Detection and Spectral Measurements of Coherent Synchrotron Radiation at FLASH

Diploma Thesis
by
Christopher Behrens

submitted to
Institut für Experimentalphysik
Universität Hamburg

prepared at
Deutsches Elektronen-Synchrotron (DESY), Hamburg

Hamburg, October 2008

Christopher Behrens
Deutsches Elektronen-Synchrotron
Notkestraße 85
22607 Hamburg, Germany
e-mail: christopher.behrens@desy.de

German title:
Nachweis und spektrale Messungen von kohärenter Synchrotronstrahlung bei FLASH

Published under DESY report numbers:
DESY-THESIS-2010-002
TESLA-FEL-2010-03

Printed by the DESY copy centre.
This document was typeset using LaTeX and KOMA-Script.

Gutachter der Diplomarbeit: Prof. Dr. J. Roßbach (Unversität Hamburg)
PD Dr. B. Schmidt (DESY Hamburg)

Abstract

The operation of high-gain free-electron laser (FEL) underlies tremendous demands on high quality electron beams with high peak currents. At the Free-Electron-Laser in Hamburg (FLASH), two magnetic bunch compressors are used to compress the electron bunches longitudinally. In the bunch compressor magnets, these short electron bunches generate coherent synchrotron radiation (CSR). This CSR contains information on the longitudinal bunch profile, which is relevant for driving an FEL.

In order to investigate coherent synchrotron radiation at the second bunch compressor BC3 at FLASH, a new setup behind the last dipole was installed. For the detection of coherent synchrotron radiation, which is emitted in the infrared regime, pyroelectric detectors were used. These pyroelectric detectors have been calibrated at the free-electron laser FELIX in the wavelength range from $5\,\mu$m to $110\,\mu$m.

For characterisation of the emitted radiation, a transverse scanning device was used to measure the transverse intensity distribution. Various transmission filters were used to obtain additional information about the spectral content.

In order to get spectral information with high resolution over a wide wavelength range, a rotating mirror spectrometer using reflective blazed gratings was installed. Using this spectrometer, the first spectral measurements of coherent synchrotron radiation at FLASH in a wavelength range from $10\,\mu$m to $160\,\mu$m were done.

Zusammenfassung

Der Betrieb von hochverstärkenden Freie-Elektronen Lasern (FEL) unterliegt hohen Anforderungen an die Qualität des Elektronenstrahls mit hohen Spitzenströmen. Am Freie-Elektronen Laser in Hamburg (FLASH) werden zwei magnetische Kompressoren verwendet, um die Elektronenpakete longitudinal zu komprimieren. In den Kompressormagneten erzeugen die kurzen Elektronenpakete kohärente Synchrotronstrahlung (CSR). Diese CSR enthält Informationen über das longitudinale Paketprofil, welche für den Betrieb eines FEL relevant sind.

Zur Untersuchung der kohärenten Synchrotronstrahlung beim zweiten Kompressor BC3 bei FLASH wurde ein neues Experiment hinter dem letzten Dipol aufgebaut. Für die Detektion der kohärenten Synchrotronstrahlung wurden pyroelektrische Detektoren verwendet. Diese pyroelektrischen Detektoren wurden beim Freie-Elektronen Laser FELIX über einen Wellenlängenbereich von 5 μm bis 110 μm kalibriert.

Für die Charakterisierung der emittierten Strahlung wurde ein transversal abtastendes Gerät verwendet, um die transversale Intensitätsverteilung zu messen. Verschiedene Transmission-Filter wurden verwendet um zusätzliche Informationen über den spektralen Inhalt zu erhalten.

Um spektrale Informationen mit hoher Auflösung über einen weiten Wellenlängenbereich zu erhalten, wurde eine Drehspiegel-Spektrometer mit "Blaze"-Reflexionsgittern aufgebaut. Mit diesem Spektrometer wurden erstmals spektrale Messungen von kohärenter Synchrotronstrahlung bei FLASH in einem Wellenlängenbereich von 10 μm bis 160 μm durchgeführt.

Contents

List of Tables

List of Figures

1 Introduction

In the last century, the development of light sources for highly intense electromagnetic radiation in all spectral ranges became more and more important. At the beginning, there was the discovery of the X-rays by Wilhelm Conrad Röntgen in 1895. He investigated many properties of this new kind of radiation. One of the most surprising properties was the capability of penetrating matter.
The new kind of radiation initiated a new era of research. In 1912 Max von Laue postulated a new method to explore the structure of crystals. This method is based on the diffraction of X-rays at the lattice points of crystals. The realisation of corresponding experiments pointed out the capability of X-ray diffraction. In addition, this was the evidence for the wavelike behaviour of the X-rays.

1.1 Accelerator based light sources

The next important step in the history of radiation sources came along with the development of particle accelerators. In 1944, Iwanenko and Pomeranchuk published an article with the title "On the Maximal Energy attainable in a Betatron", where they pointed out that electron accelerators are limited by radiation losses [1]. John Blewett suggested a search for the radiation losses at the 100-MeV General Electric Betatron, but only the indirect evidence was found by the observation of the shrinking orbit when the electrons neared 90 MeV. This effect could be explained by an alternative mechanism [2]. A direct observation was not possible due to the opaque doughnut-shaped beam tube.
In 1947, Herbert Pollock and his group completed a 70-MeV Synchrotron at the same laboratory, where a 100-MeV betatron was built. This new machine was not entirely covered by an opaque shielding, so that there was the possibility to detect the radiation directly. In the same year Pollock and his group detected the radiation visually, which was from now on called synchrotron radiation [3]. According to theory, the spectrum should extend into the visible region which can be seen in Fig. 1.1 [4].
At that time, the main purpose of the newly invented synchrotrons was to perform high energy physics experiments, and the emission of synchrotron radiation was an unwanted effect that limited the maximal attainable beam energy. It did not take a long time that scientists considered to use the synchrotron radiation parasitically to perform experiments.

These machines for high energy physics that allowed to use the synchrotron radiation from bending magnets parasitically were called "first generation" synchrotron radiation sources. Due to the the fact that these machines were built for particle physics, they were not optimised for the use of synchrotron radiation. For this reason, dedicated storage rings with special optics and small beam sizes were built. These machines are called "second generation" synchrotron radiation sources. In the bending magnets, a horizontal fan of synchrotron radiation with an vertical opening angle $\theta \approx \gamma^{-1}$ is emitted.

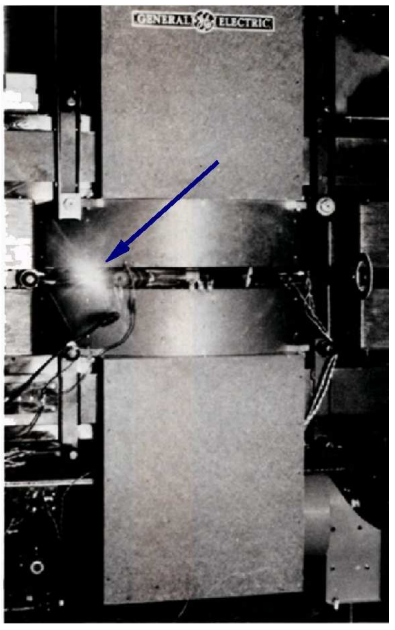

Figure 1.1: Picture of the 70-MeV synchrotron at General Electric. The blue arrow indicates one part of the bright arc of visible synchrotron radiation.

In order to produce higher intensities and a good collimation in both planes, beam insertion devices called wigglers and undulators were developed. Wigglers and undulators consist of a periodic arrangement of short dipole magnets with alternating polarity. Nowadays, modern machines contain long straight sections to accommodate the insertion devices. These machines are called "third generation" synchrotron radiation sources. The most recent development in the field of accelerator based light sources are the free-electron lasers, which produce laser-like radiation with high intensity. Free-electron lasers are tunable over a wide range and reach wavelengths down to the X-ray regime.

1.1.1 Undulator radiation

An undulator is a periodic arrangement of short dipole magnets with alternating polarity. The magnetic fields can be generated by permanent magnets or by electromagnets. The quantity that characterises the undulator is the dimensionless undulator parameter

$$\boxed{K = \frac{\lambda_u e B_0}{2\pi m_e c_0}} \tag{1.1}$$

with the undulator period length λ_u, the elementary charge e, the peak magnetic field B_0, the electron rest mass m_e, and the speed of light in vacuum c_0. The undulator parameter is in general in the order of 1. For higher K, the magnet arrangement is sometimes called a wiggler. Due to the Lorentz force, an electron moves on a sinusoidal trajectory in the undulator which can be seen in Fig. 1.2. The chosen coordinate system has its s-axis along the undulator parallel to the beam axis, the x-axis in the horizontal plane and the y-axis in the vertical plane. Using the expression for the alternating magnetic field, which can be

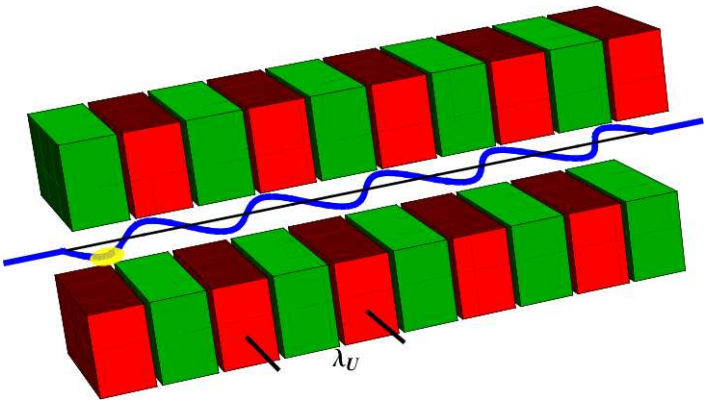

Figure 1.2: Sketch of an undulator with the sinusoidal electron beam trajectory. The magnets of alternating polarity form a periodic structure with the undulator period length λ_U. The electron bunch is represented by the yellow ellipsoid.

assumed to be sinusoidal, and the Lorentz force, the representation for the horizontal and longitudinal velocity component results in

$$\dot{x}(t) = \beta c_0 \frac{K}{\gamma} \sin(\omega_u t) + \dot{x}(t_0) \qquad \text{with} \qquad \omega_u = \frac{2\pi c_0}{\lambda_u} \tag{1.2}$$

and

$$\dot{s}(t) = \bar{\beta} c_0 + \frac{c_0 \beta^2 K^2}{4\gamma^2} \cos(2\omega_u t) \qquad \text{with} \qquad \bar{\beta} = \frac{\dot{\bar{s}}}{c} = 1 - \frac{1}{2\gamma^2}\left[1 + \frac{K^2}{2}\right]. \tag{1.3}$$

with the normalised average velocity $\bar{\beta}$ of the centre-of-gravity. Due to the sinusoidal oscillation and relativistic effects, the electron radiates synchrotron radiation with the wavelength

$$\lambda_l = \frac{\lambda_u}{2\gamma^2}\left(1 + \frac{K^2}{2} + \gamma^2 \Theta^2\right). \tag{1.4}$$

This formula is valid for the first harmonic in a planar undulator and for small angles Θ with respect to the mean momentum direction. Detailed calculations (see [5]) show that an undulator generates also higher harmonics, in the forward direction only the odd harmonics are observed. The wavelength of the mth harmonic is

$$\boxed{\lambda_m = \frac{1}{m}\frac{\lambda_u}{2\gamma^2}\left(1 + \frac{K^2}{2} + \gamma^2 \Theta^2\right) \qquad \text{with} \qquad m = 1, 2, 3, ...}. \tag{1.5}$$

The radiation output of an undulator consists of a wave-train with a finite number N_u of oscillations. N_u is the number of undulator periods. A Fourier-analysis of this finite wave-train results in the following expression for the spectral intensity distribution of the

first harmonic of an undulator

$$\boxed{I(\Delta\omega) \sim \left[\frac{\sin\left(\pi N_u \frac{\Delta\omega}{\omega_1}\right)}{\pi N_u \frac{\Delta\omega}{\omega_1}}\right]^2} \tag{1.6}$$

with $\Delta\omega$ being the frequency deviation $\omega - \omega_1$. From this equation follows that the relative bandwidth behaves like

$$\boxed{\frac{\Delta\omega}{\omega_1} \sim \frac{1}{N_u}}. \tag{1.7}$$

1.2 Free-Electron Lasers

First concrete ideas for the principle of a free-electron laser (FEL) were presented in 1971 by J.M.J Madey [6]. The first operating free-electron laser was build at Stanford University in 1977. It was lasing at a wavelength of $3.4\,\mu$m.
A free-electron laser is based on an accelerator that provides a high energy electron beam and on an undulator that enables energy transfer. The lasing process depends on the energy transfer between the light wave and the electron beam that serves as the active medium and the pump source as well. In contrast to a conventional laser, the electrons in a free-electron laser are not bound to discrete energy levels, but nevertheless a free-electron laser has all the properties of a conventional laser, like the spatial and temporal coherence or the high brightness.

1.2.1 Energy transfer in an FEL

The theory of free-electron lasers is subject of a few textbooks. Details and derivations of the following formulas can be found in the references [7, 8].
In an FEL, the electron beam and the incident light wave must propagate along the same axis to get an interaction and energy exchange. The energy transfer between an electron and a radiation field is described by

$$\boxed{\frac{dW}{dt} = -e\vec{E} \cdot \vec{v}} \tag{1.8}$$

with the electric field vector $\vec{E}$ of the radiation field and the velocity $\vec{v}$ of the electron. According to (1.8), energy transfer is only possible, if the electron beam gets a velocity component parallel to the electric field vector of the incident light wave. This horizontal velocity component will be generated by an undulator. A qualitative treatment of the energy transfer condition can be done with the help of Fig. 1.3. At point A, the transverse velocity of the electron is assumed to be parallel to the electric field, resulting in an energy transfer from the electron to the light wave. To achieve a steady energy transfer, the case

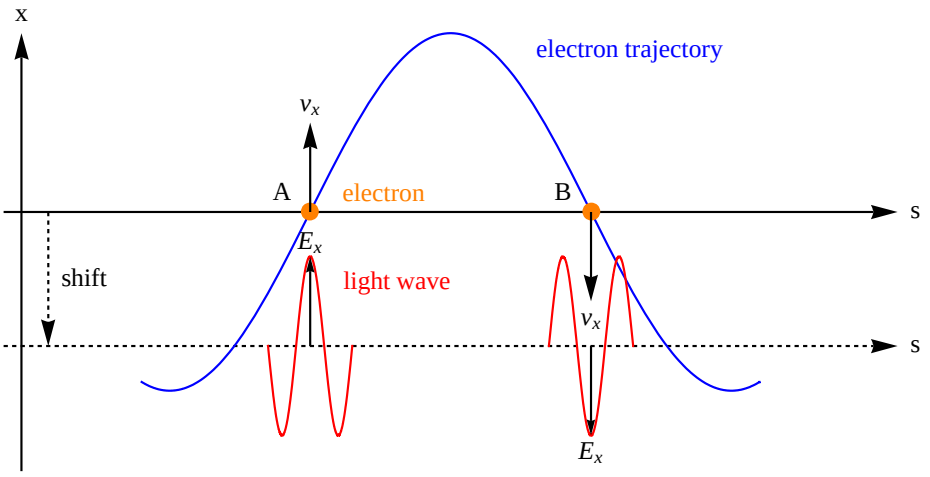

Figure 1.3: Condition to transfer energy from the light wave to the electron. The electron has to lag by a half wavelength $\lambda_l/2$ per half period of the undulator.

in point A has to hold for different times e.g. for one half period of the electron trajectory later. Due the fact that the velocity of the electron is slower than the speed of light, the electron has to slip back against the lightwave by on half period λ_l, which is the case in point B.

A more quantitative treatment can be done assuming a plane electromagnetic wave represented by

$$\vec{E}(s,t) = \vec{E}_0 \cdot \cos(k_l s - \omega_l t + \phi_0). \tag{1.9}$$

Inserting (1.9) and (1.2) in the time derivative of the expression (1.8) as well as arranging the arguments of the trigonometric functions, result in

$$\frac{dW}{dt} = -\frac{e_0 c_0 K E_0}{2\gamma}[\sin(\psi_+) - \sin(\psi_-)] \tag{1.10}$$

with

$$\psi_\pm = (k_l \pm k_u)s - \omega_l t + \phi_0. \tag{1.11}$$

Only the term ψ_+ provides continuous energy transfer, since the term ψ_- is rapidly oscillating and yields no energy exchange in average. Because of its importance, the phase ψ_+ is called ponderomotive phase. In order to sustain a steady energy transfer, the phase ψ_+ should be almost constant over the time, which means that the time derivative should vanish.

$$\frac{d\psi_+}{dt} = (k_l + k_u)\dot{s} - \omega_l = 0 \tag{1.12}$$

Due the fact that energy transfer is desired over the whole path in the undulators, the average longitudinal velocity $\dot{s}$ from (1.3) will be used in (1.12). Multiplication with $1/c_0$

and taken into account that $\omega_l = c_0 k_l$, results in

$$-\frac{k_l}{2\gamma^2}\left(1+\frac{K^2}{2}\right)+k_u-\frac{k_u}{2\gamma^2}\left(1+\frac{K^2}{2}\right)=0. \tag{1.13}$$

With the fact that $k_u << k_l$, the last expression can be neglected. That leads to

$$-\frac{k_l}{2\gamma^2}\left(1+\frac{K^2}{2}\right)+k_u \approx 0, \tag{1.14}$$

which can be easily transform to the final resonance condition for energy transfer.

$$\boxed{\lambda_l = \frac{\lambda_u}{2\gamma^2}\left(1+\frac{K^2}{2}\right)}. \tag{1.15}$$

This condition is the basic equation for all types of free-electron lasers. It should be noted that the resonance condition (1.15) is of the same form as the first harmonic of the undulator radiation in (1.4). That has impacts for the operation of an FEL, especially for providing the input radiation, because the resonance condition agrees with the first harmonic of the undulator radiation.
The main types of FEL are classified into the FEL-oscillator and the FEL-amplifier. Both types will be treated in the following sections.

1.2.2 Low-gain FEL

One way of operating an FEL is in the low-gain regime, which means that the relative energy increase of the light wave per passage of the electron in the undulator is low. To obtain a considerable output laser power, the electron has to pass the undulator many times, while the light wave is stored in an optical resonator. That is the reason why this type is called low-gain FEL. The amplification mechanism is similar to a conventional laser and is described by

$$\boxed{P = P_0(1+G)^N} \tag{1.16}$$

with the input power P_0 and the FEL gain G which is in the range of a few percent. Due to the result in (1.15), the undulator radiation can serve as the input. A quantitative treatment of the FEL dynamics (see [8]) results in the gain function for the low-gain regime that is plotted in Fig. 1.5. This plot shows the gain as a function of the energy deviation $\eta = \frac{\gamma-\gamma_r}{\gamma_r}$ with the normalised resonance energy $\gamma_r = \frac{W_r}{m_0 c_0^2}$ which is the energy to obtain the corresponding wavelength from (1.15). A positive gain is only possible if the energy of the electron beam will be tuned to off-resonance with $\eta > 0$. To store the light wave, two mirrors like in Fig. 1.4 will be used. Mirrors with a suitable reflectivity exist only for the optical and infrared wavelength range. For this reason, no low-gain FEL exists in the ultraviolet and X-ray regime. That is the regime for high-gain FELs (see next section).

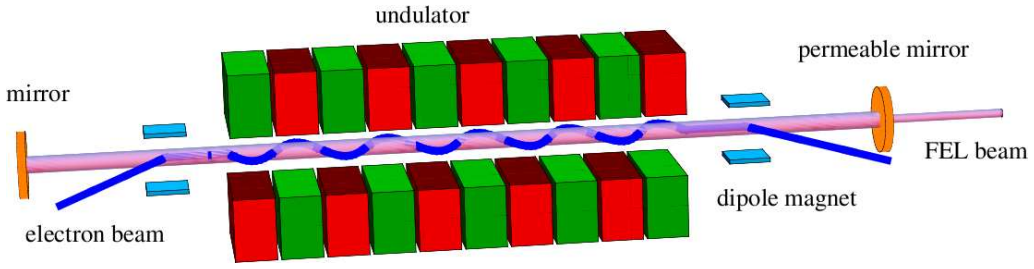

Figure 1.4: Sketch of a low-gain FEL. The main components are the undulator, the electron beam and two mirrors to establish the resonator.

The basic components of a low-gain FEL are sketched in Fig. 1.4. It mainly consist of an electron beam that can be delivered by a linac as well as by a storage ring, two mirrors to establish a resonator and a short undulator. To sustain a steady energy transfer, the energy of the electron beam is operated off-resonance with $\eta > 0$.

1.2.3 High-gain FEL

In order to obtain light amplification in the wavelength range of the ultraviolet and below, another amplification scheme is necessary due to the lack of suitable mirrors. The amplification has to take place in one pass through a very long undulator. That is the reason, why this type of FEL is called high-gain FEL.
The FEL power along the undulator is described by

$$\boxed{P \approx \frac{P_{in}}{9}\exp(z/L_g)} \tag{1.17}$$

with the gain length

$$\boxed{L_g = \frac{1}{\sqrt{3}}\left(\frac{I_A\gamma^3\sigma_r^2\lambda_u}{4\pi K^2}\frac{1}{I_p}.\right)^{1/3}}. \tag{1.18}$$

The parameter σ_r is the rms beam radius and the parameter I_p is the peak current of the electron bunch. The equation (1.17) is valid after a few gain lengths i.e. $z \geq 2L_g$. The power evolution before this region depends on the exact start-up process, which can be initiated by an external light wave (seed) or by an initial density modulation of the electron bunch. The basic layout of a high-gain FEL is based on a long undulator and a high quality electron beam. The input radiation that has to be amplified, can be provided by an external seed laser or by the electron beam itself from the spontaneous undulator radiation. The latter process is called SASE-process (Self-Amplified Spontaneous Emission) which was proposed in the early 1980s [9, 10]. The high-gain FEL has special requirements on the electron beam, and the operation is done in a different manner compared to the operation of a low-gain FEL. In order to achieve a high power amplification resp. power saturation with as small as possible an undulator length, the gain length L_g should be small. One

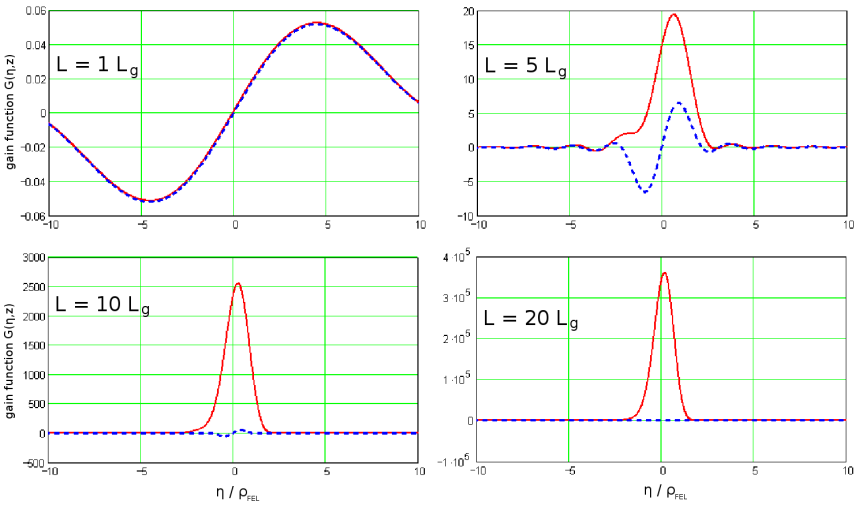

Figure 1.5: FEL-gain as a function of the normalised energy deviation for different undulator lengths. The dashed blue curve shows the gain according to the low-gain-theory, the red continuous curve is computed according to the high-gain theory (courtesy of P. Schmüser and M. Dohlus).

parameter that has a critically impact is the peak current I_p of the electron bunch that should be large. Examples of these quantities will be given in the section for FLASH.
As the name high-gain FEL implies, the gain will be much larger than in the case of low-gain FEL. The plots in Fig. 1.5 are based on semi-analytic calculation of the high-gain theory and show the gain of both FEL-types as a function of the energy deviation for different gain lengths. The energy deviation η is expressed in units of the dimensionless FEL-parameter

$$\boxed{\rho_{FEL} = \frac{1}{4\pi\sqrt{3}} \cdot \frac{\lambda_u}{L_g}}. \tag{1.19}$$

These plots indicate that the low-gain theory can be described as a "short-undulator approximation" of the more general high-gain theory.

1.3 FELIX: Free-Electron Laser for Infrared eXperiments

The Free-Electron Laser for Infrared eXperiments (FELIX) at the FOM-Institute for Plasma Physics Rijnhuizen in the Netherlands is a low-gain FEL that provides radiation in the infrared. FELIX serves as a user facility that provides continuously tunable infrared radiation in the spectral range of 4 μm to 250 μm, at peak powers ranging up to 100 MW in picosecond pulses. The layout of the facility is shown in Fig. 1.6. FELIX is a linac-driven FEL and consists of an injector and two linacs. The first linac can accelerate electrons up to 25 MeV. These electrons can either be passed through an undulator (FEL-1) for infrared radiation in the range 25 μm to 250 μm or can be accelerated in the second linac up to 45 MeV to generate FEL radiation in a second undulator (FEL-2). The second undulator can generate radiation in the range 3 μm to 40 μm.

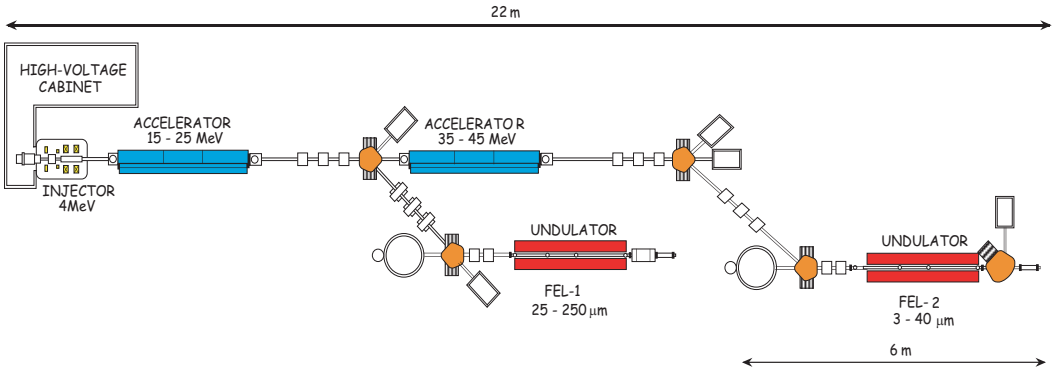

Figure 1.6: Layout of the Free-Electron Laser for Infrared eXperiments FELIX. (Courtesy of B. Redlich)

electron energy E	15 MeV - 45 MeV
FEL wavelength λ	3 μm - 250 μm
micropulse duration (nominal)	5 ps
micropulse repetition rate	25 MHz or 1 GHz
macropulse duration	$< 10\,\mu$s
macropulse repetition rate	5 (10) Hz
micropulse energy	$< 50\,\mu$J

Table 1.1: Parameters of FELIX.

The time structure of the FEL-output consists of short micropulses with durations below 5 ps. These micropulses are separated by either 1 ns or 40 ns and form a macropulse with a duration up to 15 μs. Due to the fact that FELIX is a low-gain FEL, the first few μs of the macropulse are needed to build up the saturated range of the FEL output. The FEL-radiation is coupled out of the resonator through a small on-axis hole in one the mirrors. Some parameters of FELIX are listed in table 1.1. More information can be found in [11].

1.4 FLASH: Free-Electron Laser in Hamburg

The Free-Electron Laser in Hamburg (FLASH) is a high-gain FEL (SASE-FEL) that provides radiation in the extreme-ultraviolet down to 6 nm. Details of the facility and the scientific capabilities can be found in [12].
The layout of the facility is shown in Fig. 1.7. The first part of FLASH is the laser-driven photo-injector with a normal-conducting 1.3 GHz copper cavity (RF gun) that generates electron bunches with a charge of 0.5 to 1 nC and an energy of approx. 4.5 MeV. The six superconducting accelerator modules ACC1 to ACC6 are operated with a frequency of 1.3 GHz and allow to reach a final energy of up to 1 GeV. In the first module ACC1, the beam energy is boosted to about 130 MeV, furthermore a phase off-crest operation can be used to generate an energy gradient within the bunch. This energy gradient is required for

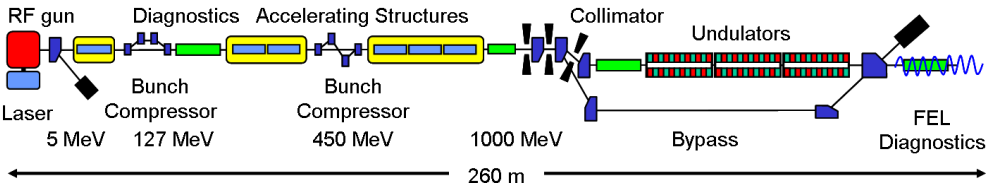

Figure 1.7: Layout of the Free-Electron-Laser in Hamburg (FLASH).

electron energy E	1 GeV
FEL wavelength λ	6.4 nm
norm. emittance ϵ_n	2 mm mrad
peak current I_p	2.5 kA
gain length L_g	1 m
saturated power P_{sat}	3 GW

Table 1.2: Design parameters of FLASH.

longitudinal bunch compression in the first magnetic bunch compressor BC2 (see subsection 1.4.1). After passing BC2, the beam is accelerated again in the modules ACC2/3 to about 450 MeV, before the electron bunches are further compressed in the second magnetic bunch compressor BC3. The modules ACC4 to ACC6 accelerate the electron beam to the final energy of up to 1 GeV. Before the electron bunches enter the undulators, they pass a collimator system to prevent radiation damages of the sensitive permanent magnets of the undulators. At the end of the linac, the electron bunches pass six 4.5 m long undulators. A dipole at the end of the undulator section separates the electron beam from the FEL-radiation, which is transported to the experimental stations for users. Some parameters of FLASH are listed in table 1.2. Further information and details are available in [13].

1.4.1 Bunch compressors

In order to drive a high-gain FEL, a high peak current is necessary. Prevention of beam blow-up resp. emittance growth by space charges forces, the high peak current cannot be produced at the source, instead the beam has to be boosted up to relativistic energies where the transverse space charge forces scale like $1/\gamma^2$. In order to generate high peak currents, the electron bunch has to be compressed, which can be accomplished, if particles in the bunch-tail catch up with the particles in the front of the bunch (bunch-head). This mechanism is called "velocity bunching" and is only possible for weakly relativistic particles. A more effective way of bunch compression makes use of an arrangement of a few dipole magnets and an energy gradient within the bunch. The arrangement is called "magnetic bunch compressor (BC)". The energy gradient within the bunches that is generated by the accelerating field of the modules is called "correlated energy spread" and depends on the phase with respect to the sinusoidal radio frequency. On-crest operation means

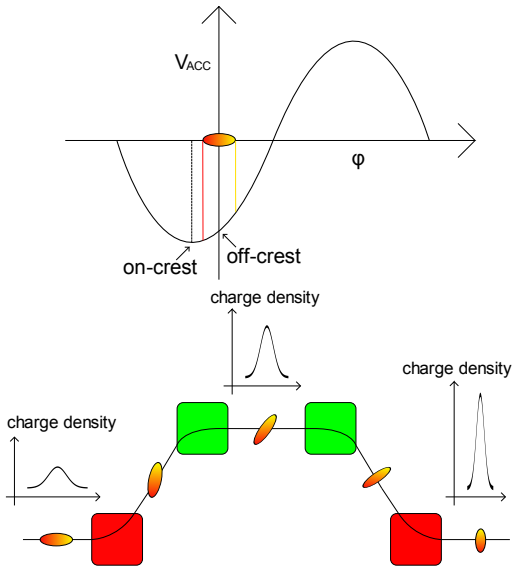

Figure 1.8: Principle of a magnetic bunch compressor: The upper figure shows the principle of off-crest operation. The lower figure sketches the mechanism of magnetic bunch compression.

maximum attainable energy transfer. In order to compress bunches longitudinally, the off-crest operation has to be done such that particles in the tail gain more energy than particles in the head. The principle is sketched in Fig. 1.8. When the electron bunches enter the dispersive sections of the bunch compressor, the particles will be deflected depending on the energy. Particles in the head take a longer path through the compressor than particles in the tail. The result is a longitudinal compression of the bunches (see Fig 1.8).
At FLASH, a two-stage compression system is used, which consist of the C-shape BC2 behind ACC1 and the S-shape BC3 in front of the modules ACC4 to ACC6. Details on the design of the bunch compressors can be found in [14].

2 Synchrotron radiation

The following sections will be about the basics of synchrotron radiation. The starting points for all expressions in the theory of synchrotron radiation are the retarded fields of a moving charge, also called Liénard-Wiechert fields. From these field equations, all relevant quantities, like the spectral energy distributions or polarisation, can be derived. The approaches and derivations in the following sections are based on the textbook by A. Hofmann [15].

With the feature of small opening angles ($\Theta \approx 1/\gamma$) (see subsection 2.3.3) some of the most important physical principles of synchrotron radiation can be illustrated. This will be done by means of the electron trajectory inside a dipole, sketched in Fig. 2.1. In the dipole magnet, the electron follows a curved trajectory with the bending radius ρ. Due to the small opening angle of the emitted radiation, the observer receives radiation only when the electron is located between the points A and B. The consequence is that the radiation within a pulse originates from a short arc of length

$$\boxed{l_r \approx \frac{2\rho}{\gamma}}. \tag{2.1}$$

The radiation pulse duration can be estimated by the difference in travel time between the electron and the emitted photons on the path from A to B. The electron follows the curved path, while the photons propagate straight-lined, resulting in

$$\Delta t = t_e - t_\gamma = \frac{2\rho}{\beta\gamma c_0} - \frac{2\rho \sin(1/\gamma)}{c_0}. \tag{2.2}$$

For high-relativistic energies, the sine function can be expanded to the second order to yield

$$\Delta t \approx \frac{2\rho}{\beta\gamma c_0}\left(1 - \beta + \frac{\beta}{6\gamma^2}\right) \approx \frac{\rho}{\gamma c_0}\left(\frac{1}{\gamma^2} + \frac{1}{3\gamma^2}\right) = \frac{4\rho}{3c_0\gamma^3}. \tag{2.3}$$

The strong energy dependence enables the generation of short radiation pulses with a corresponding spectrum containing high frequency components. A typical frequency can be given by the inverse of Δt

$$\boxed{\omega_{typ} \approx \frac{1}{\Delta t} \approx \frac{3c_0\gamma^3}{4\rho}}. \tag{2.4}$$

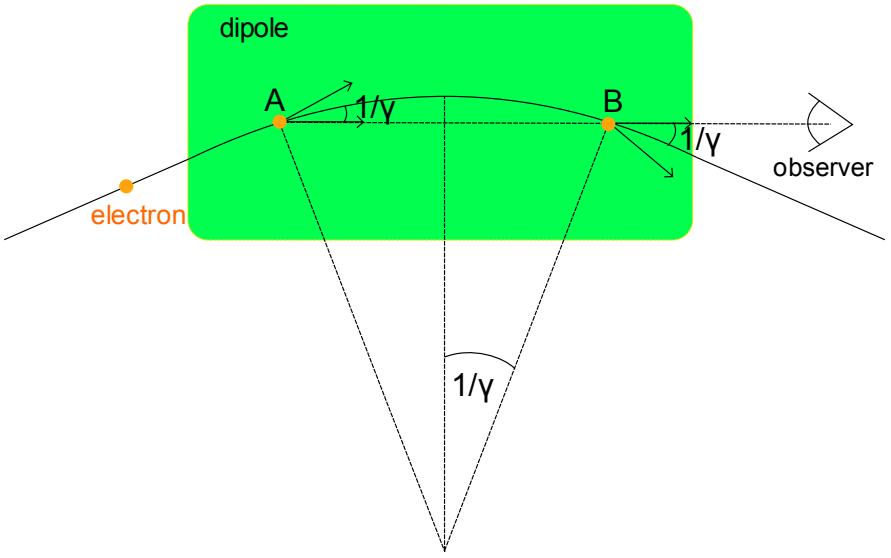

Figure 2.1: Electron trajectory inside a dipole magnet that produces a short radiation pulse.

In later sections, a modified version of the typical frequency ω_{typ} reveals some features to describe the spectrum of synchrotron radiation. The next will consider in more detail the theory of synchrotron radiation.

2.1 Liénard-Wiechert field equations

2.1.1 Retarded time

The finite propagation velocity c of electromagnetic fields results in a difference between the emission time t' of a photon and the observation time t. The emission time t' is often called retarded time and it is related to the time t by

$$\boxed{t = t' + \frac{r(t')}{c}} \tag{2.5}$$

with the distance r between the positions of emission and observation. With the help of Fig. 2.2, an important relation between the infinitesimal time scales dt and dt' can be derived. The vector

$$\vec{d} = \vec{R}(t') + \vec{r}(t') \tag{2.6}$$

is constant for all times t'. The time derivative with respect to t' yields

$$\frac{d\vec{r}(t')}{dt'} = -\frac{d\vec{R}(t')}{dt'} = -\vec{v}(t') \tag{2.7}$$

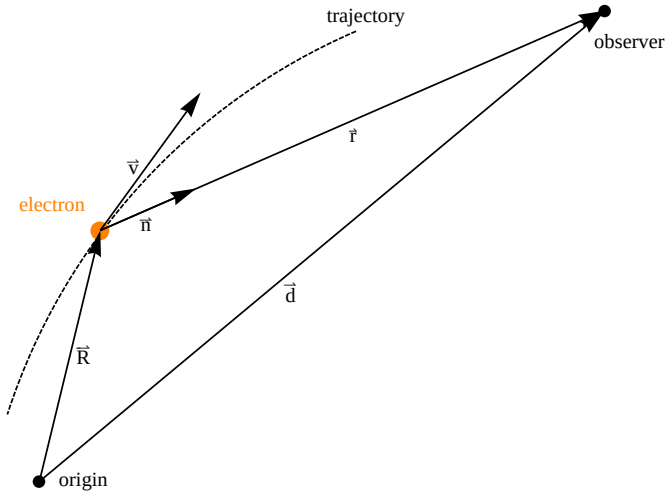

Figure 2.2: Geometry of the electron trajectory with an observer.

with the velocity vector $\vec{v}$ of the moving electron. Using the relation

$$\vec{r} \cdot \frac{d\vec{r}}{dt'} = r \cdot \frac{dr}{dt'} = -\vec{r} \cdot \vec{v} \tag{2.8}$$

without loss of generality and introducing the unit vector

$$\vec{n} = \frac{\vec{r}}{r} \tag{2.9}$$

pointing from the electron in the direction of the observer, result in

$$\frac{dr}{dt'} = -\vec{n} \cdot \vec{v}. \tag{2.10}$$

The final relation is obtained by creating the differential of (2.5) and using the previous relation (2.10):

$$\boxed{dt = \left(1 + \frac{1}{c}\frac{dr}{dt'}\right) dt' = (1 - \vec{n} \cdot \vec{\beta}) dt'}. \tag{2.11}$$

This important relation will be used in the next section to derive the frequency spectrum by means of Fourier-transformation.

2.1.2 Retarded potentials and fields

Classical electrodynamics is based on Maxwell's equation, which exist in different formulations. The differential form makes it possible to express the vector fields $\vec{E}$ and $\vec{B}$ in terms of the scalar potential Φ and the vector potential $\vec{A}$ by

$$\boxed{\vec{E} = -\nabla\Phi - \frac{\partial \vec{A}}{\partial t}} \tag{2.12}$$

and

$$\boxed{\vec{B} = \nabla \times \vec{A}}. \tag{2.13}$$

The time-dependent potentials for a single electron are given by (see [5])

$$\boxed{\Phi(t) = -\frac{e_0}{4\pi\epsilon_0}\left(\frac{1}{r(t')(1-\vec{n}(t')\cdot\vec{\beta}(t'))}\right)} \tag{2.14}$$

and

$$\boxed{\vec{A}(t) = -\frac{\mu_0 e_0}{4\pi}\left(\frac{\vec{v}(t')}{r(t')(1-\vec{n}(t')\cdot\vec{\beta}(t'))}\right)}. \tag{2.15}$$

The expressions are similar to the potentials of a static charge and a stationary current, but they explicitly contain a specific time-dependence. In order to obtain the potentials at the observation time t, the quantities $\vec{v} = c\vec{\beta}$, $\vec{n}$ and r have to be calculated at the emission time resp. retarded time t'. These potentials are called retarded potentials or Liénard-Wiechert potentials.

The electric and magnetic fields of a moving charge can be derived by solving (2.12) and (2.13) using the Liénard-Wiechert potentials. The calculations are somewhat long and contain few physical considerations. For this reason, the result will be given with reference to [15]:

$$\boxed{\vec{E}(t) = -\frac{e_0}{4\pi\epsilon_0}\left(\frac{(1-\beta^2)(\vec{n}-\vec{\beta})}{r^2(1-\vec{n}\cdot\vec{\beta})^3} + \frac{[\vec{n}\times[(\vec{n}-\vec{\beta})\times\dot{\vec{\beta}}]]}{cr(1-\vec{n}\cdot\vec{\beta})^3}\right)_{t'}} \tag{2.16}$$

and

$$\boxed{\vec{B}(t) = \frac{\vec{n}(t')\times\vec{E}(t)}{c}}. \tag{2.17}$$

The subscript t' at the bracket of the electric field indicates that the expression has to be evaluated for the retarded time t', however the electric field is a function of the observation time t. In the expression for the magnetic field, only the vector $\vec{n}$ has to be evaluated for the retarded time t'.

The electric field in (2.16) consists of two terms with different dependencies on the distance r. The first term is proportional to $1/r^2$ and also exists in the absence of any acceleration. In fact, for the static case with $\vec{\beta} = \dot{\vec{\beta}} = 0$, the expression recovers Coulomb's Law. The second term scales with $1/r$ and is only present in the case of acceleration. Due to the fact that the first term does not vanish if the acceleration is absent, it is sometimes called velocity term.

The quantity that expresses the radiated power is the Poynting vector

$$\boxed{\vec{S} = \frac{\vec{E}\times\vec{B}}{\mu_0}}. \tag{2.18}$$

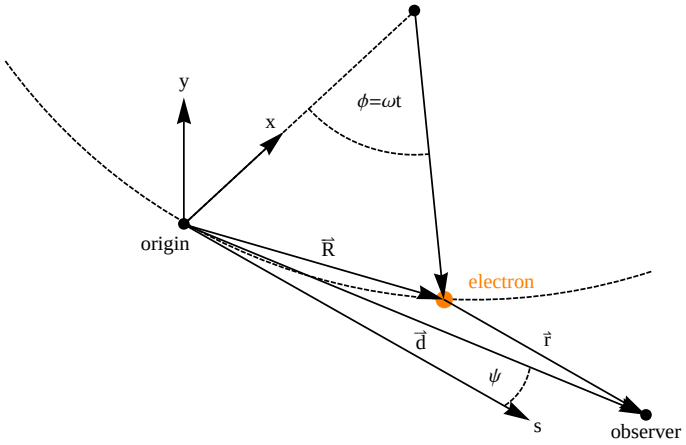

Figure 2.3: Geometry of the electron trajectory on a circular arc used for the derivation of synchrotron radiation.

Using the relation in (2.17), the Poynting vector can be given by

$$\vec{S} = \frac{1}{\mu_0 c_0}\vec{E} \times (\vec{n}_{ret} \times \vec{E}) = \frac{1}{\mu_0 c_0}(E^2 \vec{n}_{ret} - (\vec{n}_{ret} \cdot \vec{E})\vec{E}) \tag{2.19}$$

with unit vector $\vec{n}_{ret} = \vec{n}(t')$ evaluated at the retarded time. Inserting (2.16) for the electric field highlights the different contributions to the power flux. One term decreases with the distance like $1/r^4$ and is related to the near-field contribution. The second one decreases like $1/r^2$, which is called far-field contribution. In order to get the total radiated power, the Poynting vector has to be integrated over the surface of a sphere of radius r. Only the far-field contribution leads to a term that is independent of the distance r. This behaviour has an important impact on the field orientation with respect to the propagation direction. At large distances, only the second term in (2.16) exists. The numerator shows that the electric field is perpendicular to the unit vector $\vec{n}_{ret}$. Together with (2.19), $\vec{n}_{ret} \cdot \vec{E}$ vanishes and the remaining power flux is only proportional to $\vec{n}_{ret}$ with the electric field, which is perpendicular to the propagation direction.
At smaller distances, the near-field contributes to the power flux as well, and the field orientation with respect to the propagation direction is more complex.

2.2 Synchrotron radiation emitted on a circular arc

This section will cover the basics and some important properties of synchrotron radiation emitted on a circular arc, such as synchrotron radiation of a dipole magnet. The formulas will be given with reference to [15].
The starting point for the derivation will be the geometry of the electron motion shown in Fig. 2.3. The electron is moving in the (x-s)-plane on a circular arc with bending radius ρ. Its trajectory is described by the vector $\vec{R}(t')$ and the electron moves through the origin

at the time $t' = 0$. The observer is located tangentially to the circular arc at the position $\vec{d}$ at an angle ψ above the orbit plane. The electron trajectory is given by

$$\vec{R}(t') = \rho[(1 - \cos(\omega_0 t')), 0, \sin(\omega_0 t')] \tag{2.20}$$

with angular velocity $\omega_0 = \beta\, c_0/\rho$. The normalised velocity $\vec{\beta}$ and acceleration $\dot{\vec{\beta}}$ can be derived by differentiation of (2.20) with respect to t'. The distance vector $\vec{r}(t')$, pointing from the electron to the observer, is given by

$$\vec{r}(t') = \vec{d} - \vec{R}(t') \tag{2.21}$$

with the corresponding absolute value

$$r(t') = d\sqrt{1 - 2\frac{\rho}{d}\cos(\psi)\sin(\omega_0 t') + 2\left(\frac{\rho}{d}\right)^2 (1 - \cos(\omega_0 t'))}. \tag{2.22}$$

In order to yield the analytical expression for the radiated field, some approximations have to be made. The first one is the fundamental dipole approximation that expands the expression (2.21) into powers of ρ/d

$$r(t') \approx d\left(1 - \frac{\rho}{d}\cos(\psi)\sin(\omega_0 t') + \frac{1}{2}\left(\frac{\rho}{d}\right)^2 (2 - 2\cos(\omega_0 t') - \cos^2(\psi)\sin^2(\omega_0 t'))\right). \tag{2.23}$$

In this approximation, all terms higher than linear orders can be neglected if the condition $d \gg \rho$ is justified. A less strict condition can be obtained if the emphasis will be on the ultra-relativistic case, where the main part of the radiation spectrum is contained within a small cone with an opening angle of about $1/\gamma$. Using the assumptions

$$|\sin(\omega_0 t')| \lesssim \frac{1}{\gamma} \quad \text{and} \quad 1 - \cos(\omega_0 t') \lesssim \frac{1}{2\gamma^2}, \tag{2.24}$$

the final approximation in linear order

$$\boxed{r(t') \approx d\left(1 - \frac{\rho}{d}\cos(\psi)\sin(\omega_0 t')\right)} \tag{2.25}$$

can then be used demanding that

$$\boxed{\frac{\rho}{d\gamma} \ll 1} \tag{2.26}$$

is fulfilled [15]. This condition is less strict than $\frac{\rho}{d} \ll 1$, but it should be noted that this approximation is derived for the main part of the spectrum. For long wavelengths, which are also emitted with angles larger than $1/\gamma$ (see section 2.3), this approximation is not justified in general. In this case, the validity of the approximations has to be checked or compared with numerical simulations (see chapter 7).
The following derivations of the electric fields are based on the approximation in (2.25).

2.2.1 The radiation field in time-domain

In the far-field, where the condition (2.26) is satisfied, the electric field in the time-domain is given by

$$\vec{E}(t) = -\frac{e_0}{4\pi\epsilon_0}\left(\frac{[\vec{n}\times[(\vec{n}-\vec{\beta})\times\dot{\vec{\beta}}]]}{cr(1-\vec{n}\cdot\vec{\beta})^3}\right)_{t'} \tag{2.27}$$

with neglecting the velocity term, which does not contribute to the energy flux at large distances. Using the relevant motion described by (2.20) and the relation

$$t = t' + \frac{r(t') - d}{c_0} \tag{2.28}$$

between the observation time t and the retarded time t', the electric field in the time-domain is given by (see [15])

$$\boxed{\vec{E}(t) = \frac{e_0\omega_0\gamma^4}{\pi\epsilon_0 c_0 d}\frac{[-(1+\gamma^2\psi^2-(\gamma\omega_0 t')^2), -2\gamma\omega_0 t'\gamma\psi, 0]}{(1+\gamma^2\psi^2+(\gamma\omega_o t')^2)^3}}. \tag{2.29}$$

The terms including the retarded time t' can be replaced by

$$\gamma\omega_0 t' = 2\sqrt{1+\gamma^2\psi^2}\sinh\left(\frac{1}{3}\operatorname{arcsinh}\left(\frac{2\omega_c t}{(1+\gamma^2\psi^2)^{3/2}}\right)\right) \tag{2.30}$$

with the critical frequency

$$\omega_c = \frac{3c_0\gamma^3}{2\rho} \tag{2.31}$$

that is two times the typical frequency estimated in (2.4). The expression for the electric field in (2.29) shows the following symmetry properties, in which E_x represents the horizontal component (the first component in Eq. (2.29)) and E_y represents the vertical component of the electric field. The longitudinal component E_s vanishes. Inversion of the time and the vertical angle yield

$$\boxed{\begin{aligned} E_x(-t,\psi) &= E_x(t,\psi), E_y(-t,\psi) = -E_y(t,\psi) \\ E_x(t,-\psi) &= E_x(t,\psi), E_y(t,-\psi) = -E_y(t,\psi) \end{aligned}}. \tag{2.32}$$

The maximum field amplitude is given at $t = 0$ and $\psi = 0$ by

$$\boxed{E_{max} = \frac{e_0\omega_0\gamma^4}{\pi\epsilon_0 c_0 d}}. \tag{2.33}$$

In chapter 7, the analytical expression will be compared with numerical simulations to check the validity of the used approximations.

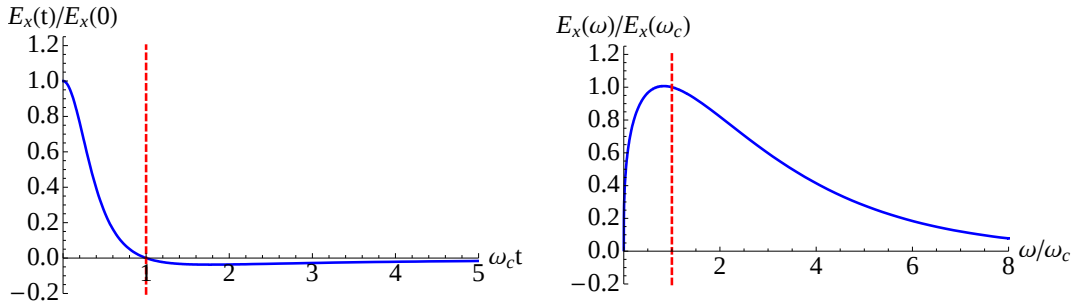

Figure 2.4: Left: Horizontal electric field component in time-domain. Right: Horizontal electric field component in frequency-domain.

2.2.2 The radiation field in the frequency-domain

The electric field in the frequency-domain can be derived by means of Fourier-transformation given by

$$\vec{\tilde{E}}(\omega) = \frac{1}{\sqrt{2\pi}} \int_{-\infty}^{\infty} \vec{E}(t) e^{-i\omega t} dt. \tag{2.34}$$

Due to the fact that the relation between the observation time t and the retarded time t' can be complicated for a general motion, the integration variable t in (2.34) can be replaced by t' with the corresponding infinitesimal time-element found in (2.11). Neglecting the *velocity* term, the general expression for the electric field in the frequency-domain is given by

$$\boxed{\vec{\tilde{E}}(\omega) = \frac{e_0}{\sqrt{2\pi} 4\pi\epsilon_0 c_0} \int_{-\infty}^{\infty} \frac{[\vec{n} \times [(\vec{n} - \vec{\beta}) \times \dot{\vec{\beta}}]]}{r(1 - \vec{n} \cdot \vec{\beta})^2} e^{-i\omega(t' + r(t')/c_0)} dt'}. \tag{2.35}$$

The magnetic field can be expressed in the same way as in the time-domain by

$$\boxed{\vec{\tilde{B}}(\omega) = \frac{\vec{n} \times \vec{\tilde{E}}(\omega)}{c_0}}. \tag{2.36}$$

Using the motion described by (2.20) and the relation in (2.28), the electric field can be given in terms of the components by

$$\boxed{\begin{aligned} \tilde{E}_x(\omega) &= \frac{-\sqrt{3} e_0 \gamma}{(2\pi)^{3/2} \epsilon_0 c_0 d} \left(\frac{|\omega|}{2\omega_c}\right) (1 + \gamma^2\psi^2) \mathrm{K}_{2/3} \left(\frac{\omega}{2\omega_c} (1 + \gamma^2\psi^2)^{3/2}\right) \\ \tilde{E}_y(\omega) &= \frac{i\sqrt{3} e_0 \gamma}{(2\pi)^{3/2} \epsilon_0 c_0 d} \left(\frac{\omega}{2\omega_c}\right) \gamma\psi \sqrt{(1 + \gamma^2\psi^2)} \mathrm{K}_{1/3} \left(\frac{\omega}{2\omega_c} (1 + \gamma^2\psi^2)^{3/2}\right) \end{aligned}}. \tag{2.37}$$

As in the case of the time-domain expression, the longitudinal component vanishes.
The electric field in the frequency-domain can also expressed by Airy functions, instead of using the modified Bessel functions K_i. The plots in Fig. 2.4 present the normalised

horizontal component of the electric field in frequency-domain as well as in time-domain for the case $\psi = 0$. The left plot shows that the electric field has a zero-crossing at the time $t = 1/\omega_c$. The right plot shows that there is no DC-component in the spectrum. This can also be seen by evaluating the time integral

$$\int_{-\infty}^{\infty} \vec{E}(t)dt = 0, \tag{2.38}$$

which is related to the Fourier-component by

$$\int_{-\infty}^{\infty} \vec{E}(t)dt = \sqrt{2\pi}\vec{\tilde{E}}(0). \tag{2.39}$$

2.3 Spectral distributions

The starting point for deriving the spectral distributions of synchrotron radiation is the Poynting vector defined in (2.18). If the near-field contribution of (2.16) is neglected, the Poynting vector can be written as

$$\vec{S} = \frac{1}{\mu_0 c_0} E^2 \vec{n}. \tag{2.40}$$

From the definition of the Poynting vector as

$$\vec{S} = \frac{d^2U}{dAdt}\vec{n} = \frac{1}{r^2}\frac{d^2U}{d\Omega dt}\vec{n}, \tag{2.41}$$

it follows that the energy radiated by an electron per unit solid angle can be expressed by

$$\boxed{\frac{dU}{d\Omega} = \frac{r^2}{\mu_0 c_0}\int_{-\infty}^{\infty} |\vec{E}(t)|^2 dt}. \tag{2.42}$$

Using Plancherel's Theorem, the formula can also be expressed by

$$\boxed{\frac{dU}{d\Omega} = \frac{r^2}{\mu_0 c_0}\int_{-\infty}^{\infty} |\vec{\tilde{E}}(\omega)|^2 d\omega} \tag{2.43}$$

which describes, together with the equations in (2.37), the spectral distributions of synchrotron radiation.

2.3.1 The angular spectral energy distribution

The starting point for the spectral properties and the angular dependence of synchrotron radiation is the expression in (2.43), which can be also written as

$$\frac{d^2U}{d\Omega d\omega} = \frac{2r^2}{\mu_0 c_0}|\vec{\tilde{E}}(\omega)|^2. \tag{2.44}$$

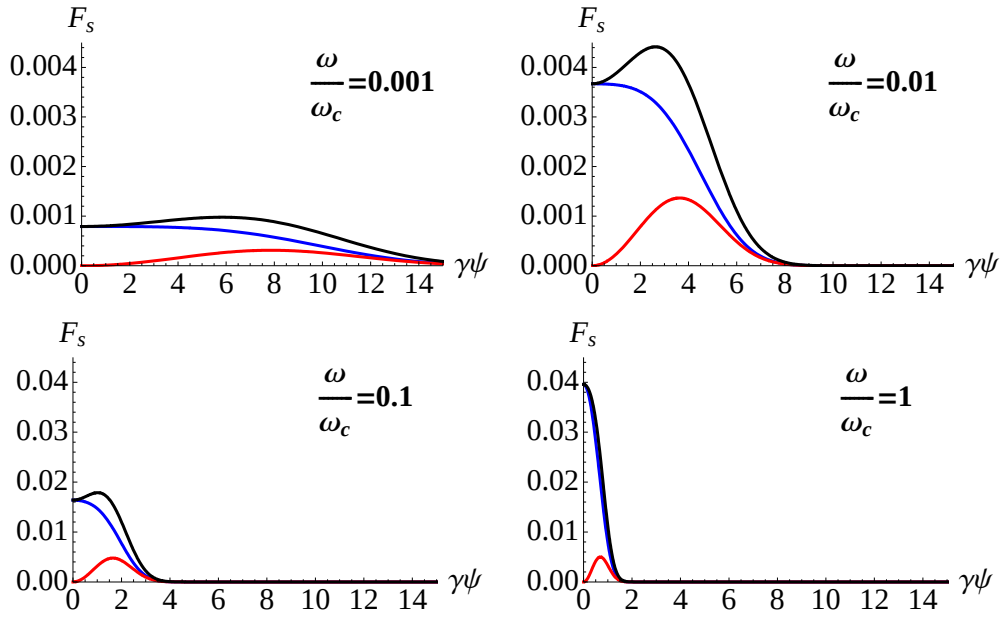

Figure 2.5: The plots show the spectral angular contributions (σ-mode (blue), π-mode (red), total (black)) as a function of the vertical opening angle $\gamma\psi$ for different frequencies ω/ω_c. The ordinates of the second row are scaled by a factor of 10 with respect to the first row.

Using the electric field terms in (2.37), the angular spectral energy distribution can be expressed by

$$\boxed{\frac{d^2U}{d\Omega d\omega} = \frac{U_0\gamma}{\omega_c}[F_{s\sigma}(\omega,\psi) + F_{s\pi}(\omega,\psi)] = \frac{U_0\gamma}{\omega_c}F_s(\omega,\psi)}, \tag{2.45}$$

taking into account both polarisation modes: the σ-mode with the electric field in the plane of the trajectory and the π-mode with the electric field perpendicular to it. The quantity U_0 describes the energy that would be radiated in one pass in a homogeneous magnet with bending radius ρ:

$$\boxed{U_0 = \frac{4\pi r_0 m_0 c_0^2 \gamma^4}{3\rho}} \tag{2.46}$$

with the classical electron radius r_0. The dimensionless function F_s is expressed by means of modified Bessel functions and fulfils the normalisation

$$\int_0^{2\pi} d\phi \int_{-\infty}^{\infty} d(\gamma\psi) \int_0^{\infty} F_s(\omega,\psi) d(\omega/\omega_c) = 1. \tag{2.47}$$

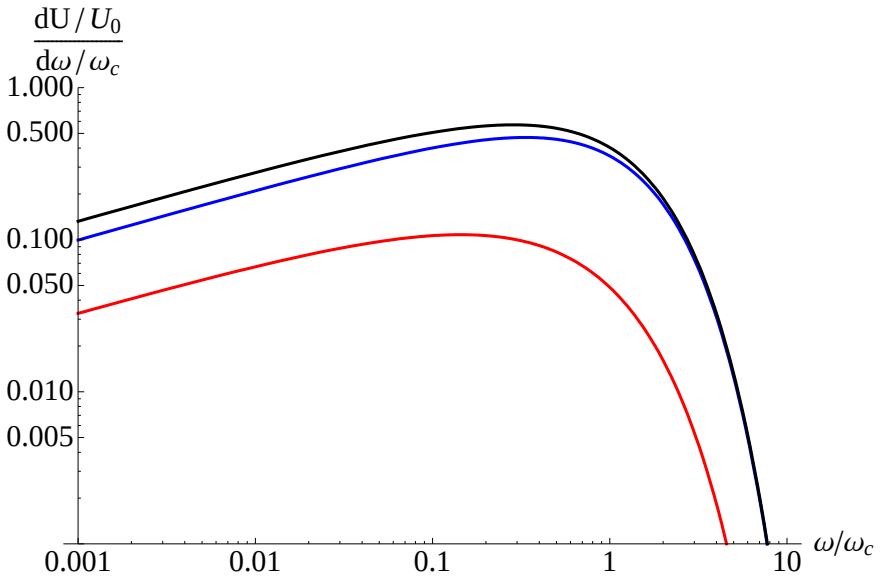

Figure 2.6: The plots show the spectral energy (σ-mode (blue), π-mode (red), total (black)) as a function of the frequencies ω/ω_c.

F_s has two components, one for each polarisation mode:

$$\boxed{\begin{aligned} F_{s\sigma}(\omega,\psi) &= \left(\frac{3}{2\pi}\right)^3 \left(\frac{\omega}{2\omega_c}\right)^2 (1+\gamma^2\psi^2)^2 \mathrm{K}^2_{2/3}\left(\frac{\omega}{2\omega_c}(1+\gamma^2\psi^2)^{3/2}\right) \\ F_{s\pi}(\omega,\psi) &= \left(\frac{3}{2\pi}\right)^3 \left(\frac{\omega}{2\omega_c}\right)^2 \gamma^2\psi^2(1+\gamma^2\psi^2) \mathrm{K}^2_{1/3}\left(\frac{\omega}{2\omega_c}(1+\gamma^2\psi^2)^{3/2}\right) \end{aligned}}. \tag{2.48}$$

The dependencies of the spectral components in (2.48) on the vertical opening angle ψ and on the frequency ω are plotted in Fig. 2.5. In the median plane ($\psi = 0$), the π-mode polarisation disappears and the total intensity is given by the σ-mode polarisation. For low frequencies ($\omega \ll \omega_c$), the intensity is distributed over angles larger than $1/\gamma$. For frequencies in the range of $\omega \approx \omega_c$, the intensity is confined to the typical opening angle of $1/\gamma$. As will be shown later in more detail, the plots in (2.5) indicate that both polarisation modes are of the same order for large opening angles.

2.3.2 The spectral energy distribution

In the case where the vertical angular distribution is not resolved or of no interest, the spectral energy distribution can be introduced:

$$\boxed{\frac{dU}{d\omega} = \int \frac{d^2U}{d\Omega d\omega} d\Omega = \frac{U_0}{\omega_c}[S_{s\sigma}(\omega) + S_{s\pi}(\omega)] = \frac{U_0}{\omega_c} S_s(\omega)} \tag{2.49}$$

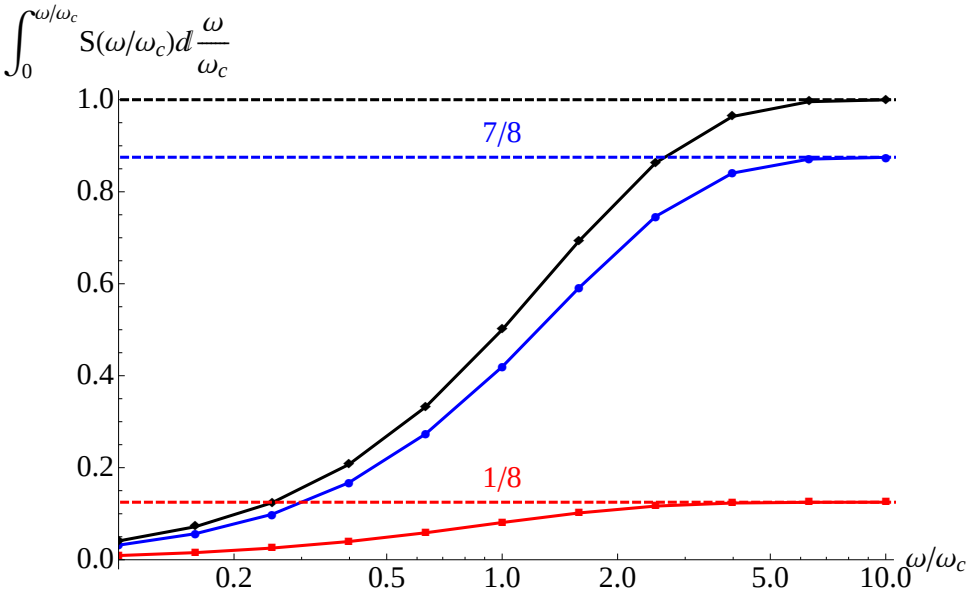

Figure 2.7: The plots show the frequency-integrated spectral energy (with running ω/ω_c) for the different polarisation modes (σ-mode (blue), π-mode (red), total (black)).

with the terms for both polarisation modes

$$\boxed{\begin{aligned} S_{s\sigma}\left(\frac{\omega}{\omega_c}\right) &= \frac{9\sqrt{3}}{16\pi}\frac{\omega}{\omega_c}\left(\int_{\omega/\omega_c}^{\infty} \mathrm{K}_{5/3}(z')dz' + \mathrm{K}_{2/3}\left(\frac{\omega}{\omega_c}\right)\right) \\ S_{s\pi}\left(\frac{\omega}{\omega_c}\right) &= \frac{9\sqrt{3}}{16\pi}\frac{\omega}{\omega_c}\left(\int_{\omega/\omega_c}^{\infty} \mathrm{K}_{5/3}(z')dz' - \mathrm{K}_{2/3}\left(\frac{\omega}{\omega_c}\right)\right) \end{aligned}}. \tag{2.50}$$

Fig. 2.6 shows the normalised energy spectrum with both polarisation modes. The spectrum covers a wide frequency range and is dominated by the σ-mode polarisation. The maximum of the plotted functions appears slightly below the critical frequency ω_c. At low frequencies ($\omega \ll \omega_c$), the spectrum scales with $S_s \sim \left(\frac{\omega}{\omega_c}\right)^{1/3}$ and is independent of the electron energy.

In order to show how the total energy spectrum is distributed over both polarisation modes, an integration of the spectral energy over the frequency can be carried out, resulting in

$$\boxed{\int_0^{\infty} \left(S_{s\sigma}(\frac{\omega}{\omega_c}) + S_{s\pi}(\frac{\omega}{\omega_c})\right) d\left(\frac{\omega}{\omega_c}\right) = \frac{7}{8} + \frac{1}{8} = 1}. \tag{2.51}$$

Integration over all frequencies shows that almost the whole intensity (87.5%) of synchrotron radiation is σ-mode polarised. If the focus is in the low-frequency range, the situation is different and the σ-mode polarisation is less dominant, as can be seen in Fig. 2.7. The integration of the energy spectrum over the frequency also reveals the fact

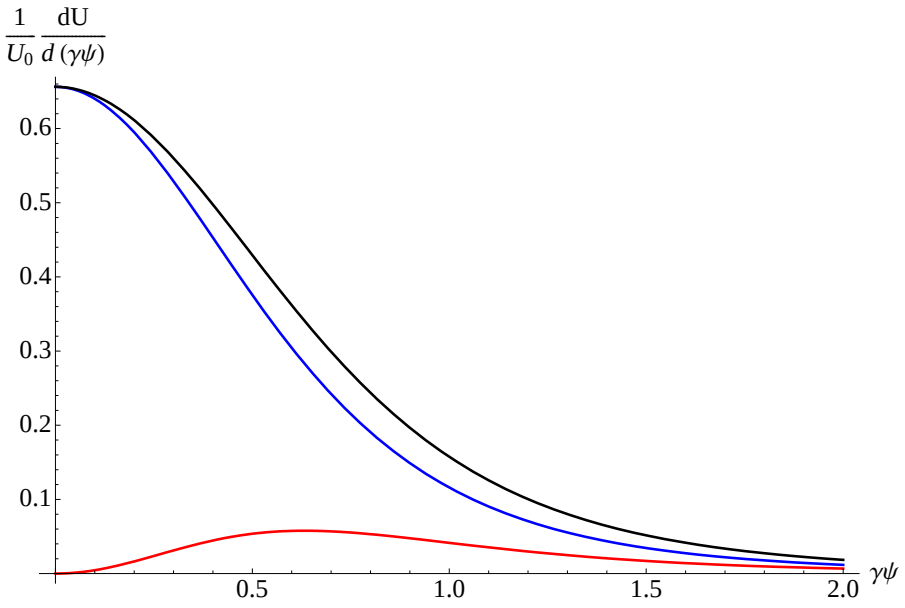

Figure 2.8: The plots show the frequency-integrated spectral energy (over all frequencies) for the different polarisation modes (σ-mode (blue), π-mode (red), total (black)) as a function of the vertical opening angle $\gamma\psi$.

that the critical frequency ω_c divides the spectrum into two equal parts

$$\boxed{\int_0^{\omega_c} \left(S_{s\sigma}(\frac{\omega}{\omega_c}) + S_{s\pi}(\frac{\omega}{\omega_c}) \right) d\left(\frac{\omega}{\omega_c}\right) = 0.5}. \tag{2.52}$$

2.3.3 The angular energy distribution

The frequency-integrated angular distribution is obtained by integration of the spectral angular distribution in Eq. (2.45) over all frequencies. With respect to the polarisation modes, it yields

$$\boxed{\frac{dU}{d\Omega} = \int_0^\infty \frac{d^2U}{d\Omega d\omega} d\omega = \frac{U_0\gamma}{\omega_c} \int_0^\infty [F_{s\sigma}(\omega,\psi) + F_{s\pi}(\omega,\psi)] d\omega = \frac{dU_\sigma}{d\Omega} + \frac{dU_\pi}{d\Omega}} \tag{2.53}$$

with the contributions

$$\boxed{\begin{aligned} \frac{dU_\sigma}{d\Omega} &= \frac{U_0\gamma}{2\pi} \frac{21}{32} \frac{1}{(1+\gamma^2\psi^2)^{5/2}} \\ \frac{dU_\pi}{d\Omega} &= \frac{U_0\gamma}{2\pi} \frac{15}{32} \frac{\gamma^2\psi^2}{(1+\gamma^2\psi^2)^{7/2}} \end{aligned}}. \tag{2.54}$$

The ϕ-integrated angular spectrum is plotted in Fig. 2.8 for both polarisations as a function of the vertical opening angle $\gamma\psi$. On-axis with $\gamma\psi = 0$, the σ-mode is maximal and the π-mode vanishes.

A fundamental feature of synchrotron radiation is the typical opening angle of $1/\gamma$. Nevertheless, quantitative treatments show that in fact the vertical opening angle is frequency-

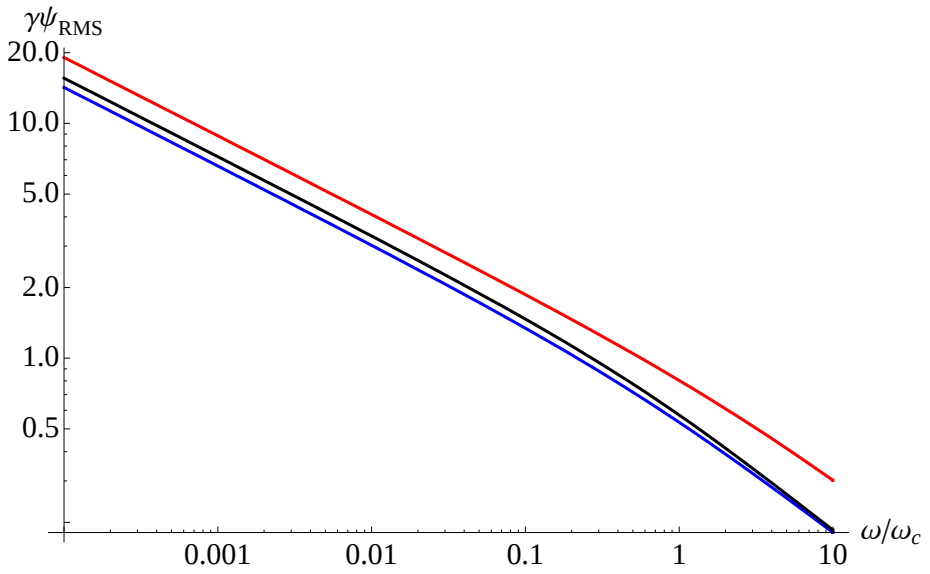

Figure 2.9: The plots show the RMS opening angle as a function of the frequency for the different polarisation modes (σ-mode (blue), π-mode (red), total (black)).

dependent. This treatment can be carried out by evaluation of the RMS opening angle $(\gamma\psi)_{\mathrm{RMS}} = \sqrt{<\gamma^2\psi^2>}$:

$$\boxed{\begin{aligned} <\gamma^2\psi^2>_\sigma &= \frac{\int \gamma^2\psi^2 \frac{d^2U_\sigma}{d\Omega d\omega} d\Omega}{\int \frac{d^2U_\sigma}{d\Omega d\omega} d\Omega} \\ <\gamma^2\psi^2>_\pi &= \frac{\int \gamma^2\psi^2 \frac{d^2U_\pi}{d\Omega d\omega} d\Omega}{\int \frac{d^2U_\pi}{d\Omega d\omega} d\Omega} \end{aligned}} \tag{2.55}$$

The total variance is given by the weighted values

$$\boxed{<\gamma^2\psi^2> = \frac{S_{s\sigma} <\gamma^2\psi^2>_\sigma + S_{s\pi} <\gamma^2\psi^2>_\pi}{S_{s\sigma} + S_{s\pi}}} \tag{2.56}$$

with the spectral functions S_i defined in (2.50).
The evaluation of these integrals is plotted in Fig. 2.9. For low frequencies, the RMS opening angle is significantly larger than the typical $1/\gamma$. Using the frequency-integrated angular distribution in (2.54), the variance of the opening angle yields

$$\boxed{\begin{aligned} <\gamma^2\psi^2>_\sigma &= \frac{1}{U_\sigma}\int_{-\infty}^{\infty} \frac{dU_\sigma}{d\psi}\gamma^2\psi^2 d(\gamma\psi) = \frac{1}{2} \\ <\gamma^2\psi^2>_\pi &= \frac{1}{U_\pi}\int_{-\infty}^{\infty} \frac{dU_\pi}{d\psi}\gamma^2\psi^2 d(\gamma\psi) = \frac{3}{2} \\ <\gamma^2\psi^2> &= \frac{1}{U_0}\int_{-\infty}^{\infty} \frac{dU}{d\psi}\gamma^2\psi^2 d(\gamma\psi) = \frac{5}{8} \end{aligned}}. \tag{2.57}$$

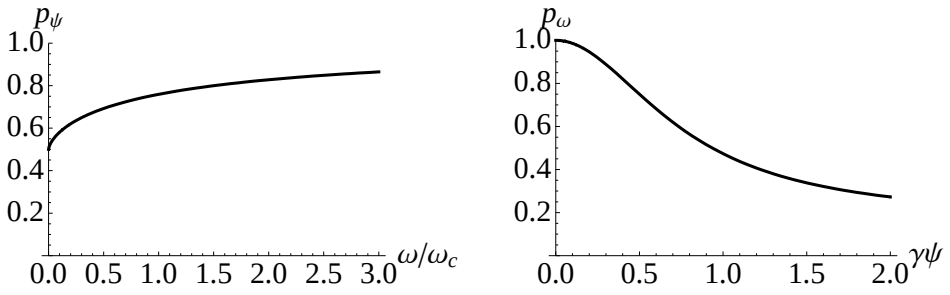

Figure 2.10: Left: Angle-integrated degree of polarisation as a function of the frequency. Right: Frequency-integrated degree of polarisation as a function of the vertical opening angle.

2.4 Degrees of polarisation

Synchrotron radiation has well defined polarisation modes, which are dependent on frequency and observation angle. The dependence on the frequency can be shown by evaluating the expression

$$\boxed{p_\psi(\omega/\omega_c) = \frac{\frac{dU_\sigma}{d\omega} - \frac{dU_\pi}{d\omega}}{\frac{dU_\sigma}{d\omega} + \frac{dU_\pi}{d\omega}} = \frac{S_{s\sigma} - S_{s\pi}}{S_{s\sigma} + S_{s\pi}}}, \tag{2.58}$$

where $\frac{dU}{d\omega}$ is the angle-integrated spectral distribution in (2.49). This expression gives the degree of horizontal resp. σ-mode polarisation. In the left plot of Fig. 2.10, the degree of polarisation as a function of the frequency is shown. For low frequencies, the degree of polarisation is less dominated by the σ-mode. In the case of the frequency-integrated angular distribution given by the ϕ-integrated version of (2.54), the degree of polarisation results in

$$\boxed{p_\omega(\gamma\psi) = \frac{\frac{dU_\sigma}{d(\gamma\psi)} - \frac{dU_\pi}{d(\gamma\psi)}}{\frac{dU_\sigma}{d(\gamma\psi)} + \frac{dU_\pi}{d(\gamma\psi)}} = \frac{1 + 2\gamma^2\psi^2/7}{1 + 12\gamma^2\psi^2/7}}. \tag{2.59}$$

In the right plot of Fig. 2.10, the degree of polarisation as a function of the vertical opening angle is shown. The degree of polarisation decreases with larger opening angles.

3 Coherent radiation effects

In modern accelerators facilities, like free-electron lasers, short bunch lengths with high peak currents are of crucial importance (see 1.2.3). If these short bunches are stimulated to produce radiation, e.g. in the presence of a magnetic dipole, coherent radiation effects are observable. These coherent radiation effects can enhance the radiated energy by several orders of magnitudes.

3.1 Coherent emission

Basically, there are two mechanisms to generate coherent emission, which is sketched in Fig. 3.1.
The first one is that charges distributions like electron bunches radiate coherently, if the observing wavelength λ is longer or comparable to the length scale of the charge distributions itself. Each electron emits an electromagnetic wave with just a small phase difference with respect to the other emitting electrons. The result is an electromagnetic wave, whose electric field is enhanced by the number of the electrons. Expressed by means of the Poynting vector, the radiation energy scales with the square of the number of electrons.

$$\boxed{S \sim E_N^2 = (NE_0)^2 \sim N^2} \tag{3.1}$$

Incoherent radiation just scales linearly with the number of electrons. A more detailed consideration will be given in the next section about the form factor.
The second mechanism is based on density modulations within a charge distribution. If the modulation has a period of l_{mod} in the direction of emitted electromagnetic radiation, the electromagnetic waves from the regions with a high density are added coherently at a wavelength $\lambda = l_{mod}$. The corresponding radiation intensity scales also quadratically with the number of the contributing electrons.

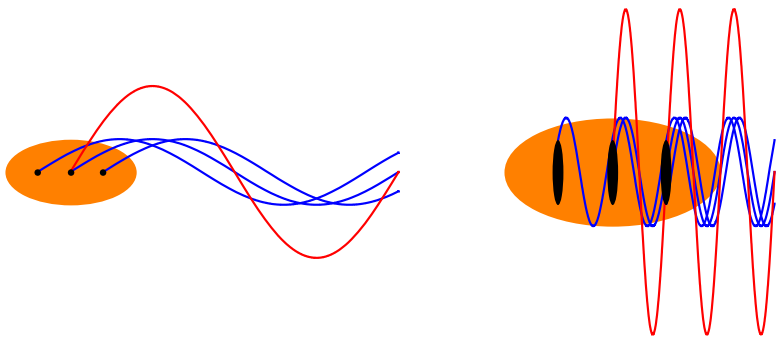

Figure 3.1: Left: A bunch, represented by three electrons, emits coherent radiation with a wavelength larger than the bunch length itself $\lambda > l_b$. Right: A bunch, which possesses a density modulation of three dense regions, emits coherent radiation with a wavelength comparable to modulation length itself $\lambda \approx l_{mod}$.

3.2 Form factor

A quantity charactersing the amount of coherent radiation is the form factor. The starting point is the superposition of the electric fields by N individual electrons of a bunch.

$$\vec{E}(t) = \sum_{i=1}^{N} \vec{E}_i(t) \tag{3.2}$$

Fourier-transformation of the electric field in the time-domain results in the corresponding expression in the frequency-domain

$$\vec{E}(\nu) = \int_{-\infty}^{\infty} \vec{E}(t) e^{-2\pi i \nu t} dt = \int_{-\infty}^{\infty} \sum_{i=1}^{N} \vec{E}_i(t) e^{-2\pi i \nu t} dt. \tag{3.3}$$

The only assumption made for the derivation is that the time dependencies of the electric fields by the individual electrons are identical, except for a time-shift due to the spatial distances. Using the assumptions of uncorrelated electrons and introducing a reference electron $\vec{E}_{ref}(t)$, the fields of all other electrons can be expressed by $\vec{E}_i(t) = \vec{E}_{ref}(t + \Delta t_i)$. The resulting electric field in the frequency-domain is given by

$$\vec{E}(\nu) = \int_{-\infty}^{\infty} \sum_{i=1}^{N} \vec{E}_{ref}(t + \Delta t_i) e^{-2\pi i \nu t} dt = \int_{-\infty}^{\infty} \sum_{i=1}^{N} \vec{E}_{ref}(\tilde{t}) e^{-2\pi i \nu (\tilde{t} - \Delta t_i)} dt. \tag{3.4}$$

Fourier-transformation of the reference field $\vec{E}_{ref}(\tilde{t})$ results in

$$\vec{E}(\nu) = \sum_{i=1}^{N} e^{2\pi i \nu \Delta t_i} \int_{-\infty}^{\infty} \vec{E}_{ref}(\tilde{t}) e^{-2\pi i \nu \tilde{t}} dt = \vec{E}_{ref}(\nu) \sum_{i=1}^{N} e^{2\pi i \nu \Delta t_i}. \tag{3.5}$$

Independent of the kind of electromagnetic radiation, the power is proportional to the square of the electric field. In order to see the effect of the form factor, the ratio of the radiated energy of the total bunch with N electrons versus the radiated energy of a single electron is introduced by the scaling parameter

$$C(\nu) = \left| \sum_{i=1}^{N} e^{2\pi i \nu \Delta t_i} \right|^2 . \tag{3.6}$$

Following the treatments in [16], the scaling parameter can be expressed by

$$\boxed{C(\vec{k}) = N + N(N-1) \cdot |F(\vec{k})|^2} \tag{3.7}$$

with the three-dimensional form factor

$$\boxed{F(\vec{k}) = \int \rho_n(\vec{r}) e^{-i\vec{k}\cdot\vec{r}} d\vec{r}}. \tag{3.8}$$

The quantity ρ_n is the charge distribution normalised to the total bunch charge. The form factor becomes 0 for incoherent radiation with a scaling parameter of $C = N$ and 1 for coherent radiation with a scaling parameter of $C = N^2$. In the cases, where the transverse bunch dimensions do not have a great impact e.g. in the case of small observation angles or well focused long bunches, the three-dimensional form factor can be projected to the longitudinal axis s with

$$\boxed{F(k) = \int_{-\infty}^{\infty} \rho_n(s) e^{-iks} ds}. \tag{3.9}$$

Using $k = \omega/c_0$ and $s = c_0 t$ one can rewrite the longitudinal form factor as follows

$$\boxed{F(\omega) = \int_{-\infty}^{\infty} \rho_n(t) e^{-i\omega t} dt} \tag{3.10}$$

where $\rho_n(t)$ is the temporal profile of the bunch.
Considerations and investigations on the influence of transverse size effects can be found in [17].

3.3 Coherent radiation diagnostics

As already mentioned in subsection 1.2.3, it is necessary to have a high peak current I_0 and a small transverse beam size σ_r to achieve a small gain length L_0. These quantities are connected to the shape of the electron bunches and it is therefore mandatory to get as much information as possible about this. In particular, the current I is associated with the longitudinal bunch profile, which can be expressed by the normalised longitudinal charge

distribution $\rho_n(s)$ via

$$I(s) = v\rho(s) \approx c_0 Q_b \rho_n(s) \tag{3.11}$$

with the bunch charge Q_b. In the case of coherent radiation diagnostics (CRD), the goal is to determine the longitudinal bunch profile through frequency-domain measurements. The starting point of CRD is the scaling parameter in (3.7), including the longitudinal form factor in (3.9). From the measurement of the energy spectrum of a bunch of electrons follows

$$\boxed{\frac{dU}{d\omega} = C(\omega)\left(\frac{dU}{d\omega}\right)_{single} = (N + N(N-1)\cdot|F(\omega)|^2)\cdot\left(\frac{dU}{d\omega}\right)_{single}}. \tag{3.12}$$

With the number of electrons given by the bunch charge, and with a good understanding of the energy spectrum of a single electron, the absolute square of the longitudinal form factor can be determined. In principle, the longitudinal bunch profile could be retrieved by Fourier back-transformation, but this is problematic in practice due to the unknown phase of the form factor. Only the magnitude of the longitudinal form factor can be measured. There is a possibility to determine some phase informations with the Kramers-Kronig relation [16], but this works just in certain limitations. Indeed, theres is no possibility to get the precise longitudinal bunch profile with the exclusive measurement of the magnitude of the longitudinal form factor. In spite of these ambiguities, the coherent radiation spectroscopy provides a powerful method to reveal structures in the bunch with a resolution that is far better than that of any time-domain measurement (see [18]). Moreover, coherent radiation can be utilised for a bunch compression monitor [19].

3.3.1 Coherent synchrotron radiation

In modern accelerator facilities, especially at Free-Electron Lasers where short bunches are necessary, the main coherent radiation sources are coherent diffraction radiation (CDR), coherent transition radiation (CTR), and coherent synchrotron radiation (CSR). A theoretical treatment of CDR and CTR, and as well consideration for applications in beam diagnostics can be found in [20]. The diagnostics with CTR is destructive because the bunch to be analysed has to pass through a radiation screen, but it allows measurements down to short wavelengths in the optical range. In contrast to this, diagnostics with CDR is a non-destructive method that implies a suppression a short wavelengths components. CSR, finally, has the big advantage that it permits destruction-free diagnostics in the entire wavelength range. Coherent synchrotron radiation shows no suppression of short wavelengths. The plot in Fig. 3.2 shows energy spectra of synchrotron radiation according to (2.49) with

$$\frac{dU}{d\lambda} = \frac{dU}{d\omega}\cdot\left|\frac{d\omega}{d\lambda}\right| = \frac{2\pi c_0}{\lambda^2}\cdot\frac{dU}{d\omega} \tag{3.13}$$

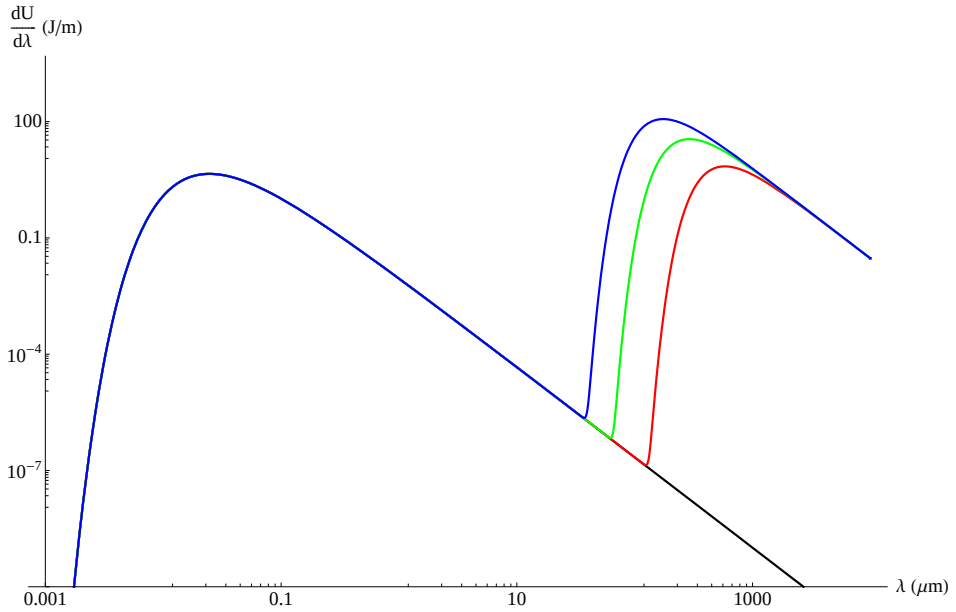

Figure 3.2: Spectral energy distributions of synchrotron radiation for a bunch charge of 1 nC, a beam energy of 400 MeV and a magnetic dipole field of 0.2 T. The plot shows the incoherent part (black) and three distributions including coherent parts of Gaussian charge distributions. The standard deviations are 30 μm (blue), 50 μm (green) and 100 μm (red).

for the incoherent case ($C = N$) and for three different Gaussian charge distributions ($\sigma = 30\,\mu$m, $50\,\mu$m and $100\,\mu$m). The plot was generated using an electron beam energy of 400 MeV, a bunch charge of 1 nC and a magnetic dipole field of 0.2 T. It can be seen that spectrum is enhanced by several orders of magnitudes, if the radiated wavelength is comparable to the bunch length or longer.

4 Pyroelectricity

Coherent radiation from short electron bunches appears mainly in the infrared wavelength region. In the near infrared (NIR), the detection can be achieved by means of semiconductor detectors like indium gallium arsenide (InGaAs). For longer wavelengths i.e. the mid and far infrared (MIR and FIR), thermal detectors like bolometers or pyroelectric detectors have to be used. For fast applications, pyroelectric detectors turned out to be useful. These can also be mounted in vacuum.

4.1 Pyroelectric effect

Pyroelectricity or the pyroelectric effect is the phenomenon of generation of surface charges when pyroelectric crystals experience temperature changes. The unit cell of a pyroelectric crystal is non-centrosymmetric and the crystal possesses a spontaneous polarisation. These types of crystals are denoted to be polar. Typical materials are $LiTaO_3$ (lithium tantalate) or DTGS (deuterated triglycine sulfate). Additionally, there exist a lot of different ceramics revealing pyroelectricity.
The main property of pyroelectricity is the change of polarisation due to a change of the temperature. This can be described by the pyroelectric coefficient α with

$$\boxed{P(t) = \alpha T(t)}. \tag{4.1}$$

The polarisation change can be divided in two contributions. The first one is the real pyroelectric effect, where the polarisation changes due to the displacement of the crystal lattice points in a way that the existing spontaneous polarisation increases. The second one originates from the piezoelectric effect, where the volume expansion due to temperature differences results in an additional polarisation. These effects offer proper methods for the detection of electromagnetic radiation in the infrared wavelength range [21].

4.2 Pyroelectric detectors

In the detection of radiation with the help of pyroelectric crystals, four distinctive processes have to be taken into account.

- 1. the absorption of a time-dependent radiation intensity

- 2. conversion into a time-dependent temperature variation
- 3. generation of a time-dependent surface charge
- 4. signal processing with suitable amplifiers

The first process includes the optical effect like reflections at the surfaces and interferences due to internal reflections. The absorption process will be treated in a more detail in the next section. The second process deals with the temperature response of the material due to the absorption of a time-dependent radiation flux. The behaviour of this process is determined by the thermal resistance, the thermal capacitance and the time-dependent input radiation. The third process is about the charge generation at the crystal surfaces. The pyroelectric crystal represents a capacitance, and therefore, the corresponding polarisation due to the pyroelectric effect results in a surface charge density. This surface charges can be measured and processed with suitable amplifiers (process four). Further information about the signal generation and processing can be found in [22, 23, 24].

4.3 Absorption effects

The capability of the detection of radiation by pyroelectric crystals depends on the effectiveness to absorb the radiation.
The total absorption process of a material with different layers is wavelength dependent. This dependence is expressed by two effects. The first effect is due to the behaviour of the incoming electromagnetic radiation at the media boundaries. The electromagnetic wave can be transmitted or reflected. The transmission and the reflection are correlated and they depend on the refractive indices of the media at the boundaries. They are described by the Fresnel equations. The second effect is the absorption in the media itself, which normally is also wavelength dependent. The attenuated intensity is given by

$$\boxed{f_a = \frac{I(d)}{I_0} = e^{-\frac{4\pi d\kappa}{\lambda}}} \tag{4.2}$$

with the intensity I_0 at the beginning of the medium, the intensity $I(d)$ after passing the distance d in the medium and the extinction coefficient κ. The extinction coefficient and the refractive index can be combined to the more general complex refractive index

$$\boxed{\tilde{n} = n + i\kappa}. \tag{4.3}$$

Combining both processes, the behaviour at the boundaries and the absorption within the media, the total absorption and as well the total transmission and reflection can be calculated. For this purpose, a set of equations for each boundary has to be solved. This set results from the fact that the tangential component of the electric field $\vec{E}$ and the tangential

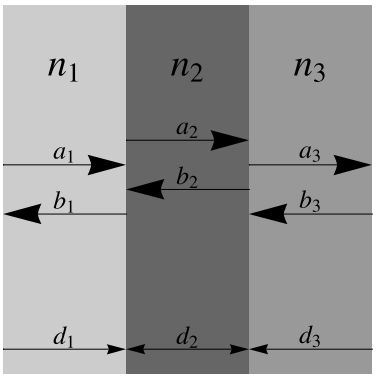

Figure 4.1: Model of a material with three different layers. The different directions of the electromagnetic waves as well the different refractive indices are indicated.

component of the magnetic field $\vec{H}$ have to be continuous at the boundaries. A model of three different layers is sketched in Fig. 4.1. Omitting the common time dependent term of electromagnetic waves, the electric field within the medium m can be expressed by

$$\boxed{E_m(s) = a_m e^{\tilde{n}_m k s} + b_m e^{-\tilde{n}_m k s}.} \tag{4.4}$$

The parameter a describes the amplitude of the electromagnetic wave propagating in the positive s-direction, and the parameter b corresponds with the same for the opposite direction. The same applies for the magnetic field with

$$\boxed{H_m(s) = \frac{\tilde{n}_m}{\mu_0 c_0} a_m e^{\tilde{n}_m k s} + \frac{\tilde{n}_m}{\mu_0 c_0} b_m e^{-\tilde{n}_m k s}}. \tag{4.5}$$

Using these equations and the restriction to non-magnetic materials with $\mu = 1$ and assuming normal incidence of the electromagnetic waves, the set of equations for each boundary result in

$$\boxed{\begin{aligned} a_m e^{\tilde{n}_m k s_b} + b_m e^{-\tilde{n}_m k s_b} &= a_{m+1} e^{\tilde{n}_{m+1} k s_b} + b_{m+1} e^{-\tilde{n}_{m+1} k s_b} \\ \tilde{n}_m a_m e^{\tilde{n}_m k s_b} + \tilde{n}_m b_m e^{-\tilde{n}_m k s_b} &= \tilde{n}_{m+1} a_{m+1} e^{\tilde{n}_{m+1} k s_b} + \tilde{n}_{m+1} b_{m+1} e^{-\tilde{n}_{m+1} k s_b} \end{aligned}}. \tag{4.6}$$

The expressions have to be evaluated at the position s_b of the boundary. Using the equations above and the expression in (4.2), the calculation of the absorption process in multiple layers of material can be computed numerically.

The following treatment will cover the absorption process in the case of $LiTaO_3$. Lithium tantalate is a uniaxial birefringent crystal with two different refractive indices. Only the component perpendicular to the optical axis which is also the pyroelectric axis, is of importance. The following refractive indices refer to the perpendicular component. In Fig. 4.2, both the real and the imaginary part of $\tilde{n}$ for $LiTaO_3$ as a function of the wavelength are shown. Using the expression in (4.2), the absorption after passing a 25 μm layer of $LiTaO_3$

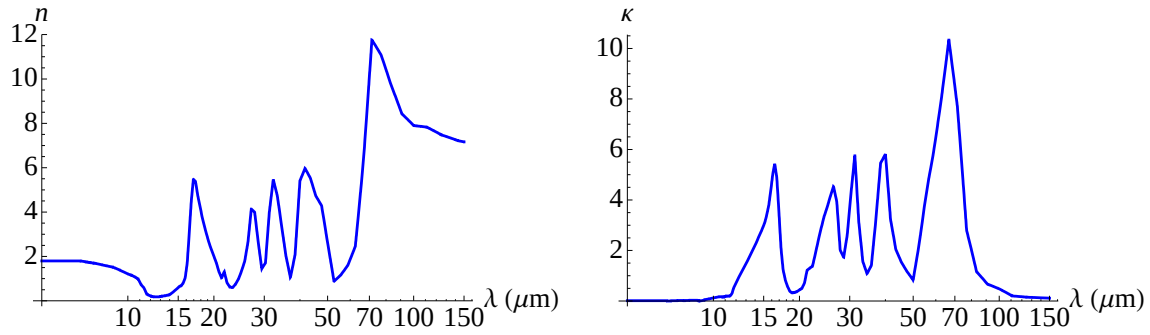

Figure 4.2: Left: Refractive index n for $LiTaO_3$. Right: Extinction coefficient κ for $LiTaO_3$.

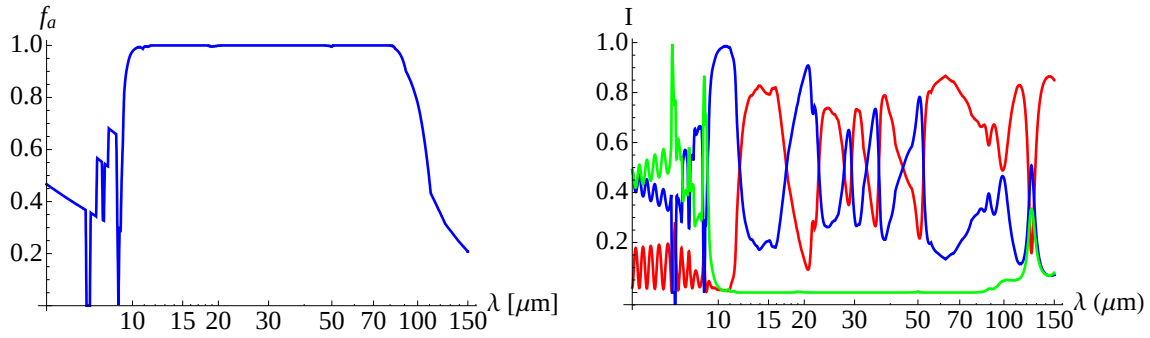

Figure 4.3: Left: Normalised absorption in 25 μm $LiTaO_3$. Right: Different components (absorption A (blue), reflection R (red), and transmission $T = 1 - A - R$ (Green)) for a single layer $LiTaO_3$ of 25 μm thickness surrounded by vacuum.

is shown in the left plot of Fig. 4.3 as function of the wavelength.

In order to include all absorption effects, concerning a real pyroelectric detector, a Mathematica-code (courtesy of B. Schmidt) was used, to perform the evaluation of the set of equations defined in (4.6).

The first step contains all effects appearing in a configuration of a single layer of $LiTaO_3$ surrounded by vacuum. The computation of 25 μm thick layer of $LiTaO_3$ is shown in the right plot of Fig. 4.3. In the wavelength range between 10 μm and 100 μm, the absorption is high in general (see the left plot of Fig. 4.3), but due to the reflection at the boundary vacuum-$LiTaO_3$, the absorption is strongly wavelength-dependent. For wavelengths longer than approx. 100 μm, the absorption is dominated by multiple internal reflections. This effect depends on the thickness of the crystal and can be modified by the choice of additional layers of a different medium. At wavelength shorter than 10 μm, $LiTaO_3$ becomes again transparent.

The second step contains additionally front -and backside coatings with Cr (chromium). A simple approximation concerning the optical constants of the chromium was made according to [25]. The extinction coefficient can be approximated by $\kappa \approx \sqrt{\sigma\lambda/c_0}$ with the

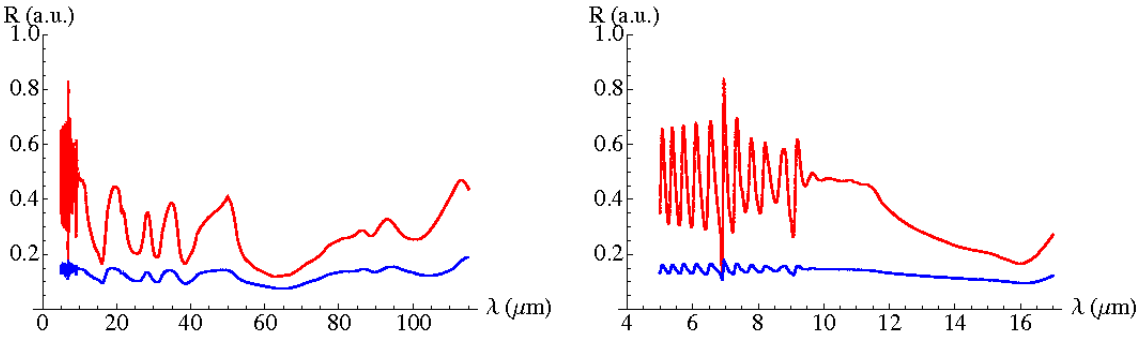

Figure 4.4: Response for two different configuration of coated $LiTaO_3$ for different wavelength ranges. (frontside 5 nm Cr and backside 20 nm Cr: red, frontside 20 nm Cr and backside 5 nm Cr: blue)

conductivity σ. A similar approximation is used for the refractive index n. This new configuration consists of three different layers surrounded by vacuum. The plots in Fig. 4.4 show the absorption of the three-layer configuration with two different front- and backside Cr coatings. The frontside coating strongly decreases the resonances in the wavelength range below 100 μm. This result from the fact that the reflectivity at the first boundary is affected by the Cr instead of the $LiTaO_3$. The same is true for longer wavelengths which are of no relevance here but might become relevant in the future. The total absorption is also decreased by the additional coating.

More investigations on the influence of different parameters, like various coating- and $LiTaO_3$-thicknesses, on the absorption behaviour can be found in [26]. The general treatment of the behaviour of electromagnetic radiation at media boundaries, also for non-normal incidence, can be found in [25].

5 Experimental setup

This chapter deals with the different experimental methods to characterise the coherent synchrotron radiation that is emitted in the last dipoles of the second bunch compressor BC3 at FLASH. The emphasis will be in the transverse distribution of the detected CSR as well as in the spectral content. The quoted absolute pulse energies are obtained by means of a calibration measurement of the pyroelectric detectors used at FELIX.

5.1 Pyro detector calibration

If absolute values of the detected radiation pulse energies are desired, calibrated detectors have to be used. Especially in the case of the spectroscopy of coherent radiation emitted by electron bunches, where the precise information of the spectral content enables to make predictions about the bunch shape, this calibration has to be known as precisely as possible. The relative sensitivity as a function of the wavelengths is of special importance for an accurate measurement of the radiation spectral composition.
For calibrations, a well known source and as well a measurement standard are necessary. The calibration measurements presented in section 6.1 were done at FELIX, a source for intense infrared radiation in the wavelength range from 110 μm down to 5 μm. Two power meters of different functional principles are used as the measurement standard.

5.1.1 Setup at FELIX

In Fig. 5.1, the schematic layout and a picture of the experimental setup are presented. The components of the experiment are mounted in a vacuum-tight box of the dimensions $60 \times 70 \times 34\,\mathrm{cm}^3$. In order to prevent water vapour absorption, the box is evacuated with a pressure in the order of 10^{-3} mbar. In the box, the incoming radiation pulses are guided through different optics, depending on the specific measurement. The first mirror, which is a movable plane mirror, directs the radiation pulses either to the pyroelectric detectors or to the power meters. There are three motor positions with the corresponding optical paths:

- The radiation pulses are guided through an attenuator and are then focused to a detector array by means of a parabolic mirror.
- The radiation pulses are directed to a pyroelectric power meter without any focusing optics.

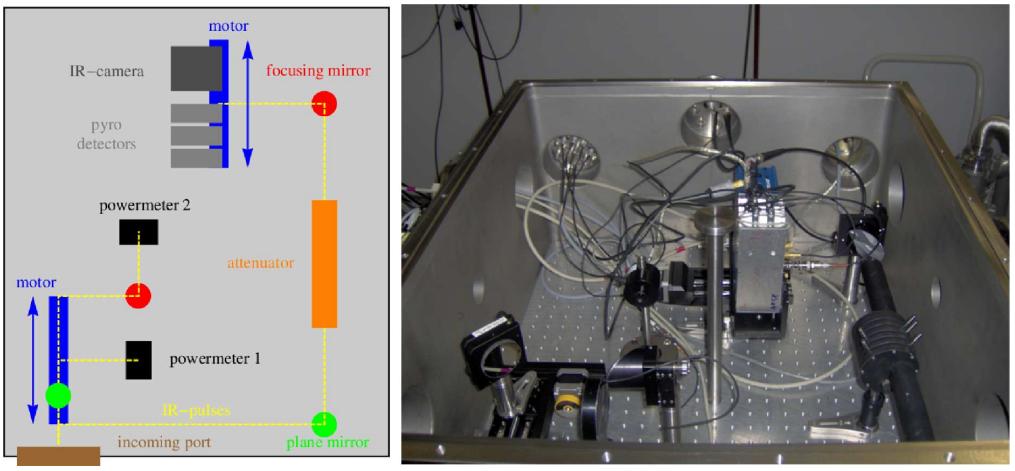

Figure 5.1: Left: Layout of the experimental setup at FELIX. The different optical paths and components are indicated. Right: Picture of the experimental setup at FELIX.

- The radiation pulses are focused on a thermo-pile power meter by means of a parabolic mirror.

The detector array is movable and consists of three different pyroelectric detectors and a camera for the detection of infrared radiation. The camera was used to align the incoming infrared pulses. Each detector is assigned to a corresponding motor position. In order to prevent damage of the pyroelectric detectors, two attenuator modules are used.

5.1.2 Power meters

For the measurements of the radiation power, two power meters of different functional principle are used. There is the pyroelectric power meter J50LP from Molectron and the thermo-pile power meter 13 PEM 001/J from Melles-Griot. In the case of the pyroelectric power meter, the working principle is the same as explained in chapter 4. Both power meters transform the temperature changes into measurable voltage signals. Additionally, the power of the infrared pulse was also measured in the transfer beamline to the experimental box. Due to transport losses, the power inside the experimental box should be smaller than in the transfer beamline outside the box. In the left plot of Fig. 5.2, the pulse energies measured with the three power meters are shown. The energies are calculated taking into account the repetition rate of the macropulses of 5 Hz. The pyroelectric power meter shows suspicious dependencies on the wavelengths compared with the other power meters. In the wavelength range from 5 μm to 17 μm, it yields values larger than those in the beamline. In the range from 15 μm to 40 μm, the values are slightly smaller than in the transfer beamline. The surface of the pyroelectric power meter appeared to be strongly damaged. For these reasons, the further data analysis was performed using the thermo-pile power meter. In the right plot of Fig. 5.2, the power of the different wavelength ranges provided by FELIX are shown. The horizontal black dashed line indicates the minimum

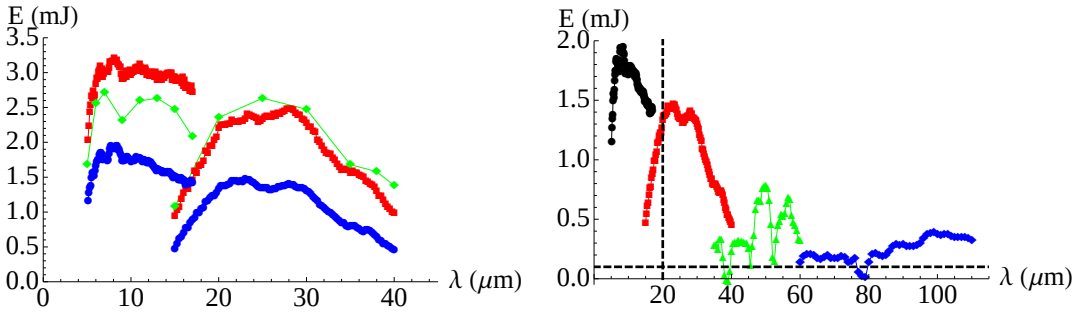

Figure 5.2: Left: Measured pulse energies with three power meters. (green: in the transfer beamline, red: pyroelectric power meter, blue: thermo-pile power meter). Right: Energy output of FELIX, measured with the thermo-pile power meter.

layer	X003	X004	X009
frontside coating	black polymer	none	black polymer
front	5 nm NiCr	5 nm NiCr	20 nm NiCr
middle	25 μm $LiTaO_3$	25 μm $LiTaO_3$	25 μm $LiTaO_3$
back	20 nm NiCr	20 nm NiCr	5 nm NiCr
backside coating	40 nm Au	40 nm Au	none

Table 5.1: Pyroelectric detector assembly of the three different types X003, X004 and X009. The radiation enters the detector at the frontside.

level used for the analysis. At wavelengths smaller than indicated by the vertical black dashed line, according to the data sheet the power meter should have a flat response. No data for this nor other available detector beyond 20 μm were available. Due to the working principle of the thermo-pile detector and due to its thickness, it is fair to assume that its responsivity for longer wavelengths stays reasonably flat.

5.1.3 Pyroelectric detectors

The experimental setup at FELIX was used to calibrate three different types of pyroelectric detectors. The three types are single type pyroelectric detectors from Infratec and are labelled with X003, X004 and X009. The detector parameters are listed in table 5.1. The purpose of the black polymer coating is to enhance the absorption of the radiation. A side effect of this coating is a change of the time response of the detector. The heat transfer from the coating to the pyroelectric crystal needs some time, resulting in two different time constants in the detector signal. The first one is the instantaneous heating from the radiation reaching the pyroelectric crystal. The second one originates from the heat deposited in the coating that reaches the inner crystal with some time delay. In order to get a more realistic model of the pyroelectric detector, the absorption process described in section 4.3 had to be extended by the black polymer coating. Due to the lack of information about the black polymer coating, this is not possible. The only way to take the coating into account

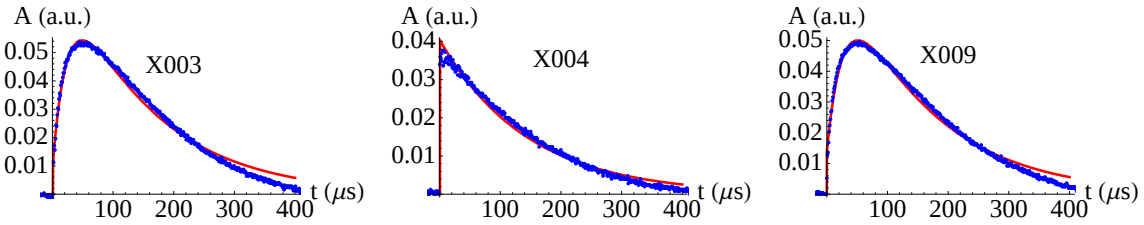

Figure 5.3: Response of different pyroelectric detectors at a wavelength of 1064 nm.

is to regard the specific time response of the pyroelectric detectors. In Fig. 5.3, the time response of the three different detectors is shown. They are measured at a wavelength of 1064 nm with a Nd:YAG-Laser (courtesy of S. Wesch). The detectors X003 and X009 reveal the effect of the black polymer coating, the detector X004 without any black polymer coating shows a fast response, as is expected.
The FEL at FELIX delivers macropulses with durations of a few μs. The macropulses themselves consist of micropulses spaced by 40 ns. The time constants of the pyroelectric detector, including the readout electronics, does not allow to resolve the individual micropulses. This has the consequences that the detectors are only able to measure the integrated signal over the macropulse. In order to deduce the expected signal for one pulse, the time profile of the FEL macropulses was measured with a X004 detector and a subsequent shaping with a Gaussian shaping-amplifier of $\sigma_t = 100$ ns. The output pulse of a Gaussian shaping-amplifier is sketched in Fig. 6.1 in the case of a pyroelectric detector with a black polymer coating. Every micropulse, the shaping-amplifier produces a Gaussian output pulse with a σ_t of 100 ns. The resulting output signal of the shaping-amplifier is the envelope of the macropulse, giving the time profile of the FEL macropulse. Some detector outputs, including also the shaping-amplifier, are shown for different pyroelectric detector types and wavelengths in Appendix B.

5.2 Synchrotron radiation port at BC3

An unavoidable effect of using magnetic chicanes for bunch compression is the emission of synchrotron radiation within the dipole magnets. At FLASH exist four sections with a notable dispersion: the first bunch compressor BC2, the second bunch compressor BC3, the section of the collimation system (called dog-leg), where the electrons with a certain energy deviation are removed, and the dipole in front of the beam dump at the end of the linac. Each section is equipped with a port to couple out synchrotron radiation. Except for one port at BC3, all ports are equipped with quartz (SiO_2) windows, which have a transmission cut-off at approx. 80 μm. Wavelengths in the range between 80 μm and 3 μm are suppressed. This range is especially interesting for bunch shape reconstruction by means of coherent radiation [27].

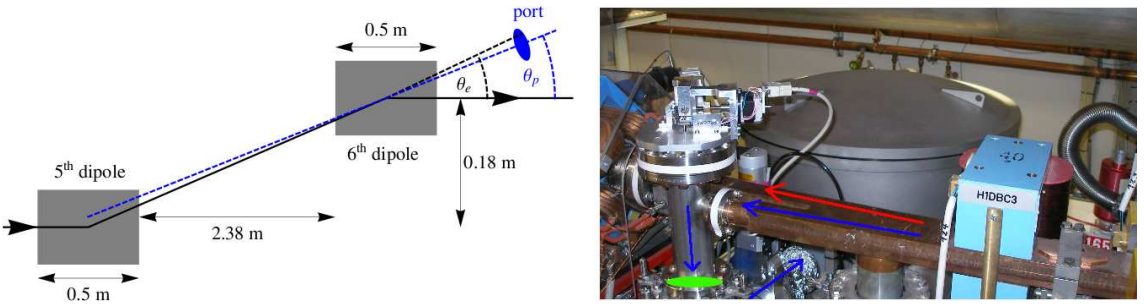

Figure 5.4: Left: The geometry of the last two dipoles of the second bunch compressor BC3. The electron orbits is indicated in black, the synchrotron radiation port in blue. Right: Picture of the beamline (electron orbit: red, synchrotron radiation: blue) with the mirror mechanics to couple out the radiation. The location of the diamond window is indicated in green.

For this work, the synchrotron radiation port behind the last dipole of BC3 was equipped with a synthetical diamond window, which has a flat transmission in the infrared, except for some absorption lines between 1 μm and 5 μm. The transmission curves for diamond and some more filters can be found in Appendix A.

In the left sketch of Fig. 5.4, the last two dipoles (5th and 6th) of the bunch compressor BC3 with the corresponding dimension are shown. The nominal bending angle is $\Theta_e = 3.85°$, but the vacuum chamber allows operation with bending angles in the range from $\Theta_e = 2.1°$ to $\Theta_e = 5.4°$ [14]. The synchrotron radiation port is pointing tangentially to the nominal orbit at the a position 84 mm behind the beginning of the last dipole. This results in the fixed angle of the port of $\Theta_p = 3.2°$ with respect to the beamline. The port dimensions are a height of 8 mm and a width of 26 mm. Depending on the particular bending angle, interference effects from the last and the second last dipole are possible and expected. Their implications on the synchrotron radiation spectrum will be investigated in chapter 7.

5.2.1 Electromagnetic shower background

The experiments with the synchrotron radiation of BC3 are performed within the accelerator tunnel, which is a controlled area due to the high radiation level during the operation of the linac. If high energy electron bunches are lost during the operation of the machine, they interact with the beamline and generate electromagnetic showers in the wall of the beam pipe. Above the critical energy which is given by

$$\boxed{E_{crit} = \frac{800\,\mathrm{MeV}}{Z + 1.2}} \tag{5.1}$$

with the atomic number Z of the target material, the energy loss is dominated by the emission of Bremsstrahlung. The corresponding photons can do pair production if the energy is larger than the rest energy of the electron-positron pair (1.022 MeV), and the process is repeated. The result is a cascade of photons, electrons and positrons. The

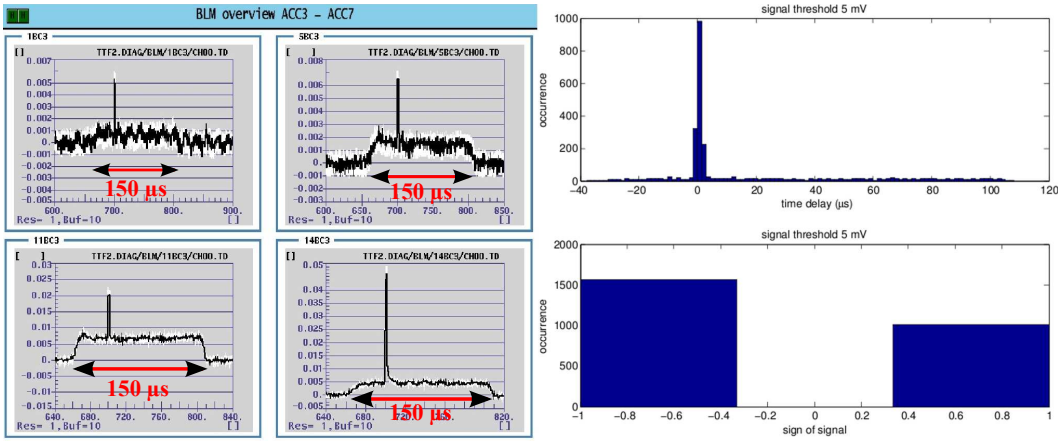

Figure 5.5: Left: Beam Loss Monitors (BLM) signals in the BC3 section. The horizontal axis is the time in μs. Right: The upper plot shows the measured detector counts above a specific threshold for 10000 different bunch trains as a function of time. The lower plot shows the corresponding signs of the signals (negative or positive).

radiation length

$$\boxed{X_0 \cdot \rho^{-1} = \frac{716.4 \cdot A}{Z(Z+1)\ln\left(\frac{287}{\sqrt{Z}}\right)} \mathrm{g/cm^2} \cdot \rho^{-1}} \tag{5.2}$$

with the atomic mass A [28] and the material density ρ, defines the length in which the electron energy has dropped to $1/e$ of its initial energy. The depth of the shower maximum, in units of radiation lengths, can be estimated by

$$\boxed{t_{max} \approx \ln\left(\frac{E_i}{E_{crit}}\right)} \tag{5.3}$$

with the initial energy E_i. Table 5.2 lists some material properties that are relevant for the FLASH linac. In the case of the shielding of sensitive electronics or experimental equipment, the shielding geometry has to be chosen carefully. If the thickness of the shielding material is below or equal to the shower maximum depth, the situation gets worse than before. In order to shield in an effective way, a material with a thickness of at least 20 radiation lengths has to be used. At FLASH, there are two contributions to the electromagnetic shower backgrounds. The first one is the beam loss due to a mismatched

material	E_{crit}(MeV)	X_0/ρ(cm)	t_{max} at 500 MeV
air	84	30000	1.78
iron	20.7	1.76	3.18
lead	7.4	0.56	4.21

Table 5.2: Data concerning electromagnetic showers for an electron energy of 500 MeV.

optics, the second one is due to dark current that consist of electrons which do not belong to the electron bunches. A main part of the dark current is generated by field emission

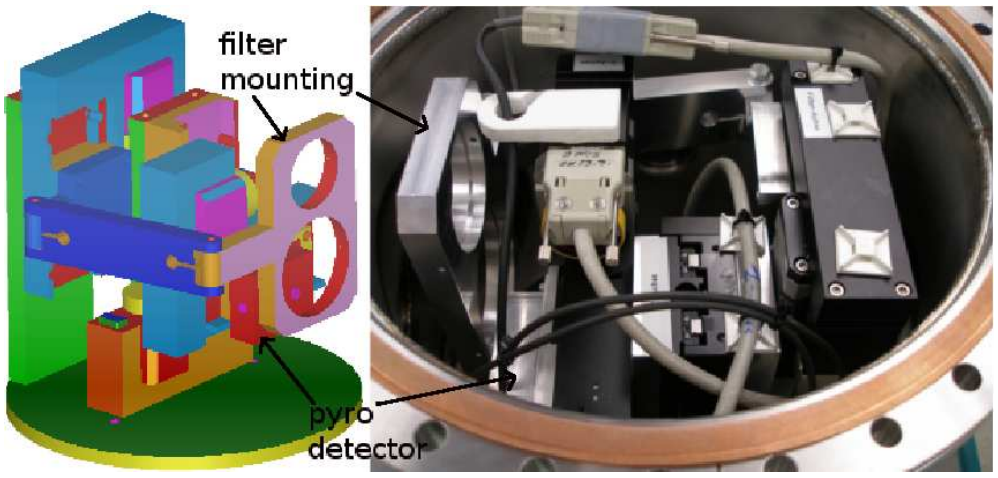

Figure 5.6: Left: CAD-drawing of the transverse scanning device (courtesy of B. Beyer). The filter mounting and the pyroelectric detector are indicated by arrows. Right: A picture of the transverse scanning device within the vacuum tank.

from the edges and the surface of the photocathode [29]. The left plot of Fig. 5.5 shows the display of the Beam Loss Monitors (BLM) in the section of BC3. The horizontal axis is the time and the vertical axis is the BLM-signal. One observes temporally long but weak signals as well as short spikes. The first part is due to the dark current, which has the same time profile as the power filling of RF gun. The second part is due to a local beam loss. The same time signature was found for the induced noise in the pyroelectric detectors. The right plot of Fig. 5.5 shows detector events without any synchrotron radiation arriving at the detector. The comparison with the BLM shows that the time profiles are identical. The occurrence of both, positive and negative signals, indicates that the noise is produced in the electronics itself and not by energy deposited in the detector crystal which would always produce positive output signals. Irradiation with radioactive sources identified two transistors of the pre-amplifier as to be the origin of the generated signals.

5.3 Transverse scanning device

In order to detect and characterise the transverse distribution of the synchrotron radiation, a transverse scanning device was installed at the synchrotron radiation port at BC3 described above. This device consists of two motors perpendicular to each other and enables the scanning of the mounted pyroelectric detector in a two-dimensional plane. This plane is aligned perpendicular to the incoming synchrotron radiation such that the transverse distribution can be investigated. The used pyroelectric detector is the X004 type without any black polymer coating. The detector signals are processed by a pre-amplifier and a subsequent Gaussian shaping-amplifier with a shaping-time of 250 ns.

In order to get further informations about the dependence of the transverse distribution on the wavelengths and about the spectral content itself, a third motor with a filter

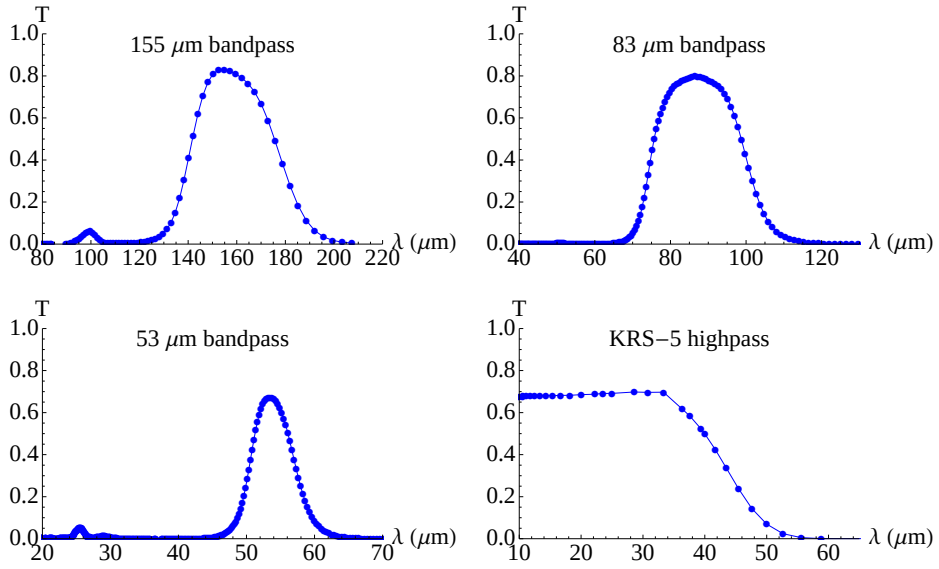

Figure 5.7: Compilation of the used filters: The plots show the transmission characteristics.

mounting was installed. All motors are remote-controlled. Figure 5.6 presents both a CAD-drawing (Computer Aided Design) and a picture of the whole device. In order to suppress absorption of the infrared radiation due to water vapour in the air, the setup is mounted in a vacuum chamber with a pressure in the order of 10^{-4} mbar.
For the detection and characterisation of the coherent part of the emitted synchrotron radiation, the observed wavelength has to be in the order of or longer than the length of the electron bunches. In the case of FLASH, the range of coherent radiation is in the infrared. For spectral measurements with filters, they have to be permeable in this range. In Fig. 5.7, the transmission characteristics of the used filters are shown in a compact form. For detailed informations, enlarged plots can be found in the Appendix A.

5.4 Spectrometer

One of the most substantial informations about any kind of electromagnetic radiation is its spectral content. This applies particularly to the case of coherent radiation from electron bunches, where the information of the longitudinal shape is contained in the spectrum. For spectral measurements of coherent radiation in the infrared, the use of reflective blazed gratings turned out to be a powerful method [30].

5.4.1 Reflective blazed gratings

Reflective blazed gratings consist of a support bulk with an imprinted periodic sawtooth structure (see the left sketch of Fig. 5.8). Except for the master gratings, the support bulk is mainly composed of glass and synthetics. The reflectivity is accomplished by specific

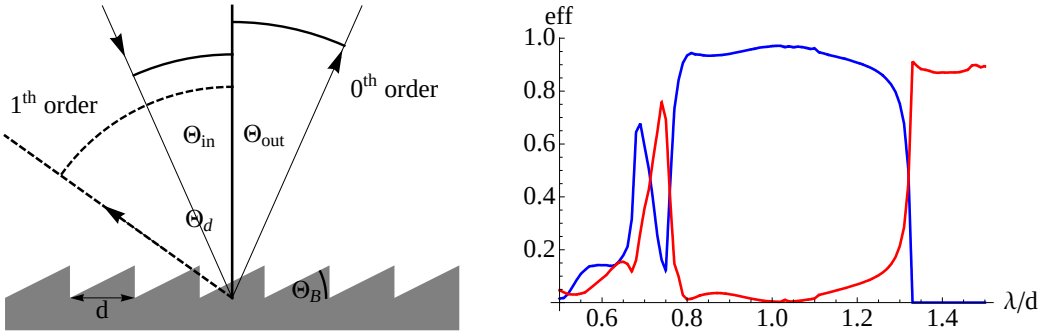

Figure 5.8: Left: Geometry of a reflective blazed grating. Right: Efficiency for a reflective blazed grating with an incoming angle $\Theta_{in} = 19°$ and a blaze angle $\Theta_B = 26.7°$ (first order: blue, zeroth order: red).

coatings with metals, e.g. aluminium. The reflective blazed gratings are characterised by two quantities.

One quantity is the pitch d of the periodic structures that affects the covered wavelength range as well the angular dispersion, both described by the grating equation

$$\boxed{m \cdot \frac{\lambda}{d} = \sin(\Theta_d) + \sin(\Theta_{in})} \tag{5.4}$$

with the m^{th} order of diffraction, the incoming angle Θ_{in} and the diffraction angle Θ_d. Instead of the pitch, the groove density $g = 1/d$, which defines the number of grooves per length interval, is often used. Using the grating equation in (5.4), the angular dispersion is given by

$$\boxed{\frac{d\lambda}{d\Theta_d} = \frac{d}{m}\cos(\Theta_d) = \frac{1}{m \cdot g}\cos(\Theta_d)}. \tag{5.5}$$

Large groove densities result in small covered wavelength ranges but also in a good resolution. Both can also be affected by the order m of diffraction. The considerations above are valid for any type of grating.

The other quantity charactersing a reflective blazed grating is the blaze angle Θ_B that defines the tilt of the sawtooth structure. Using an ordinary grating without any blaze angle, most of the intensity if reflected into the zeroth order. This zeroth order yields no dispersion, so that it cannot be used for any wavelength decomposition. Introducing a blazed structure makes it possible to shift the intensity maximum to the first order. According to (5.5), this first order results obviously in dispersion.

For any kind of application, the efficiency of a grating has to be known very well. The efficiency specifies which fraction of the incoming radiation is distributed into the different orders. In case of a nominal incoming angle $\Theta_{in} = 19°$ and a blaze angle $\Theta_B = 26.7°$, the efficiency results in large and wide first order which is sharply separated from the zeroth

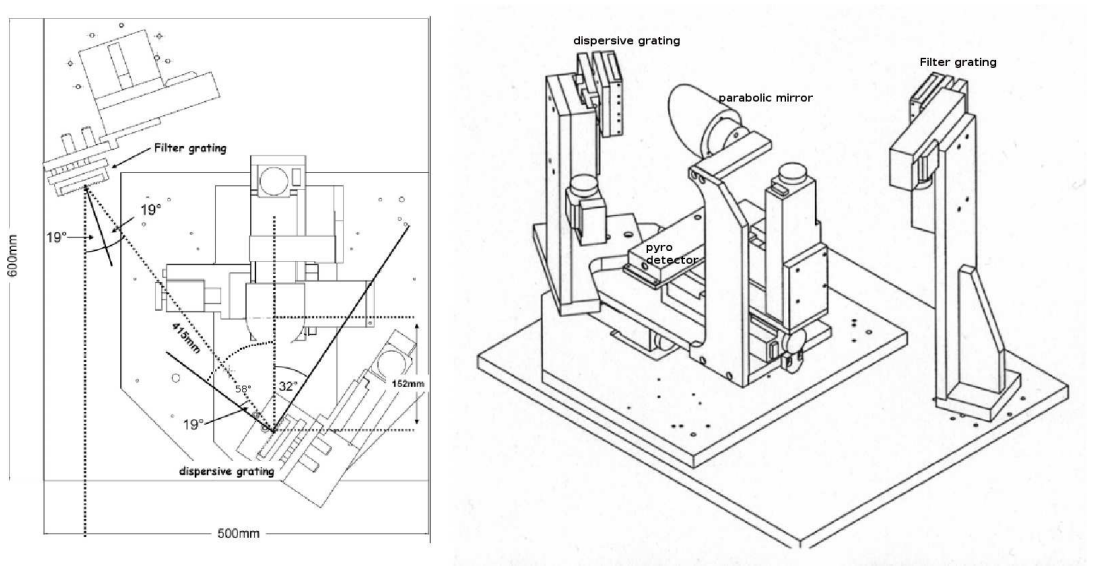

Figure 5.9: Two drawings with different views of the rotating mirror spectrometer. The basic components are labelled.

order. For this configuration, the grating efficiency for the zeroth and the first order can be seen in the right plot of Fig. 5.8. The efficiencies are calculated using the software GSolver [27, 30] and are given as a function of the dimensionless parameter λ/d.

5.4.2 Rotating mirror spectrometer

For the spectral measurements, a rotating mirror spectrometer was used. The drawings in Fig. 5.9 show two different views of the spectrometer assembly. The basic components are the filter grating, the dispersive grating, the rotatable focusing parabolic mirror and the pyroelectric detector.

For a specific wavelength range that is to be investigated by the dispersive grating, the filter grating is operated in zeroth order and acts as a mirror. Wavelengths shorter than this specific range are dispersed in the first order by the filter grating. The purpose of this operation is to suppress the effects of artificial signals due to second order radiation of the dispersive grating. It can not be distinguished between radiation with a wavelength of $(\lambda/1) \cdot 1$ from the first order and radiation with a wavelength of $(\lambda/2) \cdot 2$ from the second order. The only way is to filter the short wavelengths by means of the filter grating. For each dispersive grating, a specific filter grating has to be chosen.
The dispersive grating is operated in first order. The radiation provided by the filter gratings is dispersed in different angles dependent on the corresponding wavelength. Each grating mount is able to host at least two gratings.

A rotatable parabolic mirror with the focal length of $f = 152\,\mathrm{mm}$ is used to focus the radiation on a pyroelectric detector of type X003. The rotary motor of the paraboloid can cover an angular range of 60°.

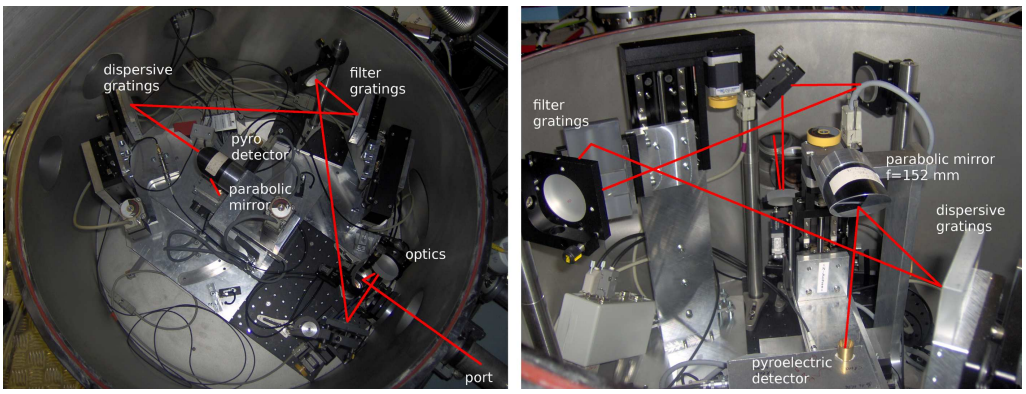

Figure 5.10: Two pictures with different views of the rotating mirror spectrometer inside the vacuum chamber. The optical path is indicated in red.

The whole device, including different optics to ensure the correct path of the incoming radiation, is mounted in a vacuum chamber with a pressure in the order of 10^{-4} mbar. The vacuum chamber for the spectrometer replaced the vacuum tank for the transverse scanning device at the synchrotron radiation port at BC3. In Fig. 5.10, two pictures of the assembled spectrometer are shown. The left picture shows the whole setup with the optical path indicated in red. The right picture reveals more details, especially of the optics to guide the radiation onto the filter grating. For the calculated efficiencies, the incoming radiation has to be horizontally polarised. Due to the fact that synchrotron radiation is dominated by the horizontal polarisation (see chapter 2) and poor intensity is expected, the measurements were performed without any polariser.

6 Measurements and results

6.1 Pyro detector calibration

The pyro detector calibration measurements were performed during two days at FELIX in the Netherlands. The first day, infrared pulses in the wavelength range from 5 μm to 40 μm were provided by FEL-2 (see Fig 1.6). The second day, the wavelength range was extended to 110 μm by means of FEL-1. Both days, FELIX was operated with a macropulse repetition rate of 5 Hz and a micropulse repetition rate of 25 MHz. This means that over the whole macropulse, the micropulses are separated by 40 ns. The time profile of the macropulse depends on the wavelength and is of the order of 10 μs, resulting in a large number of micropulses. The particular time profile for each wavelength was measured with a pyroelectric detector of type X004 with a subsequent fast shaping-amplifier with a shaping-time of 100 ns. This detector combination produces Gaussian pulses with $\sigma_t =$ 100 ns with the same repetition rate as the micropulses. The envelope of this train of Gaussian pulses reflects the time profile of the macropulses. In appendix B, some time profiles for different wavelengths are shown. The outputs of the pyroelectric detectors of the types X003 and X009 are also shown. Without any further analysis, the influence of the black polymer coating, especially at short wavelengths, is already visible in these plots. The energy for each macropulse was measured with a thermo-pile power meter. The energy output of FELIX as a function of the wavelength is shown in the right plot of Fig. 5.2. Both the measurement with the pyro detector and the measurement with the power meter are averaged over 32 shots.

6.1.1 Mathematical description of the analysis

The goal of the pyroelectric detector calibration is to obtain the responsivity R and the non-acting fraction f of the black polymer coating for the pyroelectric detector of the types X003, X004 and X009. The non-acting fraction f has the attribute of a transmission with values equal to 1 if nothing is absorbed. The responsivity R has the units mV/ nJ. Both quantities R and f affect the detector output as well the part which can be amplified by the shaping-amplifier.
The responsivity R and the fraction f are defined with the response of a short radiation pulse acting at $t = t_0$ with a amplitude of a_0, given by

$$\boxed{out(t, t_0, a_0) = a_0 \cdot R \cdot [f + (1 - f) \cdot (1 - e^{-(t-t_0)/\tau_p})] e^{-(t-t_0)/\tau_e} \cdot \Theta(t - t_0)} \qquad (6.1)$$

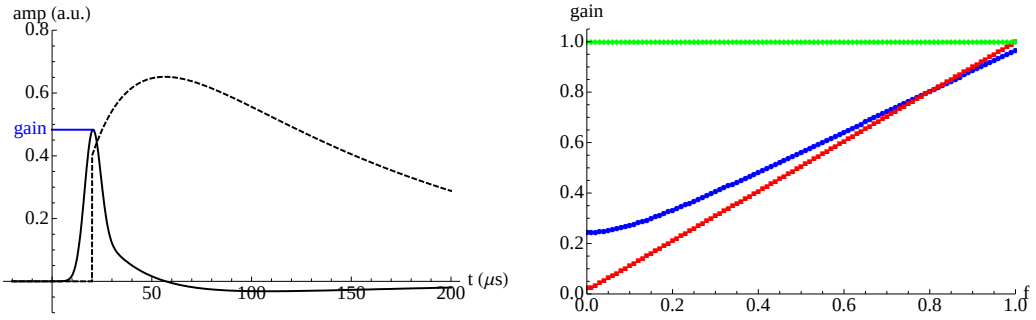

Figure 6.1: Left: Detector output for the case $f = 0.4$ and $a_0 \cdot R = 1$ (in arbitrary units). The pre-amplifier is indicated with a dashed line and the shaping-amplifier with a thick line. Right: Gain of the shaping-amplifier as a function of f for the case $a_0 \cdot R = 1$ (in arbitrary units): no coating + $\sigma_t = 250\,\text{ns}$: green, coating + $\sigma_t = 250\,\text{ns}$: red, coating + $\sigma_t = 4\,\mu\text{s}$: blue.

with the two different time constants τ_p of the black polymer coating and τ_e of the detector electronics. The function $\Theta(t - t_0)$ is the Heaviside step function with $\Theta(t - t_0) = 0$ for $t < t_0$ and $\Theta(t - t_0) = 1$ for $t > t_0$. In the case without any coating, where f is equal to 1, the output is a decreasing exponential function starting at $t = t_0$ with the amplitude $a_0 \cdot R$. The shape of the output depends on the particular values of f, R and the time constants. The left plot of Fig. 6.1 shows the detector output (dashed) of an X003 type for the case $f = 0.4$ and $a_0 \cdot R = 1$ (in arbitrary units), with the corresponding output of a shaping-amplifier with a shaping-time of $\sigma_t = 4\,\mu\text{s}$. The gain of a shaping-amplifier is associated with the amplitude of the shaping-amplifier output, which depends also on the specific values f and R and as well on the shaping-time. The right plot of Fig. 6.1 shows the gain of a detector with coating (X003) for two shaping-times, and the gain for a detector without any coating (X004).

In order to model the three detector types X003, X004 and X009 according to Eq. 6.1, the time constants τ_p and τ_e have to be known. The determination of these time constants was performed with a measurement of the detector response to a short single pulse of a Nd:YAG-Laser at a wavelength of 1064 nm. The detector outputs as the response to a short single pulse as well the fit for each detector is shown in Fig. 5.3. A fit algorithm in Mathematica was used to determine the time constants for the model used in Eq. (6.1). They are listed in table 6.1 for each detector. The time constant τ_e is a property of the

time constant	X003	X004	X009
τ_p (μs)	29 ± 1	none	34 ± 1

Table 6.1: Determined time constants of the detector.

amplifier electronics and it has the same value of $\tau_e = (145 \pm 1)\,\mu\text{s}$ for the three detectors. The measurements at FELIX were done with a micropulse separation of 40 ns. The result-

ing total output of the detector for the whole macropulse is given by

$$\boxed{out_{tot}(t,t_0) = \sum_{i=1}^{N} p_e(t+i\Delta t, t_0) out(t+i\Delta t, t_0, 1)} \tag{6.2}$$

with p_e, the energy of each micropulse, N, the number of all micropulses within a macropulse and $\Delta t = 40\,\text{ns}$, the separation between the micropulses. The energy p_e of the micropulse is a function of time which represents the envelope of the macropulse. The function p_e was determined by measurements of the time profile by using a pyroelectric detector of type X004 and a subsequent shaping with $\sigma_t = 100\,\text{ns}$. The measured timing profile was then normalised to the measured energy of the macropulse. The number N of all micropulses within a macropulse is given by the duration of the macropulse multiplied with the repetition rate of the micropulses.
The final analysis was performed with a numerical fit algorithm in Mathematica. The algorithm used the expression (6.2) with the model of the detector output defined in (6.1) and the measured normalised micropulse energy $p_e(t, t_0)$. The input data for the fit is provided by the measured signal of each detector. In appendix B, some detector outputs at different wavelengths are shown.

6.1.2 Data analysis

The data analysis includes the application of the fit algorithm for every wavelength and for each of the three detectors. The result of the fit provides quantities R and f. In the case of the pyroelectric detector without coating (X004), the quantity f is defined to be equal to 1. Figure 6.2 shows the determined responsivity R as a function of the wavelength for the X003 type. The upper row shows the whole range of the responsivity with two different regions indicated by two dashed vertical lines. The right dashed line indicates the border of the working range of the used attenuator. The left dashed line indicates the cut-off for the range used in the analysis. The border of the working range of the used attenuator is at $36\,\mu\text{m}$ according to the data sheet. In the lower row, the range of the responsivity is shown for the two cut-offs at $32\,\mu\text{m}$ and at $34.5\,\mu\text{m}$. The motivation for this cut-off introduced at lower values is that the extreme increase in the responsivity is only observed during the measurements with an attenuator. During the measurements in the wavelength range from $35\,\mu\text{m}$ to $60\,\mu\text{m}$ (black curve), no attenuator was used. This means that the wavelength range from $35\,\mu\text{m}$ to $40\,\mu\text{m}$ is covered by two independent measurements, but one was performed with an additional attenuator. Another motivation for the introduced cut-off is that there is no physical reason for the extreme increase in the responsivity, except for a non-working attenuator. The phenomenon of the increasing responsivity at the border of the working range of the attenuator was observed for each detector type for the same reason. For the final results presented in the next subsection, a cut-off of $32\,\mu\text{m}$ was used.

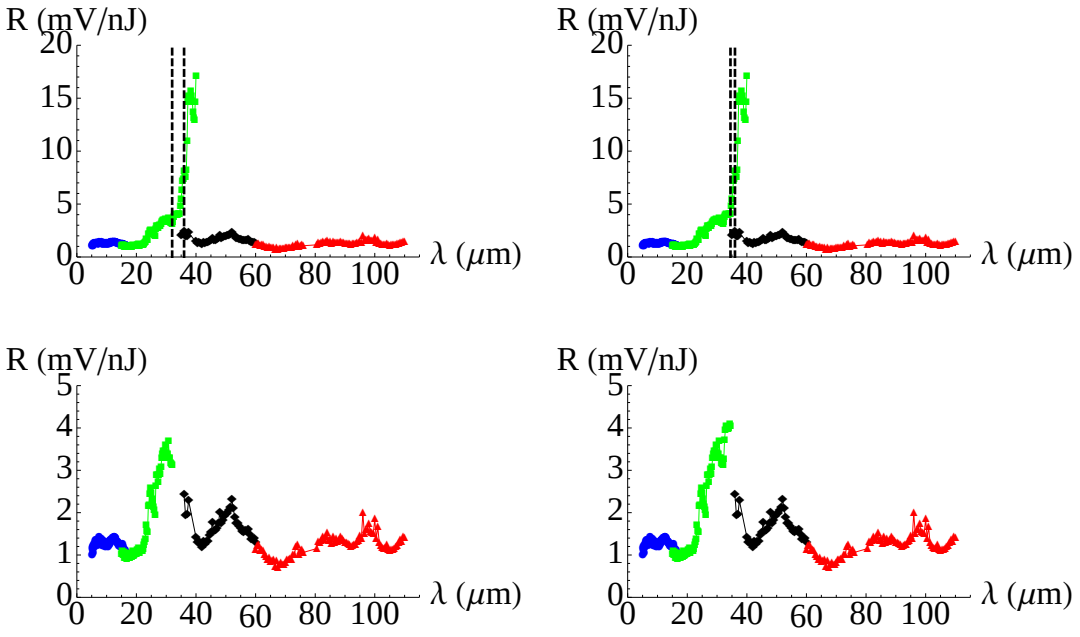

Figure 6.2: Responsivity R for the pyroelectric detector of the type X003 as a function of the wavelength: Top: Full range with the indicated border at 36 μm and the cut-off at 32 μm (left) and at 34.5 μm (right). Bottom: The range modified by the cut-offs.

6.1.3 Results of the pyro detector calibration

The results of pyroelectric detector calibration have to be discussed for different wavelengths, divided into the ranges from 5 μm to 40 μm, from 40 μm to 70 μm and from 70 μm to 110 μm. In Fig. 6.3, the final result of the responsivities for the three different detectors X003 (red), X004 (green) and X009 (blue) are shown. Fig. 6.5 shows the short-wavelength part of the responsivities with enlarged wavelength scale. To understand the wavelength-dependence of the responsivity, the non-acting fraction of the coating f, shown in Fig. 6.4, has to be included in the discussion. All plots in this subsection have the same colour coding: X003 (red), X004 (green) and X009 (blue).

The wavelength range from 5 μm to 40 μm reveals a strong influence of the coating with non-acting fractions of $f < 1$. Especially the detector of the type X004 without coating $f = 1$ shows strong oscillations in the range below 14 μm (see Fig. 6.5). This is understood by means of the absorption effects of $LiTaO_3$ as described in chapter 4 about pyroelectricity. Below 10 μm, $LiTaO_3$ becomes again transparent, resulting in absorption resonances due to multiple internal reflections. For the detector types X003 and X009, this effect is suppressed by the absorption in the black polymer coating. In general, the detector types X003 and X009 behave similarly and show a larger responsivity compared to the X004 type. This can be explained by the enhanced absorption due to the black polymer coating.

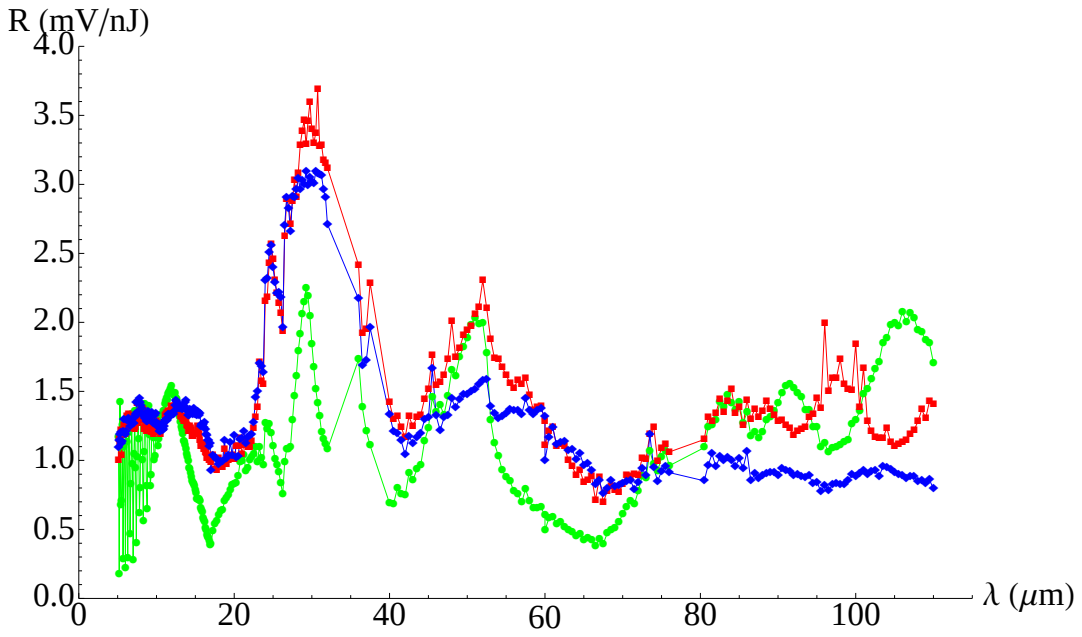

Figure 6.3: Responsivities for the different pyroelectric detectors X003 (red), X004 (green) and X009 (blue).

The wavelength range from 40 μm to 70 μm shows two different dependencies of the detectors. From 40 μm to 50 μm the detectors X003 with coating and X004 without coating behave similarly. This can be explained by the fact that in this range, the influence of the coating becomes negligible (see 6.4). From 50 μm to 70 μm the detectors X003 and X009 show the same dependence again. In the wavelength range from 40 μm to 70 μm only a slight influence of the coating with $f \approx 1$ can be observed. The responsivity is more and more affected by the $LiTaO_3$ and the different NiCr layers, instead of the black polymer coating. The detectors X003 and X004 reveal a larger responsivity compared to the X009 type. This behaviour is expected due to the different thicknesses of the NiCr layers (see Fig. 4.4).

In order to compare the measured data with the model of the pyroelectric detector made in chapter 4, a fit of the model with the data of the X004 type was done. The fit variables are the thicknesses of the $LiTaO_3$ and the two Ni layers. If the oscillating data below 20 μm are removed for the fit, the model shows good agreement with the data. The obtained fit parameters are shown in table 6.2. The thickness of the $LiTaO_3$ shows good agreement with the design value. Both the data and the plot is shown in Fig. 6.6.

X004	frontside	middle	backside
design	5 nm NiCr	20 μm $LiTaO_3$	20 nm NiCr
fit	5 nm Ni	23 μm $LiTaO_3$	15 nm Ni

Table 6.2: Fit results for detector X004.

The main uncertainties of the model are due to the lack of the optical constants of the

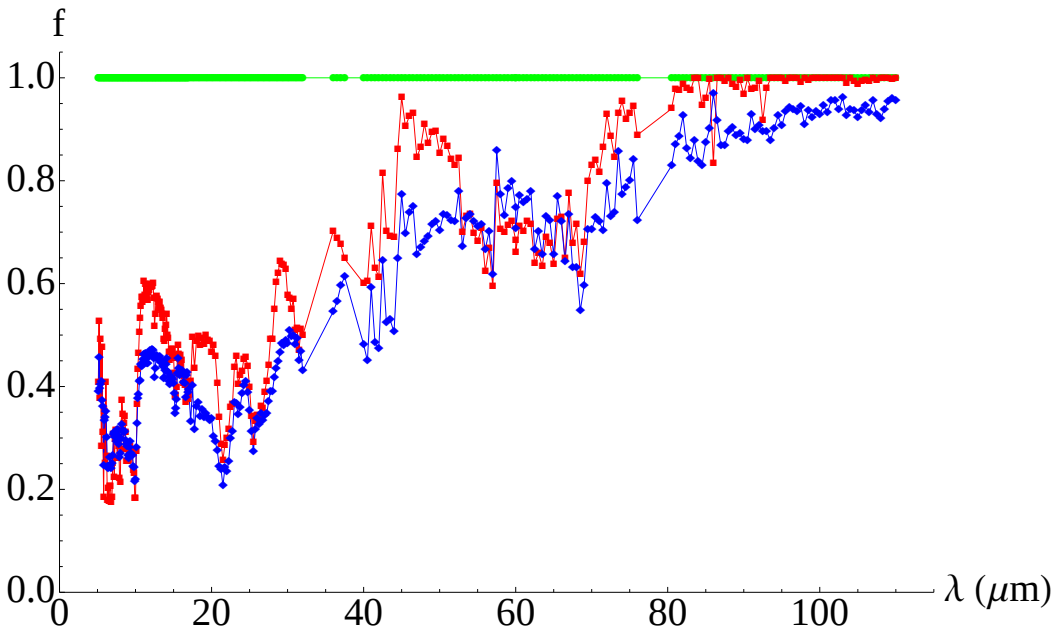

Figure 6.4: Non-acting fraction of the black polymer coating for the different pyroelectric detectors X003 (red), X004 (green) and X009 (blue).

NiCr. The model uses only an approximation of the optical constants for Ni. Nevertheless, the model shows a qualitative agreement, which is a hint for the flat responsivity of the power meter in this range.

6.1.4 Summary of the pyroelectric detector calibration

The measurements at FELIX yield the following results:

- Responsivity R of the pyroelectric detector X003, X004 and X009 in the wavelength range from 5 μm to 110 μm (Fig. 6.3).
- Non-acting fraction f of black polymer coating of the pyroelectric detector X003 and X009 in the wavelength range from 5 μm to 110 μm (Fig. 6.4).
- Black polymer coating has no effect at long wavelengths, where it becomes transparent.
- The theoretical model shows a qualitative agreement with the measurements.

The main error source for the calibration is the uncertainty of the response function of the power meter used. The discrepancy of the two power meters used inside the set up by up to factor 2 indicates a large uncertainty of the overall absolute calibration of these devices. The good agreement between all three power meters concerning the wavelength dependence of the radiation intensity indicates, that their response is actually reasonably flat, especially since they are based on different detection principles. This is further supported by the good agreement of the found responsivity with the theoretical expectations where applicable.

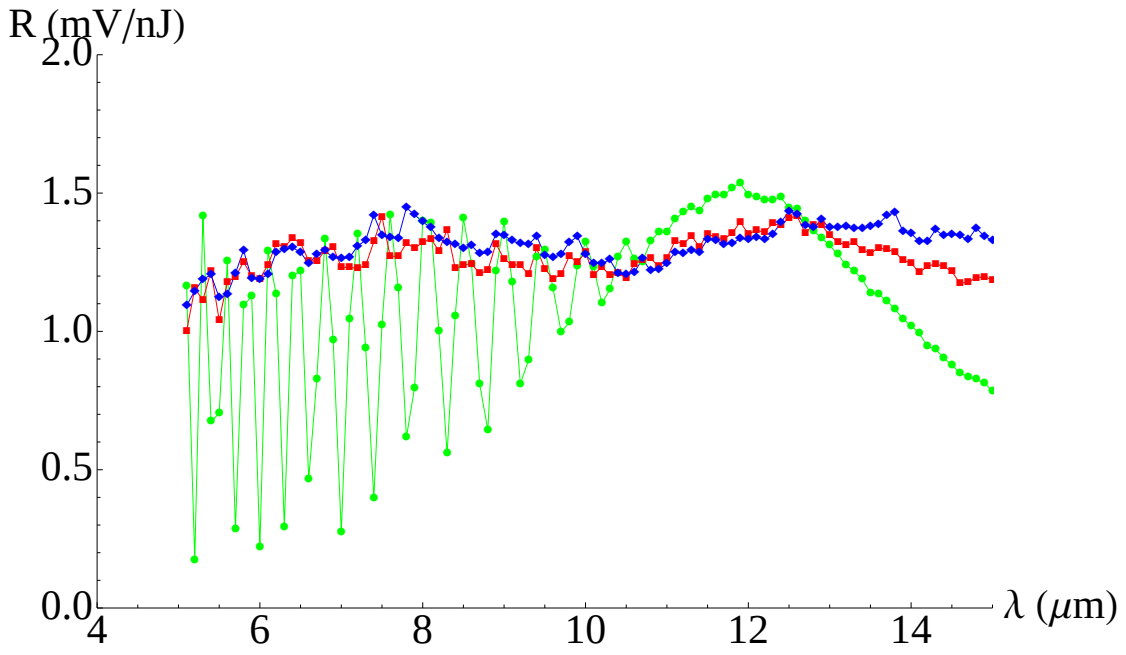

Figure 6.5: Responsivities for the different pyroelectric detectors X003 (red), X004 (green) and X009 (blue) in the short-wavelength range.

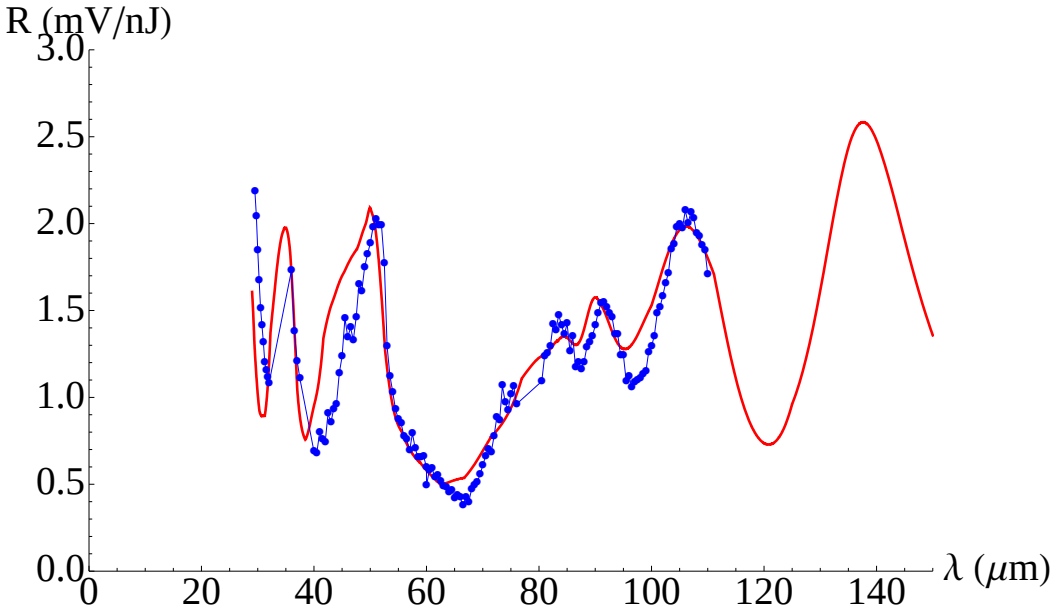

Figure 6.6: Fit of the pyroelectric detector model used in chapter 4 with the data of the X004 type. (data: blue, fit: red)

6.2 Transverse profiles of the coherent synchrotron radiation at BC3

This section deals with a qualitative analysis of the measured coherent synchrotron radiation of the last port at BC3. This port is equipped with a diamond window which has a

flat transmission curve down to the optical range. Table 6.3 gives an overview about the filters used, the bandwidth (FWHM), the averaged filter transmission and the averaged pyro responsivity. For the measurements, a pyroelectric detector of the type X004 with a shaping amplifier of $\sigma_t = 250\,\mathrm{ns}$ and an amplification factor of 100 was used. The area of the detector is $2 \times 2\,\mathrm{mm}^2$. For the KRS-5 highpass filter, the bandwidth was estimated to

filter	bandwidth (FWHM) (μm)	avg. transmission	avg. pyro responsivity ($\mathrm{mV/nJ}$)
no filter	-	1	1.11
bandpass 155	$38\,\mu$m	0.7	1.45
bandpass 83	$25.5\,\mu$m	0.69	1.19
bandpass 53	$7\,\mu$m	0.56	1.41
highpass KRS-5	$40\,\mu$m	0.65	1.06

Table 6.3: Data of the filters used and detector responsivities.

be in the range from $45\,\mu$m down to $5\,\mu$m. The average of the transmission and the pyro efficiency was determined over the wavelength range of the bandwidth. In the case without filter, the averaged pyro efficiency was determined over the whole range measured in the calibration measurements in section 6.1. For all filters, the transverse intensity distribution was measured with and without focusing of the coherent synchrotron radiation. Due to the high intensity in the case without any filter, only the unfocused distribution was measured. In all measurements, the bunch charge was in the range of 0.5 nC to 1 nC. The electron beam energy at BC3 was in the range $(450 \pm 30)\,\mathrm{MeV}$, but according to subsection 2.3.2 the spectrum should be independent of the electron energy at large wavelengths.
Fig. 6.7 shows the transverse intensity distribution for the case without any filter. The shown distribution is affected by a nominal rotation of 87° with respect to the coordinate system of the accelerator with the deflecting plane in the horizontal direction. This rotation is caused by the mirror which guides the radiation perpendicular to the direction of the electron beam (see Fig. 5.4). The nominal value of 87° results from the tilt angle of the beamline of approx. 3°. Nevertheless, rotation angles of more or less than 87° are possible, dependent of the actual position of the moveable mirror. Fig. 6.8 to Fig. 6.11 show the intensity distributions for the unfocused case in the left and for the focused case in the right. All plots are indicating two separated maxima. For the unfocused distribution in the case without any filter and in the case with the $83\,\mu$m bandpass filter, the two maxima are evident. For the other cases, the maxima are only visible if the radiation is focused. This is mainly due to the reduced intensity at short wavelengths. In the case of the $155\,\mu$m bandpass filter, the second maximum seems to be suppressed. Chapter 7 considers possible explanations for the effect of two maxima within the intensity distributions.
The wavelength dependence revealed by these measurements is the decreasing intensity for short wavelength. This effect can be explained by the decreasing form factor in case the observed wavelength is comparable or smaller than the bunch length itself. Nevertheless, the

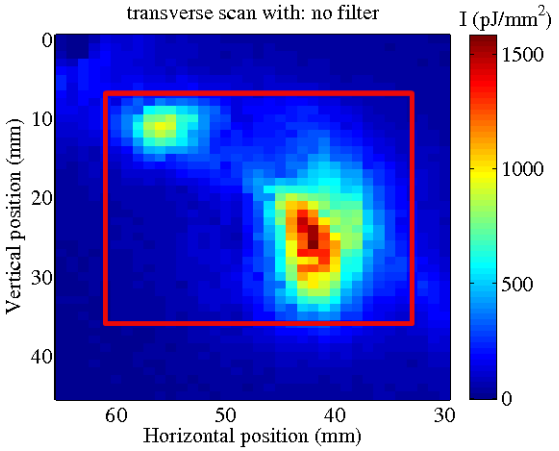

Figure 6.7: Transverse intensity distribution measured without any filter for $Q = 0.8\,\mathrm{nC}$. An additional frame of the dimensions $28.5\,\mathrm{mm} \times 28.5\,\mathrm{mm}$ is indicated in red.

transverse distribution of the coherent synchrotron radiation seems to be of low intensity compared to other sources such as coherent transition radiation [30]. For the spectroscopic measurements using the rotating mirror spectrometer, the dimension of the smallest gratings are $58\,\mathrm{mm} \times 28.5\,\mathrm{mm}$. In order to prevent beam cut-offs and in particular artificial signals from other gratings, the beam dimension have to fit to the grating. Fig. 6.7 shows the transverse distribution in the case without any filter with an additional frame indicated in red. The frame has the dimensions $28.5\,\mathrm{mm} \times 28.5\,\mathrm{mm}$ which defines a rectangle with the minimum lengths of the grating in both dimensions. For spectroscopy, the whole beam can be used. Nevertheless, it has to be taken into account that the different maxima might contain different spectral content (see [31]).

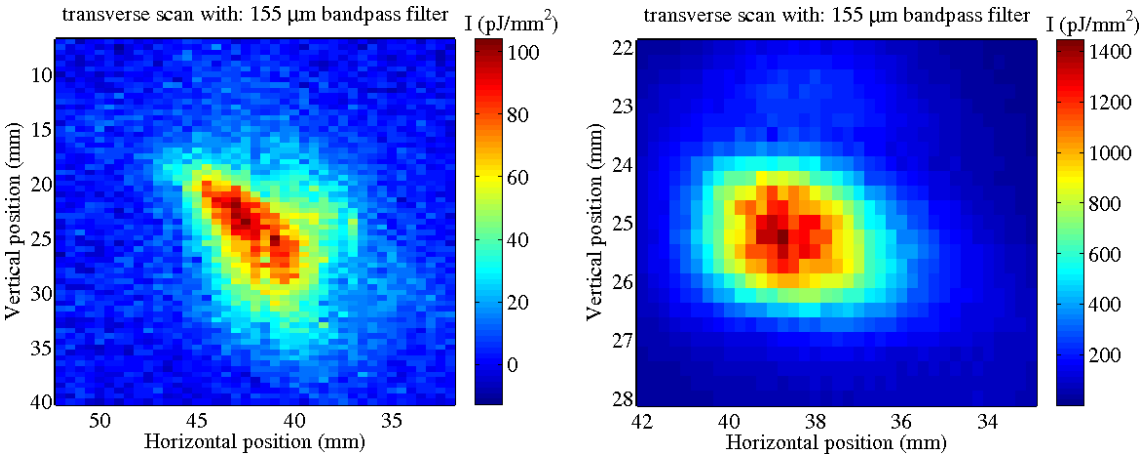

Figure 6.8: Transverse intensity distribution measured with a 155 μm bandpass filter. Left: Unfocused case for $Q = 0.6\,\mathrm{nC}$. Right: Focused case for $Q = 0.7\,\mathrm{nC}$.

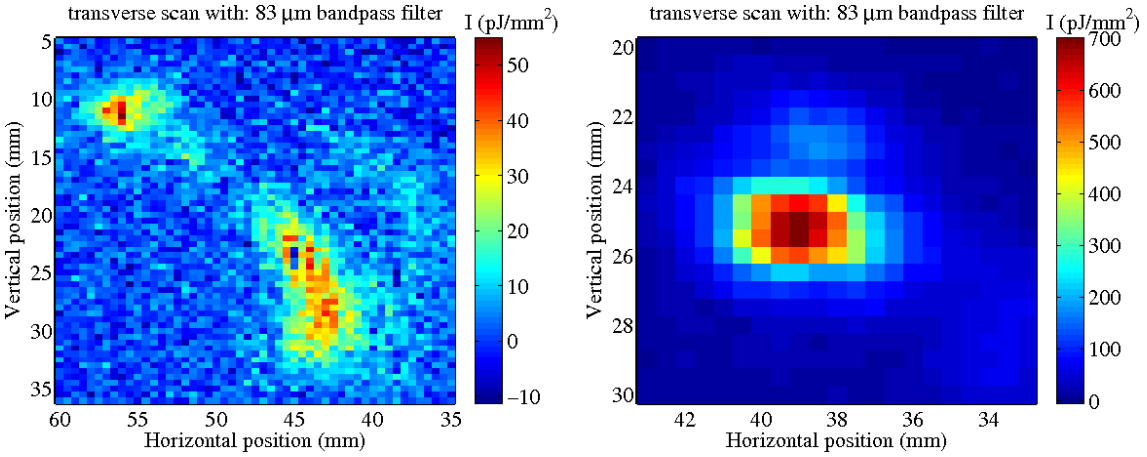

Figure 6.9: Transverse intensity distribution measured with a 83 μm bandpass filter. Left: Unfocused case for $Q = 0.7\,\mathrm{nC}$. Right: Focused case for $Q = 0.5\,\mathrm{nC}$.

6.2.1 Summary of the transverse intensity distribution measurements

The results of the transverse intensity distribution measurements can be summarised by:

- The transverse profile fits to the grating dimensions.
- A complex transverse intensity distribution comprising two maxima was revealed.
- The intensity of the transverse distribution is rather low.

The complex structure of the transverse intensity distribution is also a topic of Chapter 7. Especially, the low intensity of the coherent synchrotron radiation turned out to be limiting spectroscopic measurements.

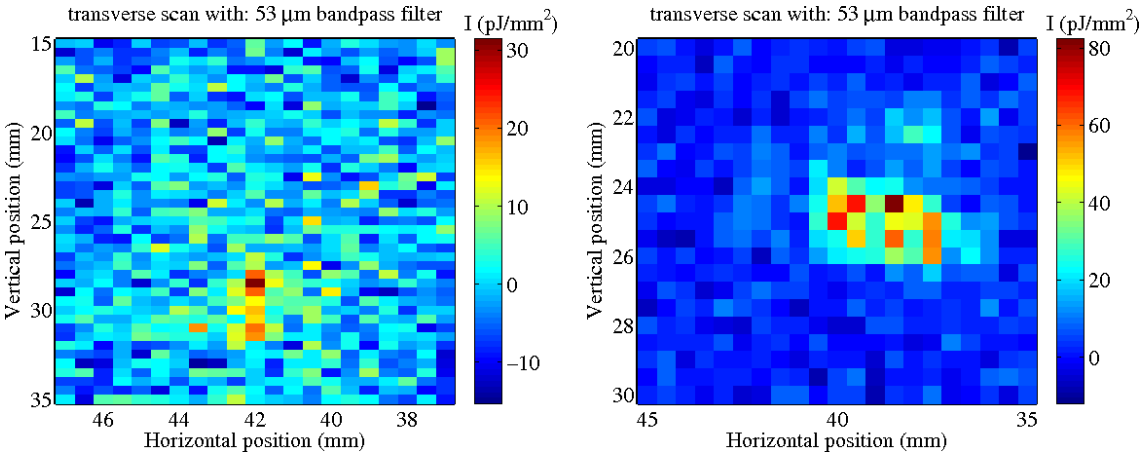

Figure 6.10: Transverse intensity distribution measured with a 53 μm bandpass filter. Left: Unfocused case for $Q = 1.0\,\mathrm{nC}$. Right: Focused case for $Q = 0.7\,\mathrm{nC}$.

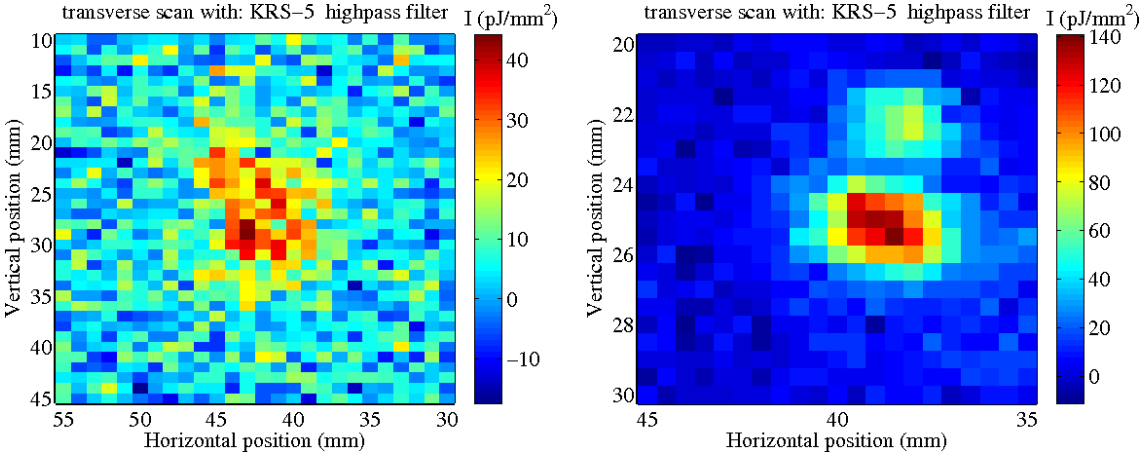

Figure 6.11: Transverse intensity distribution measured with a KRS-5 highpass filter. Left: Unfocused case for $Q = 0.8\,\mathrm{nC}$. Right: Focused case for $Q = 0.8\,\mathrm{nC}$.

6.3 Spectral measurements of the coherent synchrotron radiation

The measurements in section 6.2 show that the transverse intensity distributions of the coherent synchrotron radiation are of low intensity. To get a reliable signal-to-noise ratio, the signals have to summed over many bunches. In the case of the shaping-amplifier used with a shaping constant of $\sigma_t = 4\,\mu$s and the bunch repetition rate of 1 MHz, the detector output consist of a series of almost gaussian-shaped pulses with $\sigma_t = 4\,\mu$s, separated by $1\,\mu$s respectively. The total pulse is the sum of this series. According to the plot in Fig. 6.1, the precise form of the pulse depends on the non-acting fraction f of the black polymer coating resp. on the observed wavelengths.
The spectral measurements presented in the next subsections are performed with 20 bunches separated by 1 MHz. To further improve the signal-to-noise ratio, each measurement is averaged over 50 bunch-trains. In the following subsections, the referred gratings are labelled with Gx, x being the number of grooves per millimetre, e.g. G20 means a grating of 20 grooves per millimetre.

6.3.1 Data analysis and corrections

In order to yield absolute values of the measured spectral energy, great care in the analysis of the data has to be taken. There are a lot of corrections that have to be applied. These corrections can be divided in two main types, corrections concerning the data acquisition and corrections due to the different efficiencies of the detection geometry.
The corrections of the data acquisition include:

- conversion of the integrated signal of 20 bunches to the signal of one bunch
- impact of the black polymer coating on the pulse form
- responsivity of the pyroelectric detector of the type X003
- gain of the shaping-amplifier with $\sigma_t = 4\,\mu$s

The 20 bunches are producing a total detector signal with a duration longer than $30\,\mu$s. The data readout is performed using an analog-to-digital converter (ADC) with a sampling frequency of 1 MHz. The further analysis used the sum of a fixed number of 40 samples over the total detector signal. The precise form of the detector pulse depends on the acting of the black polymer coating. With the measured wavelength dependence due to the coating described in section 6.1, the conversion of the integrated signal of 20 bunches to the signal of one bunch, including the black polymer coating, can be derived. To yield the final pulse energy, the processed signal has to be corrected by the responsivity of the pyroelectric detector and the gain of the amplifier.
The corrections due to the different efficiencies of the detection geometry include:

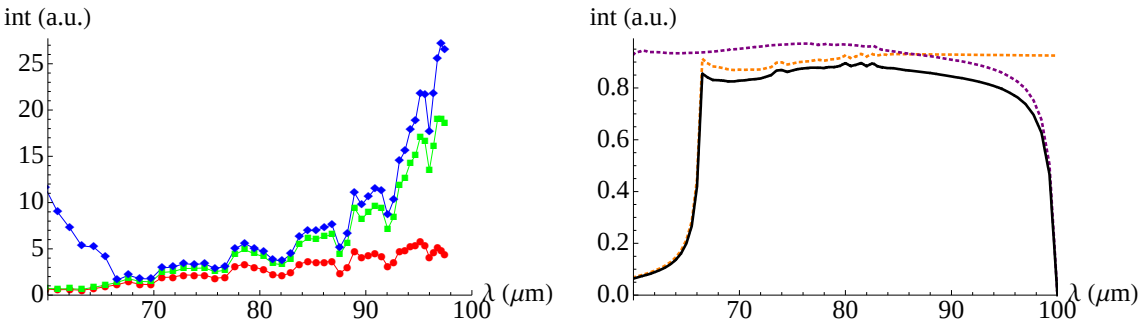

Figure 6.12: Left: Behaviour of the corrections due to dispersion strength (from red to green) and grating efficiencies (from green to blue). Right: Grating efficiency for the filter grating G20 and the dispersive grating G13.3 (zeroth order: orange, first order: purple, total: black).

- dispersion strength $\frac{d\lambda}{d\Theta} = \frac{1}{g}\cos(\Theta)$
- efficiency of the filter grating
- efficiency of the dispersive grating
- radiation transport efficiency of the beamline and the optics

The correction of the dispersion strength results in the fact that the wavelength interval $\Delta\lambda$, covered by a constant angle interval $\Delta\Theta$, is angle-dependent. The efficiencies of the gratings have been determined by simulations and verified experimentally [30]. Fig. 6.12 illustrates the behaviour of the corrections due to the spectral wavelength density and the grating efficiencies. The red curve in the left plot shows the measured intensity without any correction of the detection geometry. Applying the correction of the dispersion strength (in the plot: from red to green), the long-wavelength part, i.e. large angles, is enhanced due to the cosine term. Further corrections due to the grating efficiencies (in the plot: from green to blue) increase the over-all intensity, especially at the boundaries. This follows from the low efficiency in these regimes (see the right plot of Fig. 6.12).
Except for the transport efficiency of the beamline and the optics, all correction are included in the following measurements. The radiation transport from the electron beam pipe to the experimental setup is accomplished by two focusing parabolic mirrors and a diamond window. The wavelength dependent transport efficiency was not calculated so far due to unknown intensity distributions in front of the transport beamline. Such calculations are based on radiation transport codes, which need the expected intensity distributions with the field and phase information as input.

6.3.2 Wavelength calibration

To obtain the design efficiency of the used gratings, shown in Fig. 5.8, the actually incoming angle of the radiation has to be $\Theta_{in} = 19°$. Other incoming angles result in different

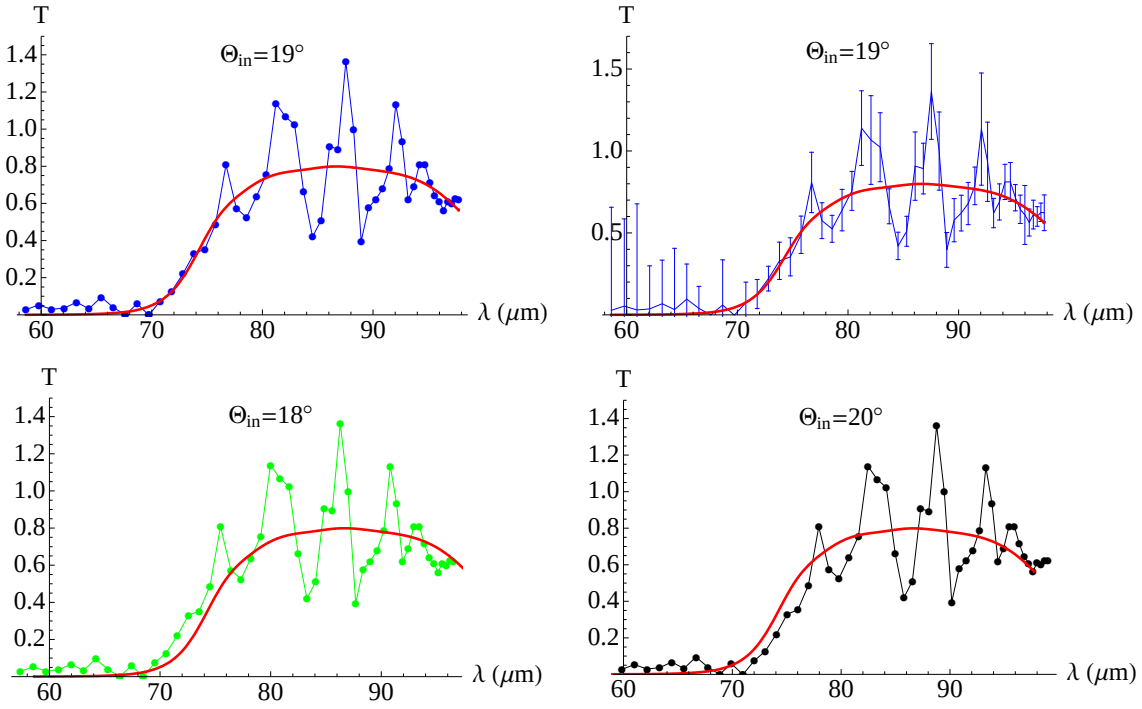

Figure 6.13: Wavelength calibration with the 83 μm bandpass filter (filter curve in red). Top row: Transmission with the nominal incoming angle of $\Theta_{in} = 19°$. Bottom row: Transmission with the shifted incoming angles of $\Theta_{in} = 18°$ and $\Theta_{in} = 20°$.

grating efficiencies and as well, according to Eq. 5.4, in other wavelengths at the same Θ_d. In order to determine the incoming angle Θ_{in} for the further analysis, a wavelength calibration with two different bandpass filters was performed. The intensity of the coherent synchrotron radiation was measured twice for the same grating and machine settings, the first time without any filter and the second time with a corresponding bandpass filter. In Fig. 6.13, the wavelength calibration in the case of the 83 μm bandpass filter is presented. The upper row shows the transmission characteristics for the nominal angle of $\Theta_{in} = 19°$. The lower row show the same measurement, but with the shifted incoming angle of $\Theta_{in} = 18°$ and $\Theta_{in} = 20°$. The incoming angle with the nominal value of $\Theta_{in} = 19°$ shows the best agreement compared with the other angles. In particular, the rising edge between 70 μm and 78 μm fits very well. The strong fluctuations between 78 μm and 92 μm can be explained by strong fluctuations of the horizontal beam position during the respective measurements (see Fig. C.4). In Appendix C, the entire wavelength calibration measurements with the additional horizontal beam positions are shown. In order to check the wavelength calibration a second time, a further measurement with 155 μm bandpass filter was performed. The results of this measurement are also shown in Appendix C. The plots in Fig. C.1 show again the best agreement for the nominal incoming angle $\Theta_{in} = 19°$. The wavelength calibration measurements result in two facts:

- The optics is well matched to the nominal incoming angle of $\Theta_{in} = 19°$.

- Indications of influence of the horizontal beam position on the measured intensity.

6.3.3 Spectra for different machine settings

This subsection presents the first spectra of coherent synchrotron radiation over a wide wavelength range at FLASH. The used synthetical diamond window at the BC3 port allows spectral measurements in the whole infrared regime. The measurements were performed using six different grating combinations. They covered a wavelength range from 160 μm

settings	parameters	G7.9	G13.3	G20
nominal	Q (nC)	0.76 ± 0.01	0.76 ± 0.01	0.75 ± 0.01
$\Phi_{ACC1} = -9°$	BPM-X (mm)	-0.71 ± 0.07	-0.25 ± 0.05	-0.61 ± 0.05
$Q = 0.8\,\mathrm{nC}$	BPM-Y (mm)	0.44 ± 0.02	0.40 ± 0.01	0.39 ± 0.01
nominal	Q (nC)	0.51 ± 0.01	0.51 ± 0.01	0.51 ± 0.01
$\Phi_{ACC1} = -9°$	BPM-X (mm)	-0.57 ± 0.06	-0.35 ± 0.05	-0.59 ± 0.04
$Q = 0.5\,\mathrm{nC}$	BPM-Y (mm)	0.44 ± 0.01	0.52 ± 0.02	0.44 ± 0.02
nominal	Q (nC)	0.77 ± 0.01	0.77 ± 0.01	0.77 ± 0.02
$\Phi_{ACC1} = -6°$	BPM-X (mm)	0.09 ± 0.04	0.38 ± 0.07	0.05 ± 0.02
$Q = 0.8\,\mathrm{nC}$	BPM-Y (mm)	-0.04 ± 0.01	0.04 ± 0.02	-0.04 ± 0.01

Table 6.4: Machine parameters for different settings. Part 1: G7.9, G13.3 and G20

settings	parameters	G30	G50	G90
nominal	Q (nC)	0.76 ± 0.01	0.79 ± 0.01	0.77 ± 0.01
$\Phi_{ACC1} = -9°$	BPM-X (mm)	-0.71 ± 0.07	-0.05 ± 0.08	-0.01 ± 0.05
$Q = 0.8\,\mathrm{nC}$	BPM-Y (mm)	0.44 ± 0.02	-0.05 ± 0.08	-0.05 ± 0.03
nominal	Q (nC)	0.51 ± 0.01	0.53 ± 0.01	0.53 ± 0.01
$\Phi_{ACC1} = -9°$	BPM-X (mm)	-0.31 ± 0.07	0.00 ± 0.04	0.02 ± 0.04
$Q = 0.5\,\mathrm{nC}$	BPM-Y (mm)	0.51 ± 0.01	-0.01 ± 0.02	-0.081 ± 0.02
nominal	Q (nC)	0.78 ± 0.01	0.77 ± 0.01	0.79 ± 0.01
$\Phi_{ACC1} = -6°$	BPM-X (mm)	0.32 ± 0.03	0.18 ± 0.03	0.18 ± 0.05
$Q = 0.8\,\mathrm{nC}$	BPM-Y (mm)	0.00 ± 0.02	-0.08 ± 0.03	-0.07 ± 0.03

Table 6.5: Machine parameters for different settings. Part 2: G30, G50 and G90

down to 9 μm, which is the most interesting range for bunch shape diagnostics. Spectra for three different machine settings are presented. For a nominal bunch charge of $Q = 0.8\,\mathrm{nC}$, spectral measurements with the two off-crest phases of $\Phi_{ACC1} = -9°$ and $\Phi_{ACC1} = -6°$ of the accelerator module ACC1 were done. In addition for the ACC1-phase of $\Phi_{ACC1} = -9°$, a spectral measurement with a nominal bunch charge of $Q = 0.5\,\mathrm{nC}$ was performed. In all cases, the phase of the modules ACC2/3 was set to on-crest with $\Phi_{ACC2/3} = 0°$. For each machine setting and grating set, the actual bunch charge and beam position at BC3 was recorded. The corresponding machine parameters are listed in table 6.4 and table 6.5. The measurements were processed according to the different corrections described in subsection 6.3.1. The right plot in Fig 5.8 show the grating efficiency of the zeroth and first

order. For a sufficient total efficiency of the gratings, a normalised wavelength range of $0.8 < \lambda/d < 1.3$ could be used in the measurements. The wavelength gaps in the spectra are indicated by grey columns. Fig. 6.14 to Fig. 6.16 show the full wavelength range of the measured spectra of coherent synchrotron radiation of the three different settings. The spectra show complex structures with existing intensity down to the shortest wavelengths,

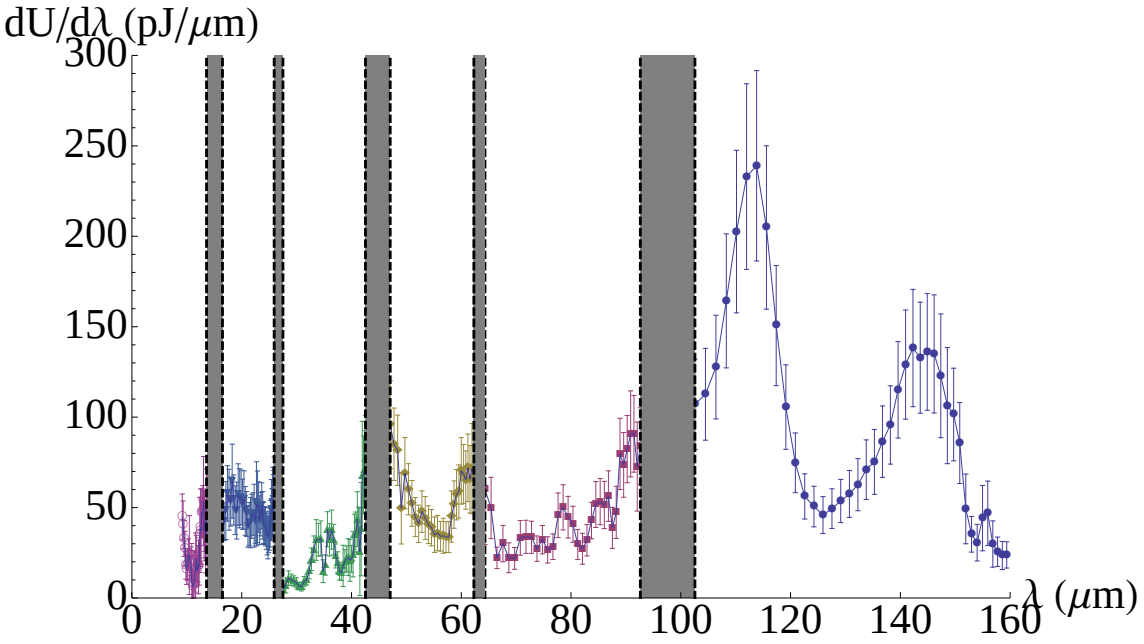

Figure 6.14: Spectrum of coherent synchrotron radiation for a bunch charge of $Q = 0.8\,\mathrm{nC}$ and ACC1-phase $\Phi_{ACC1} = -9°$.

accessible with the used gratings. The plot in Fig. 6.17 shows a combination of the spectra for the different machine settings. The cases with an ACC1-phase of $\Phi_{ACC1} = -9°$ show a notable amount of intensity in the short wavelength range below $30\,\mu\mathrm{m}$. The case of less bunch compression with an ACC1-phase of $\Phi_{ACC1} = -6°$ does not show this fact. The wavelength range above $100\,\mu\mathrm{m}$ exhibits two strong maxima, whose relative intensity is different for three machine settings.

Using the Eq. 3.12 and neglecting the incoherent part which scales linearly with the number of particles, the relative absolute square of the form factor can be introduced by

$$\boxed{|F|^2_{rel}(\lambda) = \left(\frac{Q_2}{Q_1}\right)^2 (dU_1/dU_2) = \frac{|F_1(\lambda)|^2}{|F_2(\lambda)|^2}}. \tag{6.3}$$

The left plot of Fig. 6.18 shows $|F|^2_{rel}$ for the same mean bunch charge of $0.77\,\mathrm{nC}$ and the two different ACC1-phases of $\Phi_{ACC1} = -6°$ and $\Phi_{ACC1} = -9°$. A complex behaviour is indicated with wavelength ranges, where the bunch that is compressed with an ACC1-phase of $\Phi_{ACC1} = -6°$ exhibits more intensity than for the bunch that is compressed with an ACC1-phases of $\Phi_{ACC1} = -9°$.

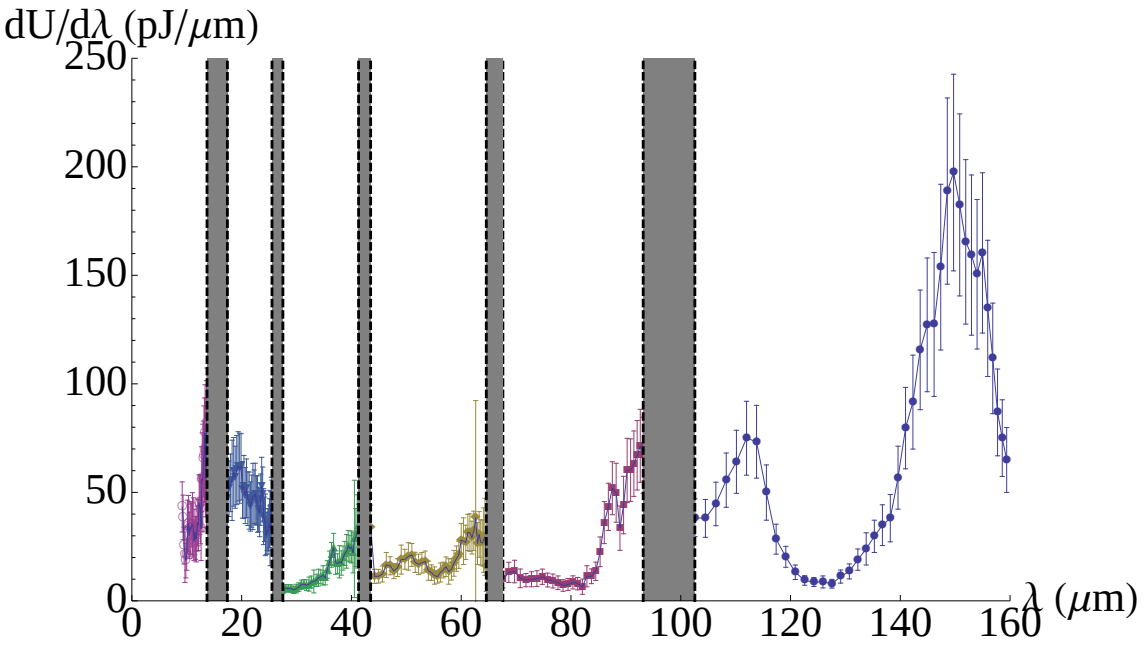

Figure 6.15: Spectrum of coherent synchrotron radiation for a bunch charge of $Q = 0.5\,\mathrm{nC}$ and ACC1-phase $\Phi_{ACC1} = -9°$.

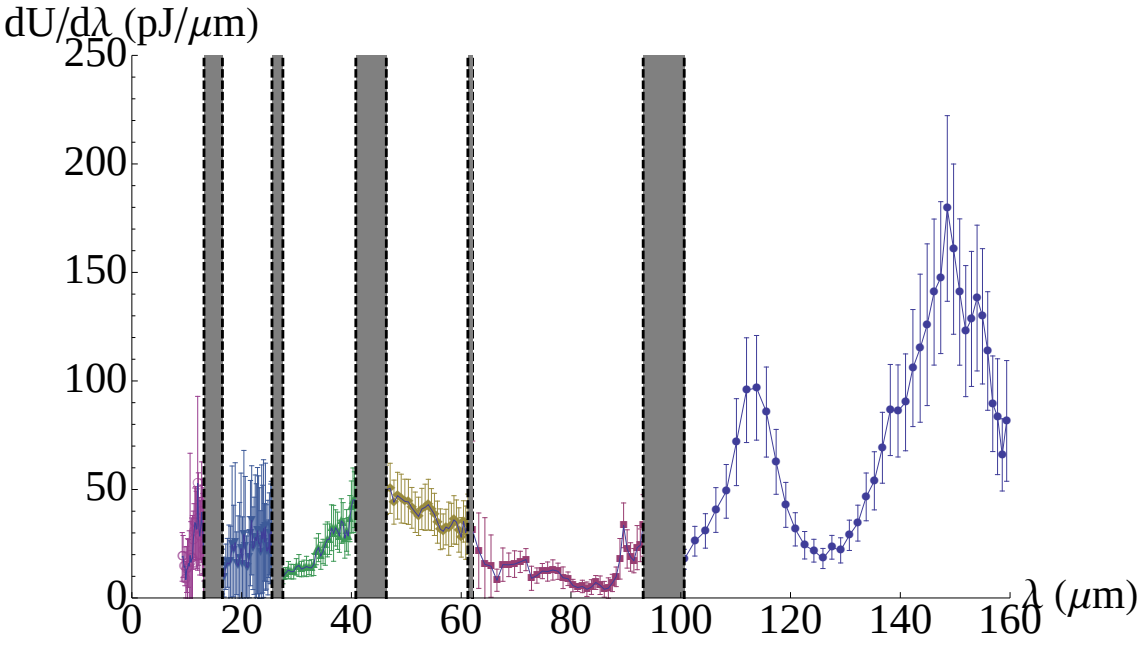

Figure 6.16: Spectrum of coherent synchrotron radiation for a bunch charge of $Q = 0.8\,\mathrm{nC}$ and ACC1-phase $\Phi_{ACC1} = -6°$.

The right plot of Fig. 6.18 shows the relative absolute square of the form factor for the same ACC1-phase of $\Phi_{ACC1} = -9°$ and the two different bunch charges of $Q = 0.52\,\mathrm{nC}$ and $Q = 0.77\,\mathrm{nC}$. An enhancement of intensity for small wavelengths below $40\,\mu\mathrm{m}$ and large wavelengths above $140\,\mu\mathrm{m}$ is observed for the bunch with the less charge of $Q = 0.52\,\mathrm{nC}$.

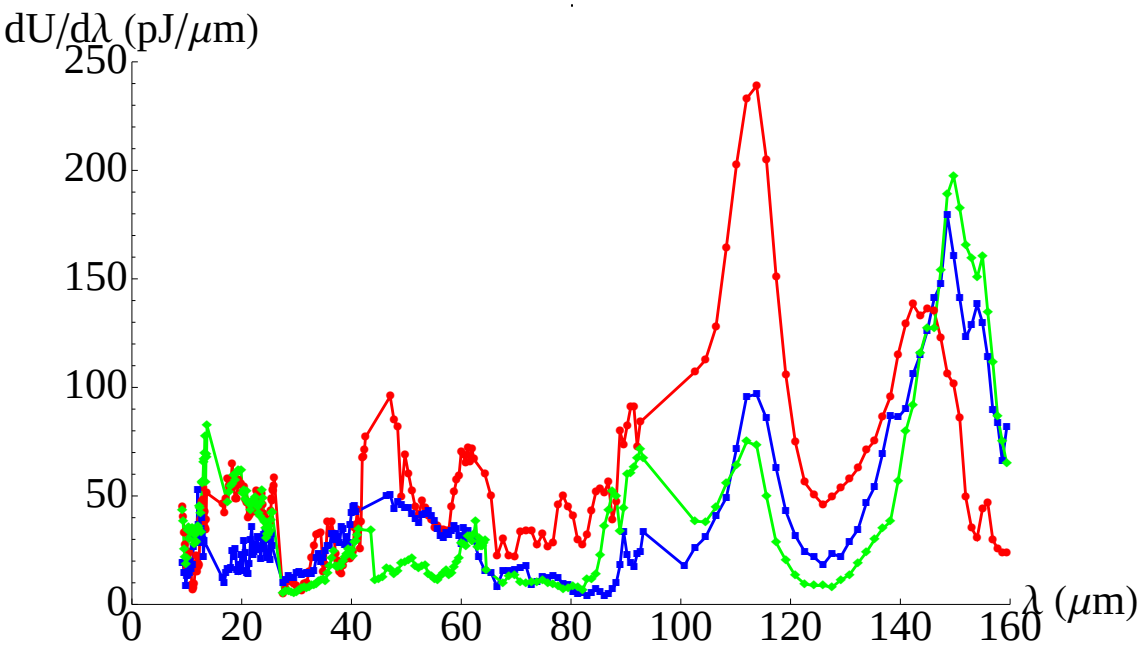

Figure 6.17: Spectra of coherent synchrotron radiation for the three cases. $Q = 0.8\,\mathrm{nC}$ and $\Phi_{ACC1} = -9°$: red, $Q = 0.5\,\mathrm{nC}$ and $\Phi_{ACC1} = -9°$: green, $Q = 0.8\,\mathrm{nC}$ and $\Phi_{ACC1} = -6°$: blue

The measurements presented here are the first observations of spectra of coherent synchrotron radiation at FLASH in this wavelength range. These measurements are also the first observations of spectra of CSR for almost finally compressed bunches after BC3. Reliable conclusions about the bunch shape or the dependencies of the spectra on the machine parameters need more systematic measurements and statistics.

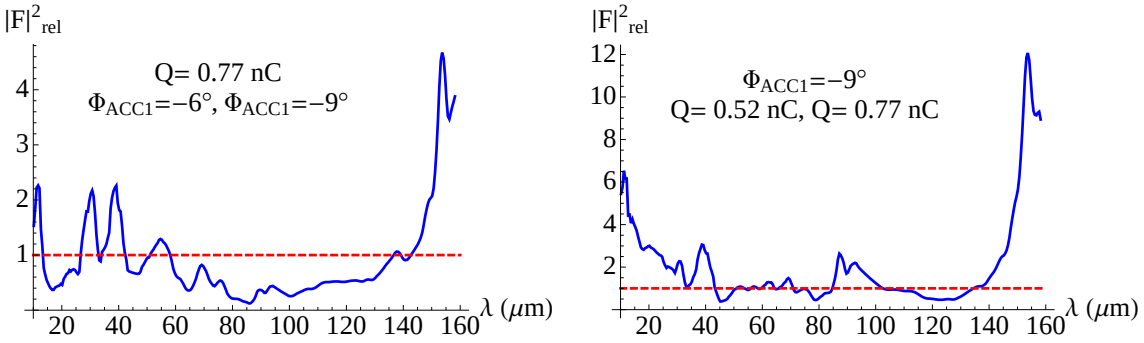

Figure 6.18: Relative absolute square of the form factors $|F|^2_{rel}$. Left: $Q = 0.77\,\mathrm{nC}$, F_1 with $\Phi_{ACC1} = -6°$ and F_2 with $\Phi_{ACC1} = -9°$. Right: $\Phi_{ACC1} = -9°$, F_1 with $Q_1 = 0.52\,\mathrm{nC}$ and F_2 with $Q_2 = 0.77\,\mathrm{nC}$. The red dashed line indicates the relative form factor of $|F|^2_{rel} = 1$.

6.3.4 Summary of the spectral measurements

The spectral measurements with the rotating mirror spectrometer that was installed at the second bunch compressor BC3 at FLASH yield the following results:

- The first spectral measurements of coherent synchrotron radiation at BC3 were done.
- A noticeable amount of short wavelengths below 30 μm was observed.
- The general spectrum is of low intensity.
- The wavelength calibration measurements indicate orbit dependencies.

The intensity that is rather small compared to coherent transition radiation could be restrictive for single bunch as well as single shot measurements using the present detector technology. This is a crucial requirement for monitor or feedback systems. Nevertheless, the use of coherent synchrotron radiation for bunch diagnostics is non-destructive and allows measurements in the entire wavelength range.

7 Numerical simulations

The theory of synchrotron radiation which was presented in chapter 2 is based on the following assumptions:

- The radiation is emitted in a magnet that has a constant field providing a constant curvature $1/\rho$ over a distance $l_r > 2\rho/\gamma$.
- The radiation is observed at a distance d from the source with $d \gg \rho/\gamma$.
- The electron moves with ultra-relativistic velocity ($\gamma \gg 1$).

The first two assumptions are not valid in general for synchrotron radiation which is emitted in the dipoles of a magnetic bunch compressor. If an observer is looking tangentially to the electron trajectory at the edge of a magnet, an influence on the synchrotron radiation spectrum is expected due to the region of non-constant magnetic field. Additional interference effects from two dipole magnets may appear if the observer is all the time within the opening angle of the emitted radiation. The electric field in time-domain will show two spikes of different amplitude which result from the different distances to the detector.
In order to check the validity of the general expressions of synchrotron radiation for the specific geometry of the second bunch compressor BC3 at FLASH, a numerical simulation in Mathematica was used. This numerical simulation is an implementation of the methods described in [31].

7.1 Numerical calculation

The numerical simulation is implemented in Mathematica and is able to calculate the electromagnetics fields of a single moving electron. The fundamental physics of the simulation is given by the expression for the electric field of a moving charge in Eq. (2.16), including both the acceleration and velocity term. For the given input parameters, e.g. the magnetic fields and the electron energy, the electron is tracked under the influence of the Lorentz force. For each time step $\Delta t'$, the electric field at a given observation point is calculated for the advanced time t in the future. This is done by means of Eq. (2.5), where $r(t')$ is the current distance. This method prevents to calculate the retarded time $t'(t)$ as a function of observation time, which is essential for the evaluation of Eq. (2.16). The result is the electric field $\vec{E}(t)$ as a function of the observation time t.

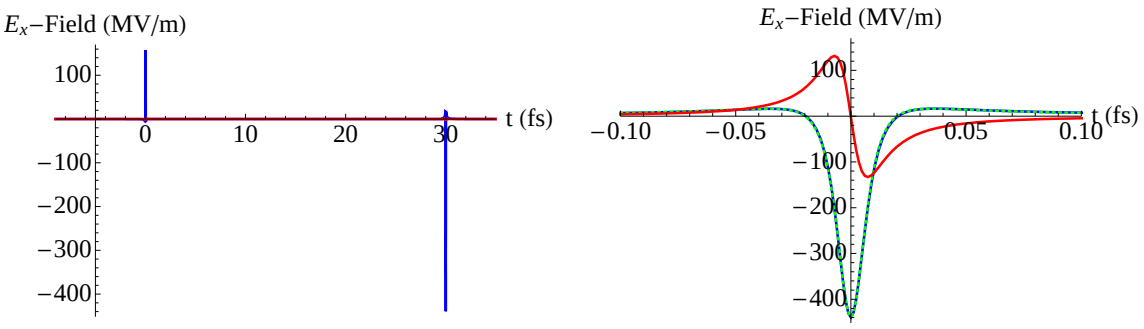

Figure 7.1: Left: Electric field in time-domain generated in the last two dipoles at BC3. Right: Electric field in time-domain of the last dipole at BC3. The calculation are made for $E = 480\,\mathrm{MeV}$ and $\Theta_e = 3.8°$ (velocity and acceleration field: blue, velocity field: red, analytical: green).

The spectrum is calculated by means of a discrete Fourier-transformation that is given by

$$\vec{E}(\nu_k) = \frac{1}{\sqrt{2\pi}} \int_{-\infty}^{\infty} \vec{E}(t) e^{-2\pi i \nu_k t} dt = \frac{1}{\sqrt{2\pi}} \sum_l \int_{t_l}^{t_{l+1}} \vec{E}(t) e^{-2\pi i \nu_k t} dt. \tag{7.1}$$

If the electric field does not vary too much between two adjacent times t_l and t_{l+1}, the electric field can be approximated by $\vec{E}(t_l)$. This approximation results in

$$\begin{aligned} \vec{E}(\nu_k) &\approx \frac{1}{\sqrt{2\pi}} \sum_l \vec{E}(t_l) \int_{t_l}^{t_{l+1}} e^{-2\pi i \nu_k t} dt \\ &= \frac{1}{2\pi i \nu_k \sqrt{2\pi}} \sum_l \vec{E}(t_l) \left(e^{-2\pi i \nu_k t_l} - e^{-2\pi i \nu_k t_{l+1}} \right) \\ &= \frac{1}{2\pi i \nu_k \sqrt{2\pi}} \sum_l \vec{E}(t_l) e^{-2\pi i \nu_k t_l} \left(1 - e^{-2\pi i \nu_k \Delta t_l} \right) \end{aligned} \tag{7.2}$$

with frequency component ν_k and time step $\Delta t_l = t_{l+1} - t_l$.

7.2 Electric field in time-domain

In order to check the numerical algorithm, the horizontal electric field component of an electron which is traversing a single dipole was compared to the calculated one using Eq. (2.30). The simulation parameters are those of the last dipole magnet at BC3 with the distance from source to observer of $d = 1.3\,\mathrm{m}$. The simulation is calculated including both the acceleration and velocity term. The right plot of Fig. 7.1 shows the different electric field contributions in time-domain. The velocity field is multiplied by 100 to make it visible. The numerical result is in good agreement with the analytical expression. Using the result shown in Fig. 2.4, the electric field zero-crossing at $t \approx 2 \cdot 10^{-17}\,\mathrm{s}$ yields the critical frequency $\omega_c = 5 \cdot 10^{16}\,\mathrm{s}^{-1}$ resp. the critical wavelength $\lambda_c \approx 40\,\mathrm{nm}$.

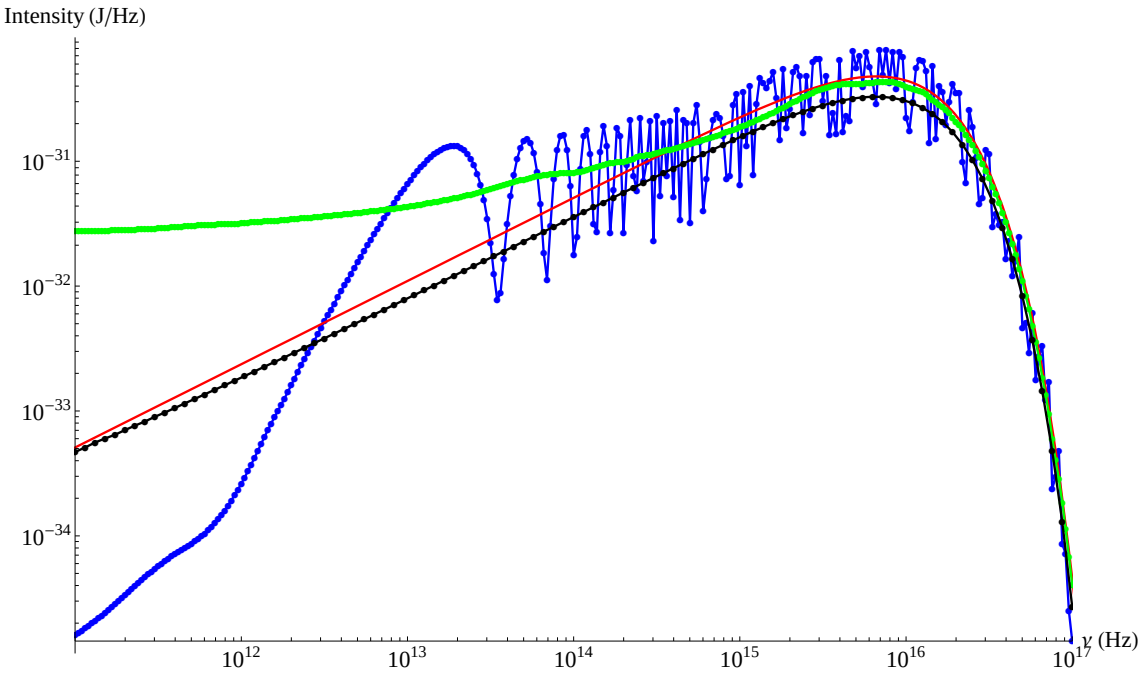

Figure 7.2: Spectrum for $E = 480\,\mathrm{MeV}$ and $\Theta_e = 3.8°$. (analytical: red, long dipole magnet of type BC3: black, last dipole magnet of BC3: green, last two dipole magnets of BC3: blue).

In order to investigate possible interference effects from two dipoles, the electric field in time-domain was calculated with the actual geometry of BC3 shown in Fig. 5.4. The result is shown in the left plot of Fig. 7.1. Two spikes of different amplitude and opposite sign appear. The opposite sign is due to different bending directions. The different amplitudes result from different distances to the observer. These two spikes will necessarily lead to interference effects in frequency-domain. The time interval between the spikes of $\Delta t \approx 30\,\mathrm{fs}$ results in a characteristic oscillation frequency of $1/\Delta t = 3.33 \cdot 10^{13}\,\mathrm{s}^{-1}$. More details will be given in the next section.

7.3 Electric field in frequency-domain

The left plot of Fig. 7.1 indicates two contributions to the total electric field detected be the observer. Fourier-transformation with the method in Eq. (7.2) yields the electric field in frequency-domain. In order to get a better understanding of the different effects, which influence the spectrum of synchrotron radiation, further cases were considered. Fig. 7.2 shows spectra according to Eq. (2.44), including the last two dipoles of BC3, including only the last dipole of BC3 and for the case of a long magnet with the same magnetic field as in the dipoles of BC3. In order to compare the results with theoretical predictions, the analytic formula in Eq. (2.45) was used. The distance to the observer is the same in all cases.

The numerical result for the long magnet has the same shape as the analytic solution, but

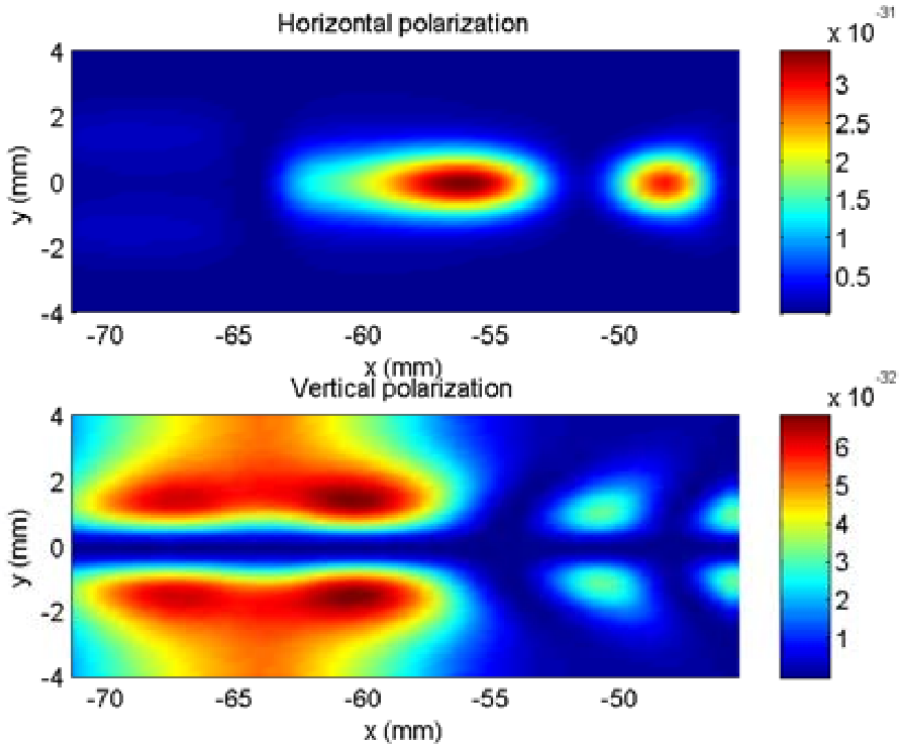

Figure 7.3: Transverse intensity distribution at BC3 at a wavelength of 50 μm. Interference and shielding effects ate taken into account (Courtesy of O. Grimm).

is slightly less intensive. This behaviour results from the short distance of 1.3 m to the observer. If the distance is shifted to 5 m, the numerical calculation agrees well with the analytic result.

The result for the last dipole of BC3 shows an enhancement of the low-frequency components. This effect results from the edge of the magnet. The detailed shape of the spectrum depends on the distance scale over which the magnetic field changes [31].

If both dipoles are considered, the expected interference effects become visible with the typical oscillating frequency of $1/\Delta t = 3.33 \cdot 10^{13} s^{-1}$. These interference effects also appear in the transverse intensity distributions. Fig. 7.3 shows the transverse intensity distribution of horizontally and vertically polarised radiation at the synchrotron radiation port at BC3 for a wavelength of 50 μm. This calculation has also taken into account shielding effects of the finite height of the BC3 vacuum chamber [31]. The total intensity exhibits two maxima similar to those presented in section 6.2.

The presented numerical simulations show the general impacts of the magnet geometry on the spectrum. More detailed calculations can be found in [31].

8 Conclusions

For detection of coherent radiation in the infrared regime, three pyroelectric detectors of different types were calibrated at the free-electron laser at FELIX. The measurements yield the responsivity R for each detector in the wavelength range from $5\,\mu$m to $110\,\mu$m. The wavelength dependencies of the responsivity show qualitative agreement with the theoretical model of the pyroelectric detector. The main uncertainties of the model are the unknown optical constants of NiCr.
Two detectors are coated with a black polymer to enhance the absorption of radiation. The influence of this black polymer coating was investigated wavelength-resolved. The measurements show a strong impact of this coating at short wavelengths. At large wavelengths, the coating becomes almost transparent.
The main error source of the calibration measurements is the uncertainty of the response function of the powermeter used.

The calibrated pyroelectric detectors were used for the detection of coherent synchrotron radiation at FLASH. A new experimental setup was installed at the last dipole magnet of the second bunch compressor BC3. The beamline for the radiation transport was equipped with a diamond window to transmit the whole range of infrared radiation.
In the first step, the transverse intensity distribution of coherent synchrotron radiation was investigated by means of a transverse scanning device. A complex structure comprising two intensity maxima was revealed. The origin of this twofold maxima structure is not fully understood at the moment. Numerical simulations indicate that the two maxima could be generated by interference effects of radiation emitted in the last and second last dipole magnet of BC3.
In addition, transmission filters were used to get spectral information of the coherent synchrotron radiation. The observed intensity is rather low but also present at short wavelengths below $40\,\mu$m.

The measurements with the transverse scanning device showed that the transverse dimensions of the CSR are suitable for using the available dispersive gratings for spectral measurements. In order to get more spectral informations about the coherent synchrotron radiation, a new setup with a rotating mirror spectrometer was installed. First spectra of CSR for almost finally compressed bunches were observed over a wavelength range from $10\,\mu$m to $160\,\mu$m. The measurements were performed for different machine settings. The

resulting spectra show complex wavelength dependencies. The general intensity is rather low compared to other coherent radiation sources like coherent transition radiation. At wavelengths larger than 100 μm, two peaks are observed which show a strong dependence on the machine parameters. In case of bunches accelerated $-9°$ off-crest in module ACC1, a significant intensity is observed at wavelengths smaller than 30 μm.

8.1 Outlook

In the future, the properties of coherent synchrotron radiation behind BC3 should be further investigated. In order to clarify the origin of the twofold maxima structure, the transverse intensity distributions could be measured for different polarisations.
The spectral measurements presented, are the first measurements of synchrotron radiation behind the last bunch compressor of FLASH. Further exploration of the parameters that affect the spectra of CSR should be done, in particular, if coherent synchrotron radiation will be used for compression feedback systems at the European XFEL. The big advantage of CSR is that it permits destruction-free diagnostics in the entire wavelength range. The drawback could be the poor intensity and potential orbit dependencies on the spectrum which was indicated by the wavelength calibration. In order to improve the maximal intensity which can be detected, comprehensive simulations should be done to find a good position and geometry of the detection port.
In order to finally answer the question if coherent synchrotron radiation can be used for feedback systems, dedicated experiments have to be done.

A Filter transmission curves

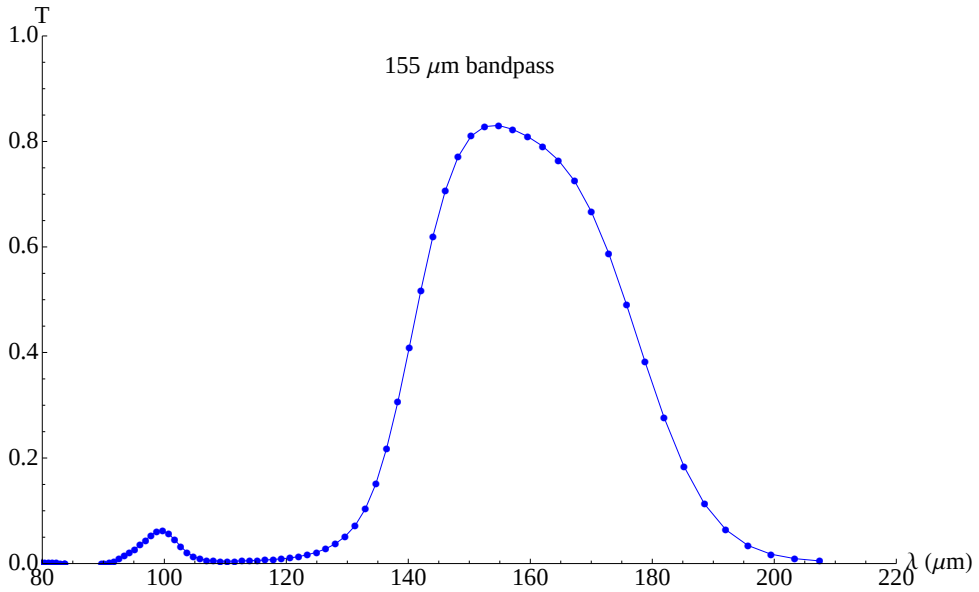

Figure A.1: Transmission of the 155 μm bandpass filter.

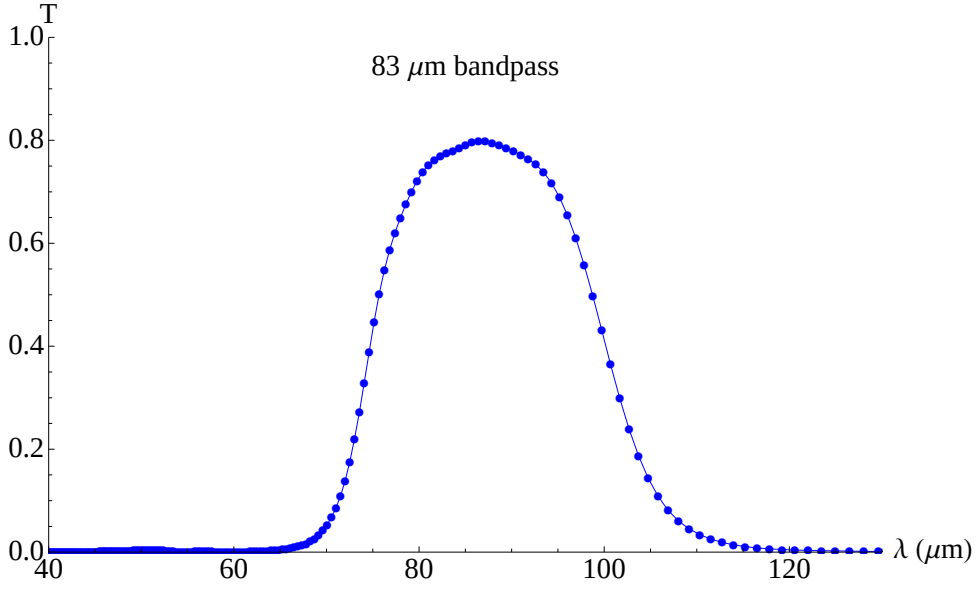

Figure A.2: Transmission of the 83 μm bandpass filter.

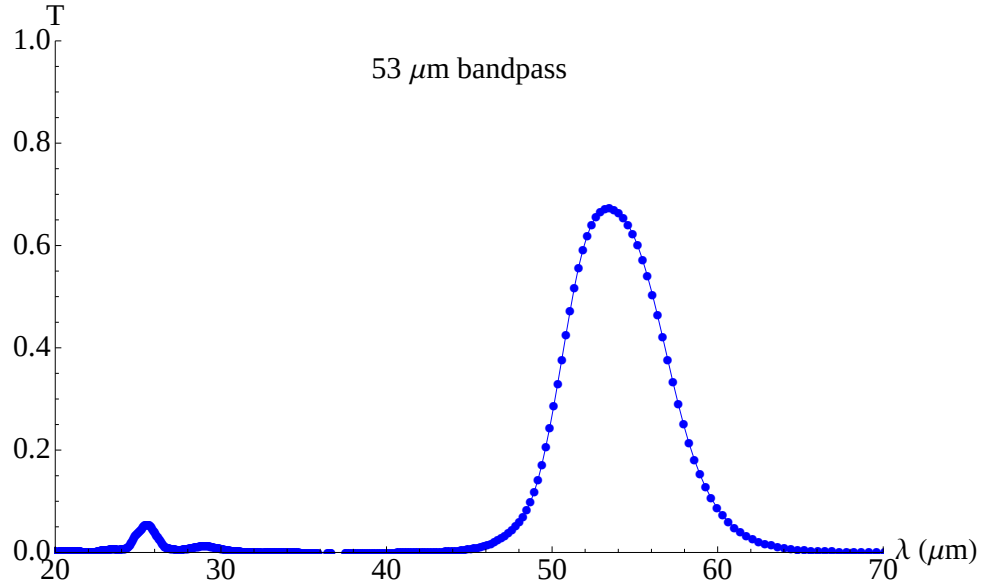

Figure A.3: Transmission of the 53 μm bandpass filter.

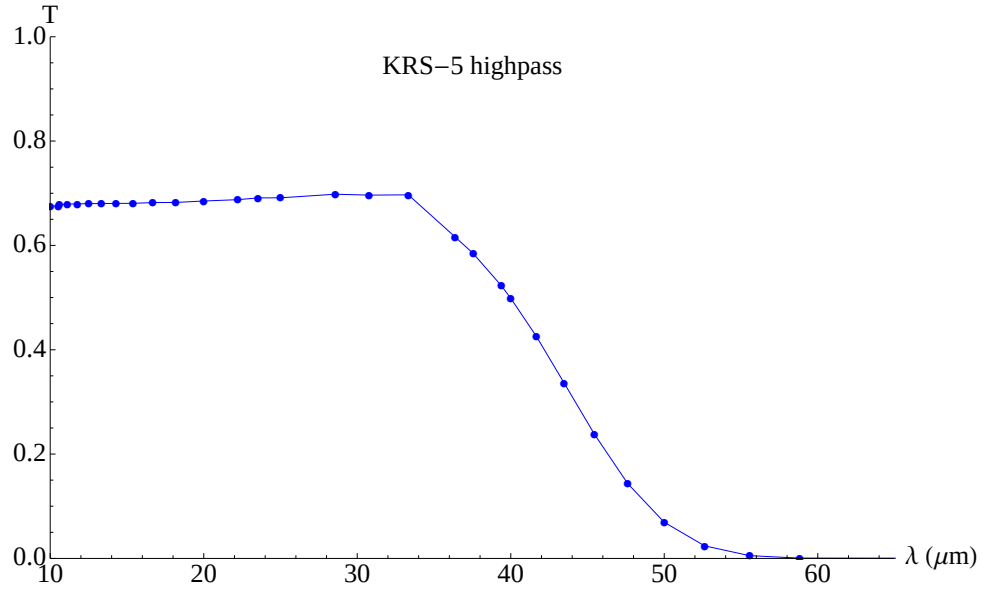

Figure A.4: Transmission of KRS-5 highpass filter. (KRS-5: Tallium Bromide-Iodide)

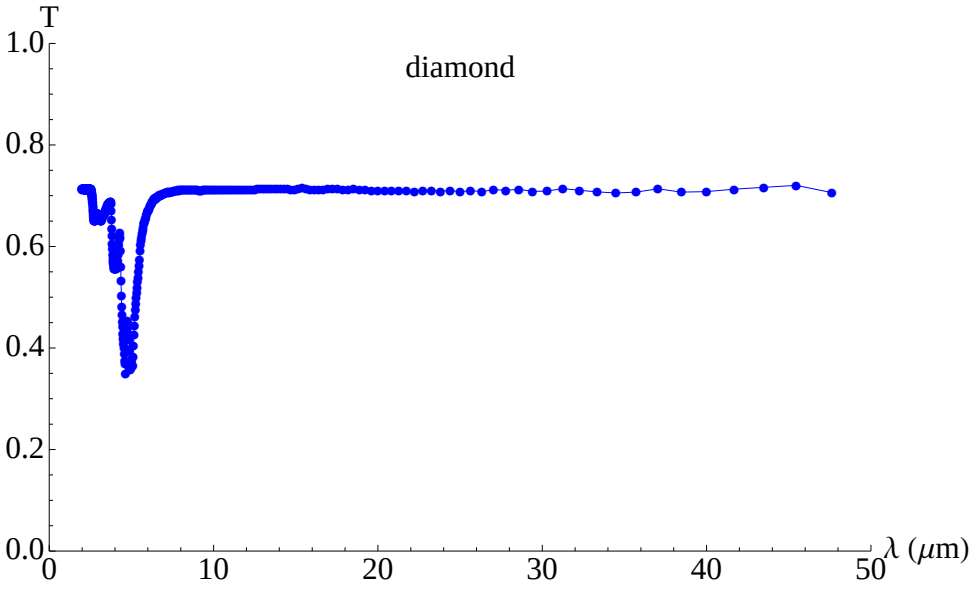

Figure A.5: Transmission of synthetic diamond.

B Detector outputs at FELIX

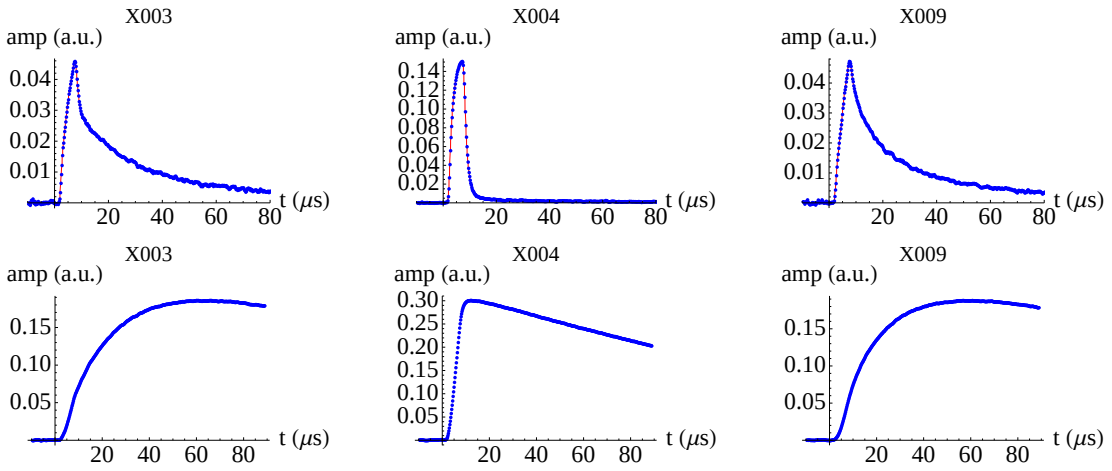

Figure B.1: Measured detector outputs at 10 μm. Top: Shaping-amplifier output (fit in red). Bottom: Pre-amplifier output.

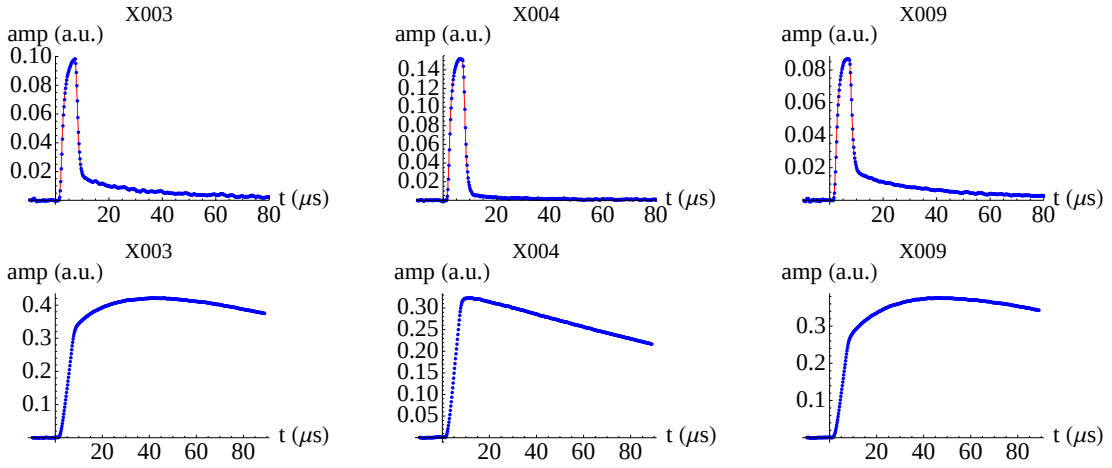

Figure B.2: Measured detector outputs at 30 μm. Top: Shaping-amplifier output (fit in red). Bottom: Pre-amplifier output.

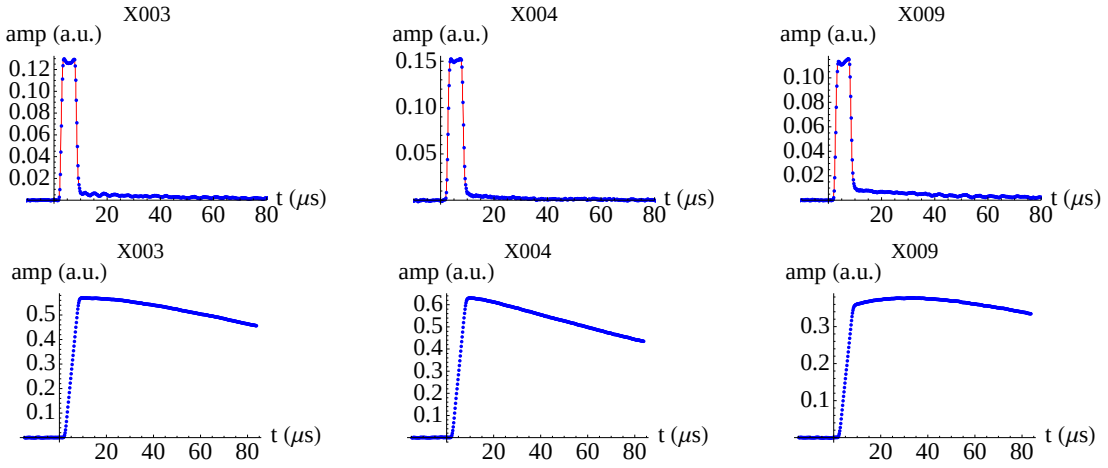

Figure B.3: Measured detector outputs at 50 μm. Top: Shaping-amplifier output (fit in red). Bottom: Pre-amplifier output.

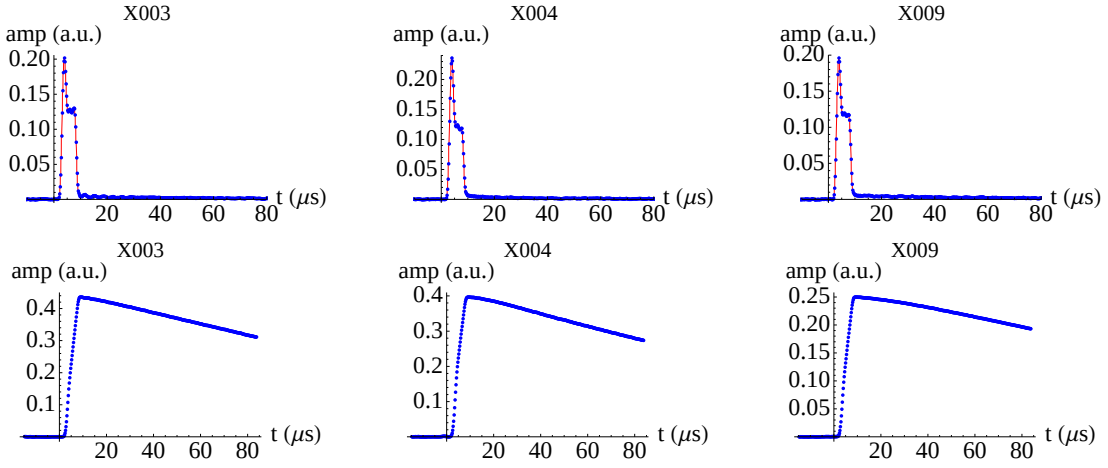

Figure B.4: Measured detector outputs at 100 μm. Top: Shaping-amplifier output (fit in red). Bottom: Pre-amplifier output.

C Wavelength calibration

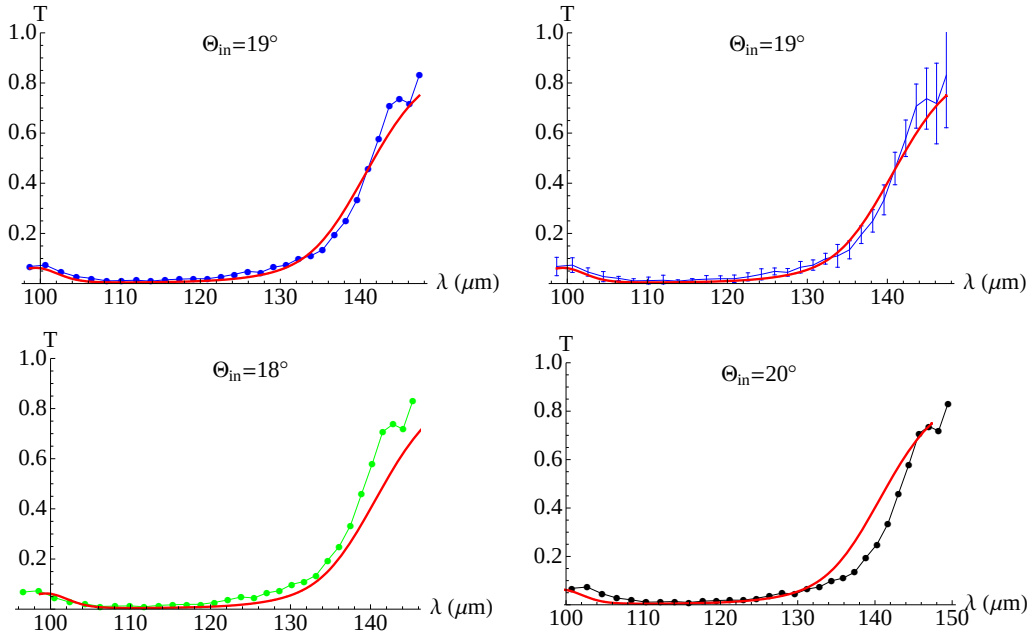

Figure C.1: Wavelength calibration with the 155 μm bandpass filter (filter curve in red). Top row: Transmission with the nominal incoming angle of $\Theta_{in} = 19°$. Bottom row: Transmission with the shifted incoming angles of $\Theta_{in} = 18°$ and $\Theta_{in} = 20°$.

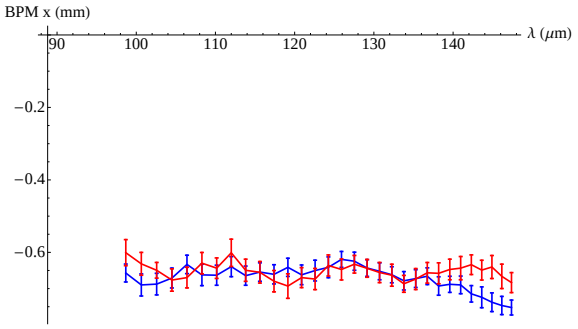

Figure C.2: Horizontal beam positions behind the last dipole of BC3 during the wavelength calibration with the 155 μm bandpass filter. The different curves (blue and red) show the position for the both cases with and without filter.

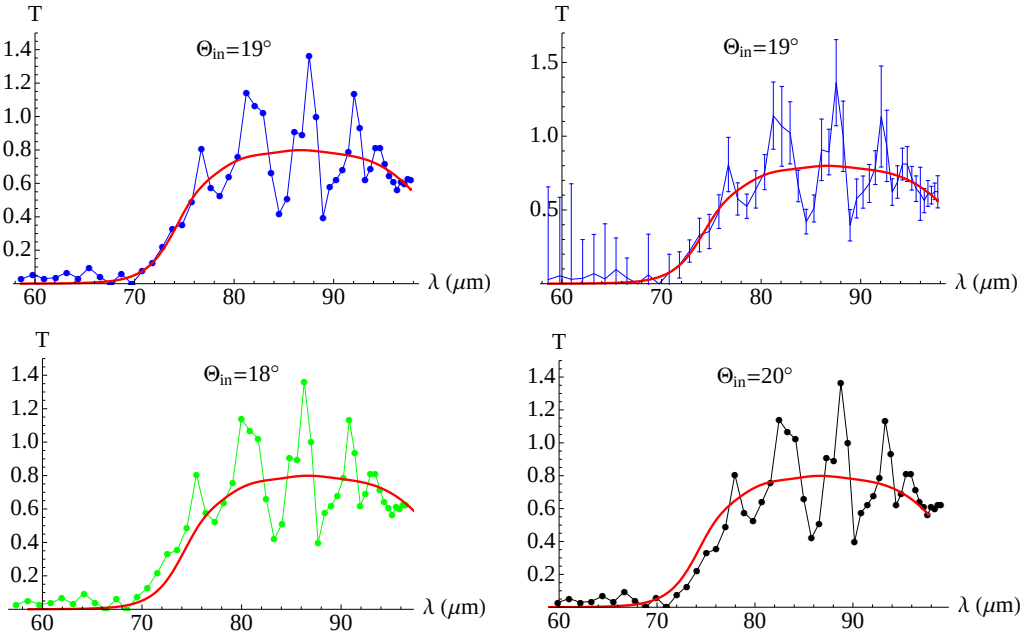

Figure C.3: Wavelength calibration with the 83 μm bandpass filter (filter curve in red). Top row: Transmission with the nominal incoming angle of $\Theta_{in} = 19°$. Bottom row: Transmission with the shifted incoming angles of $\Theta_{in} = 18°$ and $\Theta_{in} = 20°$.

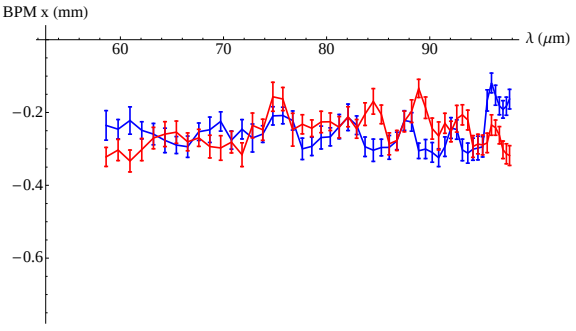

Figure C.4: Horizontal beam positions behind the last dipole of BC3 during the wavelength calibration with the 83 μm bandpass filter. The different curves (blue and red) show the position for the both cases with and without filter.

Bibliography

[1] D. Iwanenko and I. Pomeranchuk. On the maximal energy attainable in a betatron. *Physical Reviev*, 65:343, 1944.

[2] G.C. Baldwin. Origin of synchrotron radiation. *Physics Today*, 28(1):9–11, 1975.

[3] F.R. Elber, A.M. Gurewitsch, R.V. Langmuir, and H.C. Pollock. Radiation from electron in a synchrotron. *Physical Reviev*, 71:827, 1947.

[4] J. Schwinger. On the classical radiation of accelerated electrons. *Physical Reviev*, 75(12):1912, 1949.

[5] J.A. Clarke. *The Science and Technology of Undulators and Wigglers.* Oxford Univeristy Press, 2004.

[6] J.M.J Madey. Stimulated emission of bremsstrahlung in a periodic magnetic field. *Journal of Applied Physics*, 42(5):1906, 1971.

[7] K. Wille. *The Physics of Particle Accelerators.* Oxford Univeristy Press, 2000.

[8] P. Schmüser, M. Dohlus, and J.Rossbach. *Ultraviolet and Soft X-Ray Free-Electron Lasers.* Springer, 2008.

[9] A.M. Kondratenko and E.L. Saldin. Generation of coherent radiation by a relativistic electron beam in an ondulator. *Particle Accelerators*, 10:207, 1980.

[10] R. Bonifacio, C. Pellegrini, and L.M. Narducci. Collective instabilities and high-gain regime in a free electron laser. *Opt. Comm.*, 50:373, 1984.

[11] *FOM-Institute for Plasma Physics Rijnhuizen.* `http://www.rijnhuizen.nl/felix/`.

[12] *Free-Electron-Laser in Hamburg.* `http://flash.desy.de/`.

[13] *The Conceptual Design Report for the TTF: Free-Electron Laser.* `http://flash.desy.de/tesla/tesla_documentation`.

[14] F. Stulle. *A Bunch Compressor for small Emittances and high Peak Currents at the VUV Free-Electron Laser.* PhD thesis, Universität Hamburg, 2004.

[15] A. Hofmann. *The Physics of Synchrotron Radiation.* Cambridge Univeristy Press, 2004.

[16] O. Grimm and P. Schmüser. Principles of longitudinal beam diagnostics with coherent radiation. *TESLA FEL*, 3, 2006.

[17] O. Grimm et al. Transverse electron beam size effect on the bunch profile determination with coherent radiation diagnostics. *Proc. of EPAC 2008*, pages 1113–1115, 2008.

[18] B. Schmidt et al. Longitudinal structure of electron bunches at the micrometer scale from spectroscopy of coherent transition radiation. *Proc. of EPAC 2008*, pages 130–132, 2008.

[19] H. Delsim-Hashemi et al. Bunch compression monitor. *Proc. of EPAC 2006*, pages 86–88, 2006.

[20] S. Casalbuoni, B. Schmidt, and P. Schmüser. Far-infrared transition and diffraction radiation - part i: Production, diffraction effects and optical propagation. *TESLA FEL*, 15, 2005.

[21] A.L. Stanford Jr. Detection of electromagnetic radiation using the pyroelectric effect. *Solid-State Electronics*, 8(9):747 – 755, 1965.

[22] O. Grimm. Operation principles of pyroelectric detectors. *DESY-FLA webpage*, 2004. `http://tesla.desy.de/fla/crd/IR_related_info.html`.

[23] B. Schmidt, H. Delsim-Hashemi, and O. Grimm. Comments on pyroelectric response - influence of material parameters and geometry. *DESY-FLA webpage*, 2005. `http://tesla.desy.de/fla/crd/IR_related_info.html`.

[24] B. Schmidt. Pyrodetektoren für schnelle signale - high speed, low noise. *DESY-FLA webpage*, 2005. `http://tesla.desy.de/fla/crd/IR_related_info.html`.

[25] M. Born. *Principles of Optics*. Oxford Pergamon Press, 1993.

[26] B. Schmidt, H. Delsim-Hashemi, O. Grimm, and P. Schmüser. The reflection, transmission, and absorbtion coefficients for a multi-layer arrangement of dielectric materials for vertical incidence of electromagnetic waves. *DESY-FLA webpage*, 2005. `http://tesla.desy.de/fla/crd/IR_related_info.html`.

[27] S. Wesch. *Spektroskopie kohärenter Übergangsstrahlung zur Strukturanaylse von Elektronenpaketen am FLASH-Beschleuniger*. Diploma thesis, Universität Hamburg, 2008.

[28] Particle Data Group. Particle physics booklet. *PDG webpage*, 2008. `http://pdg.lbl.gov/`.

[29] L. Fröhlich. Dark current transport in the flash linacc. *Proc. of PAC 2007*, pages 956–958, 2007.

[30] H. Delsim-Hashemi. *Infrared Single Shot Diagnostics for the Longitudinal Profile of the Electron Bunches at FLASH*. PhD thesis, Universität Hamburg, 2008.

[31] O. Grimm. Synchrotron radiation for beam diagnostics: Numerical calculations of the single electron spectrum. *TESLA FEL*, 5, 2008.

[32] E.L. Saldin, E.A. Schneidmiller, and M.V. Yurkov. Coherent radiation on an electron bunch moving in an arc of a circle. *Proc. of PAC 1997*, pages 1658–1660, 1997.

Acknowledgements

In order to prevent the German adage "Lange Rede, kurzer Sinn" ...
I would like to thank

Dr. Bernhard Schmidt,
Prof. Dr. Jörg Roßbach,
Prof. Dr. Peter Schmüser,
Dr. Michael Röhrs,
Lasse Schroedter,
all members of FLA,
all technicians of FLA,
the FLASH team,
the FELIX team,
my room mate Timo Schaepe and
especially my girlfriend Elgin Oyrak.